



HAL
open science

Investigation of a rare earth doped niobate ceramic for optical applications

Ka Young Kim

► **To cite this version:**

Ka Young Kim. Investigation of a rare earth doped niobate ceramic for optical applications. Material chemistry. Université de Bordeaux, 2016. English. NNT : 2016BORD0416 . tel-01599243

HAL Id: tel-01599243

<https://theses.hal.science/tel-01599243>

Submitted on 2 Oct 2017

HAL is a multi-disciplinary open access archive for the deposit and dissemination of scientific research documents, whether they are published or not. The documents may come from teaching and research institutions in France or abroad, or from public or private research centers.

L'archive ouverte pluridisciplinaire **HAL**, est destinée au dépôt et à la diffusion de documents scientifiques de niveau recherche, publiés ou non, émanant des établissements d'enseignement et de recherche français ou étrangers, des laboratoires publics ou privés.

THÈSE PRÉSENTÉE
POUR OBTENIR LE GRADE DE
DOCTEUR DE
L'UNIVERSITÉ DE BORDEAUX

ÉCOLE DOCTORALE des Sciences Chimiques
SPÉCIALITÉ : Physico-chimie de la matière condensée

Ka-Young KIM

**Investigation of a rare earth doped niobate ceramic for
optical applications**

Sous la direction de : Véronique Jubera et Jean-Marc Heintz
(co-encadrante : Amélie Veillere)

Soutenue le 2 Novembre 2016

Membres du jury :

Rémy BOULESTEIX, Maître de Conférences, Université de Limoges
Geneviève CHADEYRON, Professeure-Sigma Clermont - ICCF Clermont-Ferrand
Claude ESTOURNES, Directeur de recherche au CNRS, CIRIMAT
Jean –Marc HEINTZ, Professeur, Bordeaux INP
Véronique JUBERA, Maître de Conférences HDR, Université de Bordeaux
Mario MAGLIONE, Directeur de recherche au CNRS, ICMCB
Seung-Han PARK, Professeur, Université de Yonsei
Amélie VEILLERE, Maître de Conférences, Bordeaux INP

Examineur
Rapportrice
Secrétaire
Examineur
Examinatrice
Président
Rapporteur
Examinatrice

Étude d'un niobate Y_3NbO_7 dopé terre rare pour applications optiques

Résumé français du manuscrit

1. Intérêt économique

Les matériaux émetteurs et plus particulièrement les matériaux à gain (lasers) sont largement employés dans le domaine de l'optique et des sciences des matériaux en tant que sources d'excitation, pour des mesures expérimentales, des applications médicales, de la mise en forme de matériaux métalliques (telle que la fabrication additive) ou encore pour de l'inscription et de l'éclairage. Les matériaux sous forme de verres, de fibres cristallines et les cristaux sont largement majoritaires au sein des dispositifs concernés mais la part des céramiques optiques s'accroît en regard de l'amélioration de leurs caractéristiques.

Les sources lasers commerciales sont développées autour de 1 micron mais, alors que le domaine du visible reste peu couvert, des premiers travaux rapportent des résultats intéressants sur des composés dopés terbium et praséodyme. Le besoin de couvrir le domaine s'étendant de 535 à 640 nm reste important, sachant que ces longueurs d'onde sont difficilement atteignables au moyen de sources doubles telles que les lasers titane saphir. Le développement de sources d'excitation type diodes semi-conductrices permet désormais d'envisager le pompage d'ions de terres rares tels que l'euporium et celles citées précédemment.

Si nous nous intéressons à présent au domaine du moyen infrarouge, des ions tels que l'holmium, l'erbium ou le thulium permettent de générer des émissions lasers autour de 2 microns. De telles longueurs d'onde sont alors envisageables pour exciter des composés semi-conducteurs permettant d'atteindre 3-5 microns tel que $Cr^{2+}:ZnSe$.

La plupart des études rapportant de très bonnes performances sont associées à des monocristaux. De plus, les compositions qui sont envisagées pour accéder aux nouvelles longueurs d'onde sont en fait proches de celles testées à 1 micron. Considérant le coût élevé et le temps d'obtention de ces monocristaux ainsi que les contraintes liées à des changement de domaines de longueurs d'onde, il est essentiel aujourd'hui de considérer de nouvelles compositions et de se tourner, dans la mesure du possible, vers d'autres moyens de mise en

forme. Les céramiques optiques apparaissent donc comme des objets qui présentent un attrait certain.

2. Techniques de frittage et céramiques optiques

Le choix et l'optimisation des paramètres de frittage mais aussi la qualité des poudres de départ (taille de grains, cristallinité, morphologie) sont des éléments cruciaux pour la densification et la qualité optique des céramiques. De plus, les post-traitements thermiques et la qualité des polissages sont aussi des étapes à ne pas négliger sous peine de réduire considérablement les performances optiques de ces matériaux. On trouve dans la littérature de nombreux procédés de mise en forme des céramiques, tels que le frittage sous vide (VS), le pressage à chaud (hot-pressing ou HP), le pressage isostatique à chaud (hot-isostatic pressing ou HIP), les frittages flash avec le SPS (spark plasma sintering), le PAS (plasma-activated sintering) ou encore le PECS (pulse electric sintering), etc... Chacun de ces procédés est associé à des températures, des temps et des pressions très différents. L'ajustement de ces paramètres est alors étroitement lié à la nature de la phase à fritter.

3. Monocristal versus céramique

L'efficacité d'un laser solide est conditionnée par différents critères. Le milieu à gain doit être obtenu avec une taille et une qualité optique suffisamment élevée pour que l'on puisse sélectionner des zones exemptes de défauts et de centres diffusants. La mise en forme qui repose sur des étapes de polissage nécessite de bonnes propriétés mécaniques et une certaine stabilité thermique et chimique. Le matériau doit également avoir une bonne tenue sous irradiation et les échauffements locaux doivent être limités par une bonne conductivité thermique. De plus, les variations d'indice de réfraction avec la température ou les indices non linéaires des matériaux non centro-symétriques peuvent affecter la géométrie du faisceau laser et conduire à des phénomènes d'auto-focalisation.

A ces critères de limitation d'efficacité optique se rajoutent, lorsque l'on parle de céramiques, la diminution de la conductivité thermique intrinsèque aux matériaux polycristallins et le degré de densification, conditions sine qua none à l'obtention d'une transparence optimale. La transmission optique dans une céramique ne peut être atteinte que pour des densités relatives supérieures à 99 % de la densité théorique de la phase, c'est-à-dire après élimination de toute porosité fermée. De plus, la taille des cristallites et la symétrie

de la maille élémentaire jouent un rôle crucial sur les pertes par diffusion du matériau fritté. Des composés de symétrie cubique présentant un indice de réfraction isotrope seront donc préférés.

Les grenats tels que Nd:YAG (YAG = yttrium aluminum garnet, i.e. $Y_3Al_5O_{12}$), les tungstates, Yb:KGW ($KGd(WO_4)_2$) ou encore les sesquioxides, Yb:TR₂O₃ (TR : terre rare) sont des matériaux phares en termes de performances. Mais l'obtention de monocristaux de taille importante reste limitée par le processus de croissance cristalline, lui-même lié à la nature de la fusion des composés.

La difficulté d'obtenir des monocristaux de taille importante a conduit à développer l'élaboration de céramiques. L'élaboration de céramiques transparentes a débuté dans les années 50 mais le premier test laser probant réalisé sur une céramique n'a été enregistré qu'en 1990, en parallèle au développement de nouvelles voies de synthèse des poudres de départ. La plupart des travaux publiés sur les céramiques sont centrés sur les compositions des matériaux cubiques ayant satisfait aux critères requis pour les applications lasers, à l'état de monocristal. Nous pouvons citer les grenats de type YAG et LuAG, Al₂O₃, les sesquioxides Y₂O₃, Lu₂O₃, les spinelles MgAl₂O₄, les fluorures CaF₂ et plus récemment Lu₃NbO₇.

4. Étude du composé Y₃NbO₇

Les composés de la famille des niobates présentent généralement un large domaine de transparence dans le visible et l'infrarouge. Les travaux publiés sur la matrice Lu₃NbO₇ étant très prometteurs, nous avons sélectionné le réseau hôte Y₃NbO₇ pour faire une première étude de frittage de ce composé par SPS. La spectroscopie de luminescence de l'euporium trivalent, ion substitué à l'yttrium, a été également étudiée pour comprendre le comportement de cette phase lors du frittage SPS.

Nous avons, dans un premier temps, mise en œuvre différentes voies de synthèse du composé Y₃NbO₇. Les voies d'auto-combustion et les voies solides testées n'ont pas permis d'obtenir des matériaux pulvérulents purs. Nous nous sommes alors tournés vers des voies de synthèse de type Pechini. La méthode "basse température" qui a été optimisée, dérive d'un protocole de synthèse initialement proposé par T. Okubo et al. Des quantités stœchiométriques de TR₂O₃ (99,99%) (TR : Y et Eu) et de NbCl₅ (99,998%) ont été mises en solution dans de l'acide nitrique et du méthanol respectivement. La solution de nitrate a été

évaporée à sec et le résidu solide broyé. Un large excès d'acide citrique a ensuite été ajouté à la solution de méthanol contenant les ions niobates, avant d'introduire le résidu broyé de nitrate de terre rare. Finalement, de l'éthylène glycol a été ajouté et la solution chauffée à environ 140°C pour accélérer la réaction d'estérification, jusqu'à obtention d'une résine brune. La phase solide ainsi obtenue (résine brune) a ensuite été traitée thermiquement pour éliminer les résidus carbonés jusqu'à obtention d'une poudre blanche. L'évaluation de la morphologie des poudres lors des traitements thermiques est présentée ci-dessous (Figure 1)

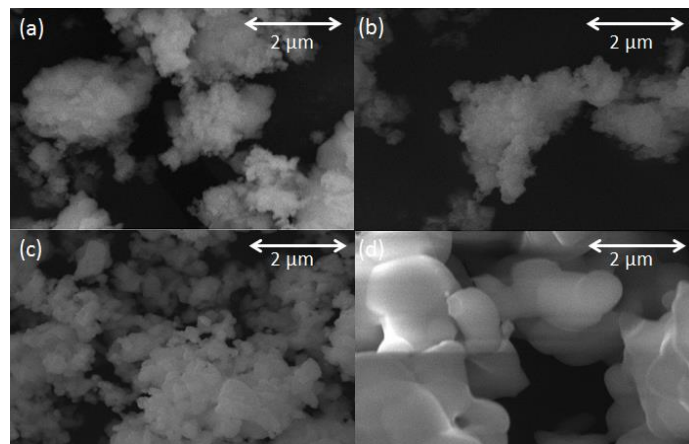


Figure 1 : Morphologie des poudres de niobate d'yttrium (micrographies MEB) (a) à l'issue de la synthèse et après traitement thermique à (b) 1000°C, (c) 1350°C et (d) 1600°C.

D'après le diagramme d'équilibre des phases $Y_2O_3-Nb_2O_5$, la phase Y_3NbO_7 présente un domaine d'existence significatif ($0,2 < Nb/[Nb+Y] < 0,3$). Pour éviter la formation du composé défini $YNbO_4$, impureté fréquemment détectée lors du processus d'optimisation des voies de synthèse, nous avons alors choisi d'étudier un composé moins riche en niobium. Nous nous sommes alors intéressés, dans un premier temps, à la stabilité thermique du composé $Y_{2,85}Eu_{0,15}Nb_{0,9}O_{6,75}$ ($Nb/[Nb+Y] = 0,23$). Les résultats issus de la diffraction des rayons X des poudres obtenues par voie Pechini sont illustrés sur la figure 2.

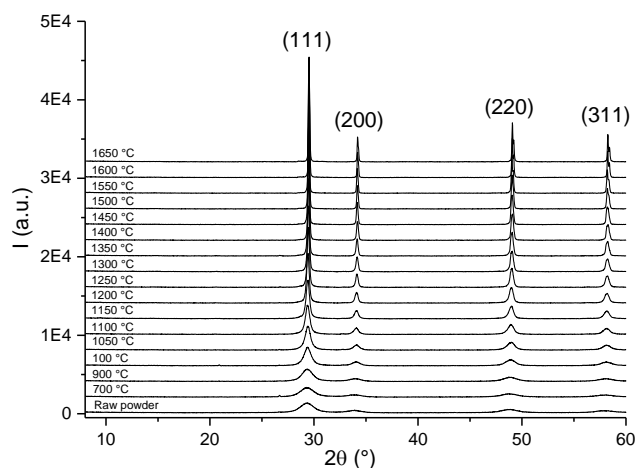


Figure 2: Diffractogrammes de $Y_{2,85}Eu_{0,15}Nb_{0,9}O_{6,75}$ (voie Pechini) en fonction de la température de traitement thermique.

Conformément à ce qui est annoncé dans la littérature, le composé semble stable pour le domaine de température testé et l'ensemble des pics de diffraction observés est compatible avec la symétrie Fm-3m.

La réponse optique des composés issus des différents traitements thermiques a permis d'affiner ces observations. En effet, si la spectroscopie de luminescence des ions europium dans les composés Y_2O_3 et $YNbO_4$ est formée de raies fines caractéristiques des transitions 4f-4f d'un composé cristallisé, l'émission du niobate étudié est, elle, large et mal définie comme cela est illustré sur la figure 3.

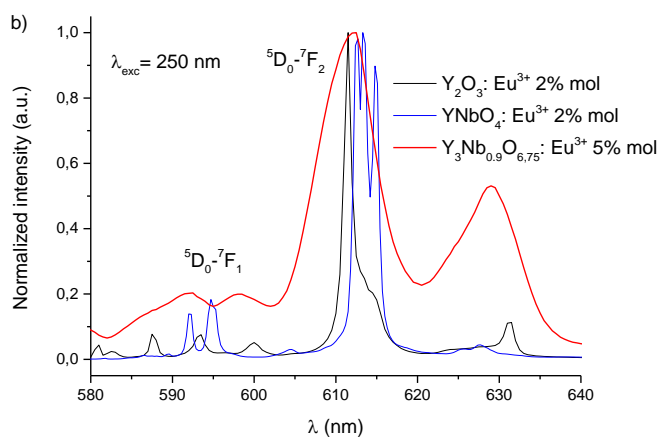


Figure 3: Emission normalisée des ions Eu^{3+} au sein des composés du diagramme binaire $Y_2O_3-Nb_2O_5$ sous une excitation à 250 nm. $YNbO_4:Eu^{3+}$ 2%mol (courbe bleue), $Y_2O_3:Eu^{3+}$ 2%mol (courbe noir) et $Y_3Nb_{0,9}O_{6,75}:Eu^{3+}$ 5%mol (courbe rouge)

Les émissions enregistrées pour une excitation à 250 nm, longueur d'onde favorisant une excitation dans les bandes de transfert de charge de $\text{YNbO}_4:\text{Eu}^{3+}$ et $\text{Y}_2\text{O}_3:\text{Eu}^{3+}$, mettent clairement en évidence la présence de ces phases (pics caractéristiques à 612,5 nm et 611.5 nm respectivement), au sein des poudres traitées thermiquement et cela dès 1100°C (Figure 4). La proportion de ces impuretés est cependant trop faible pour être détectée par diffraction des rayons X. La réponse du niobiate $\text{Y}_3\text{Nb}_{0.9}\text{O}_{6.75}:\text{Eu}^{3+}$ varie quant à elle avec la température pour se déplacer vers les plus basses longueurs d'onde (Figure 5).

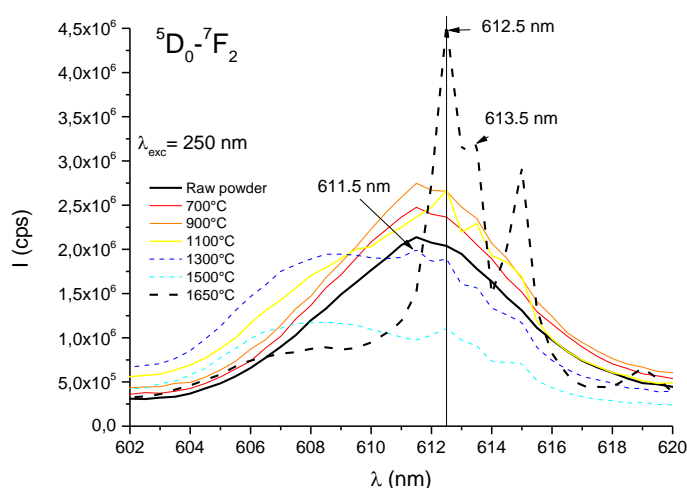


Figure 4: Spectres d'émission à température ambiante des composés $\text{Y}_3\text{Nb}_{0.9}\text{O}_{6.75}:\text{Eu}^{3+}$ 5% mol sous une excitation à 250 nm en fonction du traitement thermique des poudres.

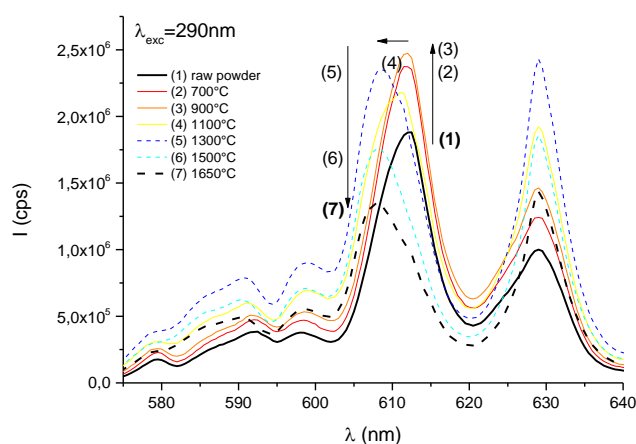


Figure 5: Émission de $\text{Y}_3\text{Nb}_{0.9}\text{O}_{6.75}:\text{Eu}^{3+}$ 5% mol sous une excitation à 290 nm en fonction du traitement thermique des poudres.

Cette modification de répartition spectrale témoigne d'une évolution de la composition globale (rapport Nb/[Nb+Y]) au sein de la solution solide, en accord avec la stabilisation des composés $\text{YNbO}_4:\text{Eu}^{3+}$ et $\text{Y}_2\text{O}_3:\text{Eu}^{3+}$. La largeur spectrale met en évidence un environnement désordonné avec une famille de sites liée à la nature lacunaire en oxygène des polyèdres de coordination autour des ions dopants.

L'étude du frittage du composé Y_3NbO_7 a ensuite été menée, en considérant deux voies de synthèse de la poudre : la voie solide (simple à mettre en œuvre) et la voie Pechini (présentée précédemment). Pour la première, compte tenu des hétérogénéités inévitables à l'échelle des grains dans le mélange de poudre, un simple traitement thermique effectué à 1300°C n'a pas été suffisant pour former la phase Y_3NbO_7 pure. L'utilisation d'un frittage flash de type spark plasma sintering (SPS), combinant température, pression, et champ électrique sur une poudre pré-réagie à 1300°C , a alors été considérée comme un moyen efficace pour obtenir à la fois la formation de la phase et sa densification (frittage-réaction). Pour la voie Pechini, le composé Y_3NbO_7 est obtenu dès 700°C . Dans ce cas, l'étude du frittage SPS a permis de définir les conditions optimales de densification de la phase pure.

Plusieurs paramètres ont été évalués. Nous citerons, les vitesses de chauffe, les durées de palier, les températures de palier, les rampes de refroidissement. Seule la pression a été fixée à 100 MPa pour l'ensemble des manipulations (102 pastilles). Les durées de traitement de ré-oxydation post-SPS ont aussi été étudiées.

Pour le frittage-réaction SPS de la poudre voie solide, nous avons montré que i) des températures élevées, proche de 1600°C , sont nécessaires pour former la phase Y_3NbO_7 , ii) les densités relatives finales sont élevées ($\sim 99\%$), mais pas suffisamment pour obtenir des pastilles transparentes. De plus, pour les temps de frittage les plus longs, les diffractogrammes RX montrent l'apparition de nouveaux pics, caractéristiques d'un début de décomposition de la phase niobiate. Ce point a été analysé plus en détail par la suite.

Pour le frittage SPS de la poudre voie sol-gel, là aussi des températures élevées (1600°C) sont nécessaires pour obtenir de fortes densités finales. Par ailleurs, l'augmentation du temps de frittage ne conduit pas à une amélioration des densités finales et comme pour le frittage SPS des poudres voie solide, la formation de nouvelles phases, est observée en DRX (Figure 6). De même, l'augmentation de la vitesse de montée en température de $5^\circ\text{C}\cdot\text{min}^{-1}$ à $10^\circ\text{C}\cdot\text{min}^{-1}$ puis à $50^\circ\text{C}\cdot\text{min}^{-1}$ fait clairement apparaître une dégradation du composé (Figure 7). Ceci est confirmé par des mesures de luminescence qui prouvent la présence de Y_2O_3 et YNbO_4 au sein des échantillons frittés avec des vitesses de montée en température de 10 et $50^\circ\text{C}\cdot\text{min}^{-1}$. Des résultats similaires sont obtenus pour des traitements de ré-oxydation dont les durées sont supérieures à 6 heures.

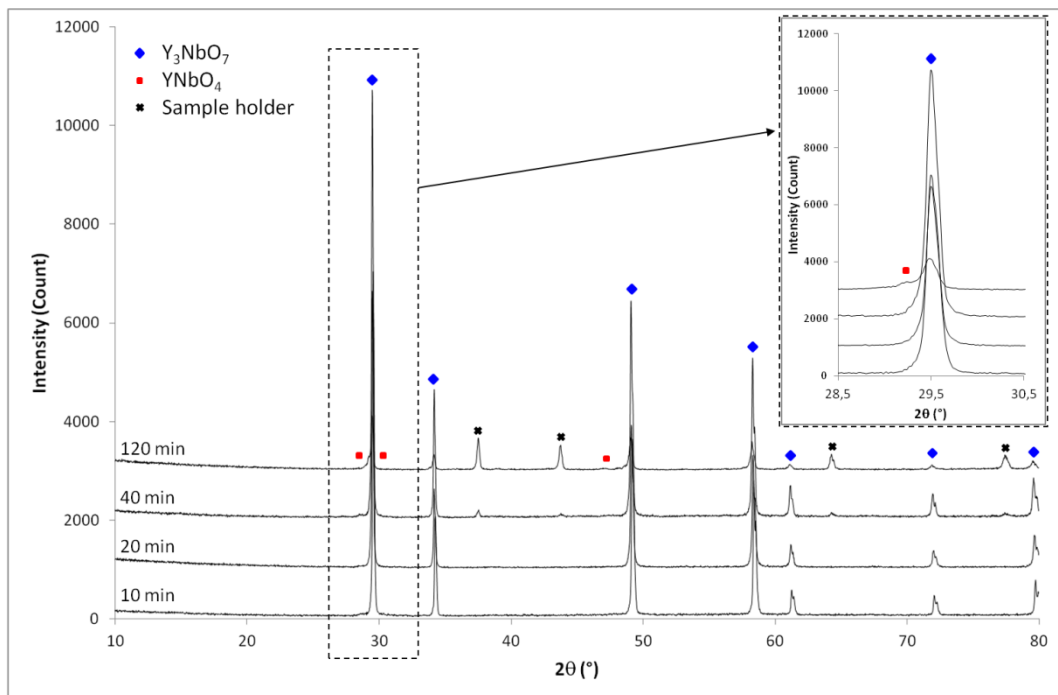


Figure 6: Diffractogrammes des pastilles frittées issues des poudres synthétisées par voie Pechini, à 1600°C avec une vitesse de montée en température de 5°C.min⁻¹ en fonction de la durée des paliers thermiques (10 min, 20 min, 40 min and 120 min).

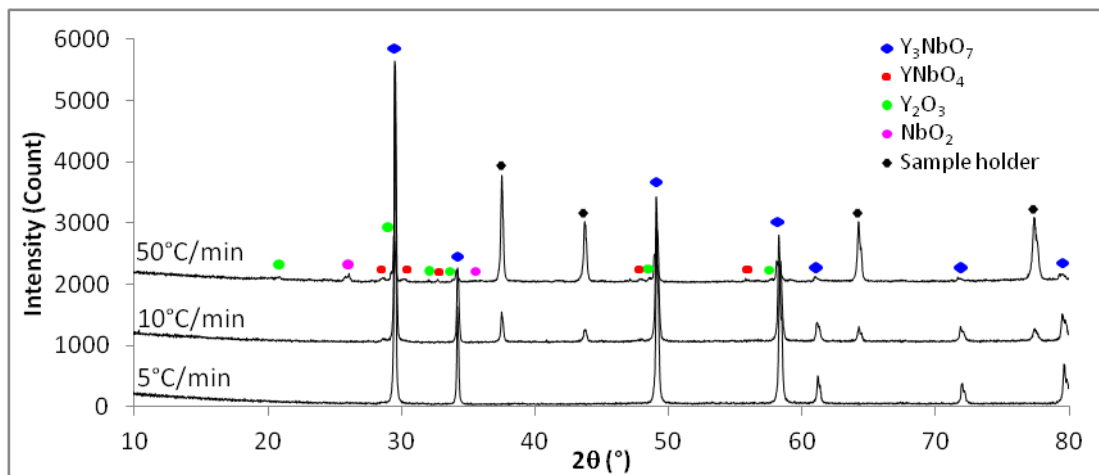


Figure 7 : Diffractogrammes des pastilles frittées issues des poudres synthétisées par Pechini à 1600°C pendant 20 min. (poudre sol-gel) en fonction de la vitesse de montée en température.

Il apparait donc que le frittage SPS de Y_3NbO_7 peut conduire à une décomposition de cette phase selon la réaction suivante: $Y_3NbO_7 \rightarrow YNbO_4 + Y_2O_3$. D'après le diagramme d'équilibre des phases de $Y_2O_3-Nb_2O_5$, le composé Y_3NbO_7 est censé être stable jusqu'à sa fusion congruente qui est supérieure à 2100°C. Dans les conditions du frittage SPS, non seulement une pression mais un champ électrique intense est appliqué à l'échantillon. Le courant joue certainement un rôle important comme cela est mis en évidence pour la pastille frittée avec une vitesse de chauffe de 50°C.min⁻¹. Cet échantillon n'est pas

dense (frittage trop court) mais montre un début de décomposition. Dans ce cas, pour assurer la rampe en température très rapide, un courant de forte intensité est appliqué qui peut induire des phénomènes de conduction ionique et donc favoriser la décomposition de la phase Y_3NbO_7 .

Cette étude de frittage montre que les conditions expérimentales de densification du composé Y_3NbO_7 par frittage SPS sont très contraintes. Nous avons toutefois réussi à optimiser le cycle de frittage afin d'obtenir une céramique dense et pure (densité relative finale de l'ordre de 99 % de la densité théorique, sans trace de Y_2O_3 ou de $YNbO_4$) :

- vitesse de montée en température de $5^\circ\text{C}/\text{minute}$ jusqu'à 1600°C
- palier à 1600°C pendant 20 minutes
- pression de 100 MPa appliquée dès le début du cycle de frittage

Les différents matériaux ont ensuite été caractérisés par spectroscopie de luminescence. Les répartitions spectrales des ions europium trivalent ont permis de mettre en évidence une faible émission de matrice (mesures effectuées à 4 K), une forte extinction configurationnelle et plus étonnamment, deux signatures optiques bien distinctes, preuve de l'existence d'environnements cationiques différents autour des ions dopants (Figure 8).

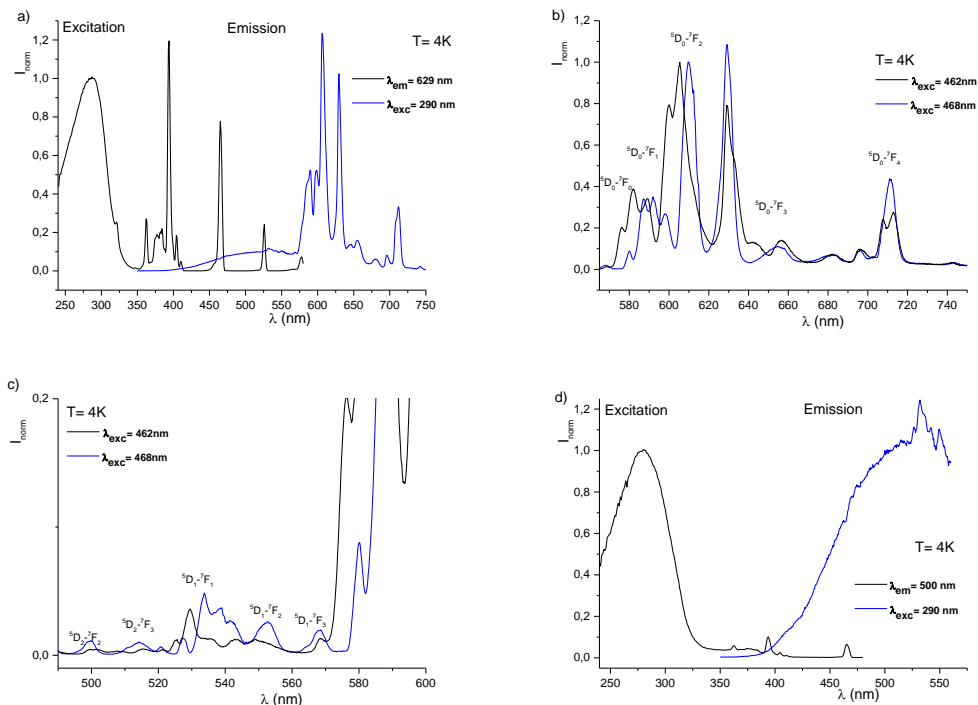


Figure 8 : Luminescence à basse température des ions Eu^{3+} au sein de la matrice Y_3NbO_7 (pastille - 4 K). Le spectre d'excitation, illustré en a-gauche), montre la contribution de la bande de transfert de charge (BTC) Eu-O. Des spectres d'excitation dans la BTC ou dans les raies 4f sont représentées en a-droite) b) et c) respectivement. d) illustre l'émission intrinsèque de la matrice.

Les études structurales des composés TR_3NbO_7 (TR, terre rare) mettent en évidence trois symétries cristallines, selon la taille du cation de terre rare. Pour les valeurs les plus élevés (La - Nd), TR_3NbO_7 cristallise dans le groupe d'espace Pnma. Les phases formées avec les ions Sm^{3+} - Tb^{3+} adoptent une maille élémentaire de groupe d'espace $C222_1$. Les terres rares de plus petites tailles (Dy-Lu) donnent lieu, elles, à des mailles de type fluorine. Des études de microscopie électronique poussées sur ces dernières phases révèlent, en fait, l'existence de nano-domaines dont les taches de diffraction seraient compatibles avec le groupe pyrochlore Fd-3m. Des études complémentaires de spectroscopie Raman confirmeraient l'existence de modes de vibration non compatibles avec la symétrie fluorine.

Concernant la phase Y_3NbO_7 dopée par des ions Eu^{3+} , les rapports entre les transitions dipolaires magnétiques et électriques excluent la stabilisation des ions dopants dans des environnements correspondant aux polyèdres de coordination d'une matrice de type pyrochlore, structure dérivée d'une maille de type fluorine. Après avoir vérifié que la substitution des ions yttrium par des ions europium ne modifie pas la symétrie de la maille cubique, nous avons réalisé des affinements structuraux obtenus à partir d'une pastille broyée (post-traitement plus long pour favoriser la croissance granulaire). Le diffractogramme obtenu confirme la cristallisation de la maille selon le groupe d'espace Fm-3m. Cependant, aux grands angles, un dédoublement des pics de diffraction, témoin d'une démixtion de la solution solide de départ en deux mailles élémentaires fluorine, est clairement visible (Figure 9).

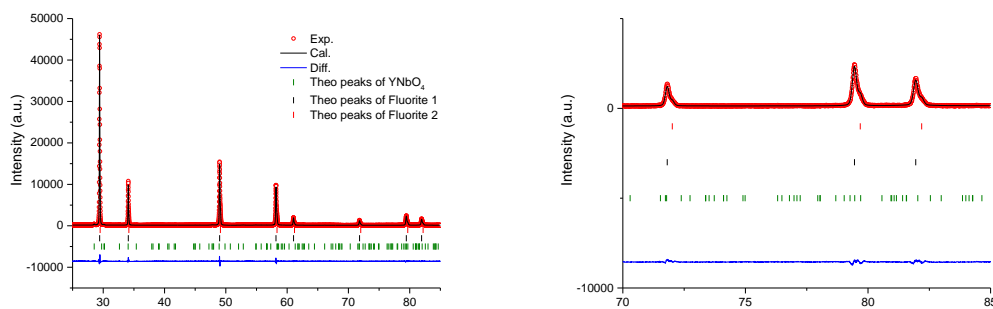


Figure 9- Affinement structural de Y_3NbO_7 : Eu^{3+} 5% fritté à $1600^\circ C$; zoom du domaine aux grands angles.

Les paramètres de maille obtenus ($a_1= 5.2531(1)$ Å et $a_2= 5.2402(2)$ Å) se répartissent de part et d'autres de la valeur que pourrait donner la loi de Vegard publiée par J.H Lee et al.

Par ailleurs, la phase Y_3NbO_7 a été étudiée pour ses propriétés de conductivité ionique. Dans le cas présent, l'utilisation du SPS entraîne une mobilité des ions qui se traduit par la stabilisation d'un composé plus pauvre en niobium (taux proche de 23-24%) et d'une phase

plus riche en niobium (taux de niobium proche de 29%) que la composition initiale. La phase riche en niobium est présente de façon minoritaire dans la pastille frittée.

Un complément d'étude a donc été mené afin de déterminer si cette démixtion était la conséquence du traitement à haute température (1600°C) ou si elle résultait d'un effet du courant associé à la mise en forme par SPS. Les données structurales et spectroscopiques obtenues sur des matériaux pulvérulents traités à 1600°C dans un four n'ont révélé aucune démixtion de la solution solide de type fluorine. Nous en avons donc déduit que les effets observés sont liés au courant inhérent à la technique de frittage SPS. Les caractéristiques des pastilles obtenues nous permettent finalement de conclure qu'il existerait une lacune de miscibilité dans le diagramme de phase proposé dans la littérature, les deux compositions mises en évidence lors de ce travail représentant les limites de ce domaine.

Table of Contents

Chapter 1 - Introduction - General context on optical ceramics	1
1.1. Economic interest	1
1.2. Sintering technique devoted to the preparation of optical ceramics	2
1.3. Single crystals versus ceramic	4
1.4. State of art on laser ceramic development	6
1.4.1 Garnet matrices	7
1.4.1.1: YAG (yttrium aluminum garnet) ceramics	7
1.4.1.2 LuAG (lutetium aluminum garnet) ceramics	9
1.4.2 Al ₂ O ₃ Alumina ceramics	12
1.4.3 Aluminum oxynitride (AlON) ceramics	14
1.4.4 Rare earth sesquioxide ceramics	15
1.4.4.1 Lu ₂ O ₃	15
1.4.4.2 Y ₂ O ₃	16
1.4.5 MgAl ₂ O ₄ spinel ceramics	17
1.4.6 Fluorite matrices	18
1.4.6.1 CaF ₂	18
1.4.6.2 Lu ₃ NbO ₇	20
1.5. Discussion	21
References	23
Chapter 2- Experimental results and discussion	29
2.1 Synthesis and characterization of Eu ³⁺ doped Y ₃ NbO ₇ powder	29
2.1.1 Introduction	29
2.1.2 Experimental step results and discussion	30
2.1.2.1 Synthesis	30
2.1.2.1.1 Solid state route	30
2.1.2.1.2 Self-combustion	31
2.1.2.1.3 Mineral Sol-gel (Pechini) route	31
2.1.2.1.4 Comparison of powders issued from the 3 syntheses	32
2.1.2.2 X-Ray diffraction analyses	33
2.1.2.3 Structural characterization- Effect of temperature	36
2.1.2.4 Luminescence characterization- Effect of temperature	39
2.1.3 Intermediary conclusion	45

2.2 Spark plasma sintering of Y_3NbO_7 : Eu phase	47
2.2.1 Introduction	47
2.2.2 Experimental results and discussions	48
2.2.2.1 Synthesis	48
2.2.2.2 Sintering setup	48
2.2.2.3 SPS sintering of powders obtained from solid state route	48
2.2.2.4 SPS sintering of powders obtained from Pechini route	50
2.2.2.5 Influence of the reoxidation step	53
2.2.2.6 Optical characterization of the SPSed pellets	54
2.2.3 Discussion	54
2.2.4 Intermediary conclusion	56
2.3 Tailoring of the composition and optical properties of Eu^{3+} doped- Y_3NbO_7 niobate induced by spark plasma sintering	59
2.3.1 Introduction	59
2.3.2 Experimental results and discussion	59
2.3.2.1 Synthesis	59
2.3.2.2 SEM pictures	60
2.3.2.3 Luminescence characterization	61
2.3.2.4 X-ray diffraction	66
2.3.2.5 Electron diffraction	69
2.3.2.6 Discussion	71
2.3.3 Intermediary conclusion	73
2.3.4. Luminescence of Ho^{3+} doped Y_3NbO_7	73
References	75
Chapter 3 – Conclusion	81

Chapter 1

Introduction - General context on optical ceramics

1.1. Economic interest

Emitting materials and all solid state lasers are widely used in the field of optical applications and materials science as excitation sources, instrumental measurements [Hering 2004], medical applications [Lubatchowski 2007], metal shapings [Dahotre 2008], and emitting sources for laser printings and projectors [Deter 2000]. Three types of materials such as glasses, crystalline fibers or crystals (blade cylinder) are traditionally used. However, ceramics and glass ceramics are now also regarded as emission and gain media [Ikesue 2008]. To produce ceramics, various factors should be considered such as concentration gradient of doping element or sandwich pellet in which non doped and doped phases can be alternated.

There are different aspects to be considered for commercialization. In the specific market of infrared laser materials, in particular, solid amplifying materials, semiconductor laser diode, is widely used to produce semiconductor laser diode. Commercial gain materials traditionally doped Yb^{3+} , Nd^{3+} or Er^{3+} emit the light in the near infrared between 980 nm and 1500 nm. These materials are easy to use and easy to fabricate in an industrial scale [Nolte 1997][Loesel 1998][Innerhofer 2003][Limpert 2003][Hönninger 2005][Killi 2005].

The current solid materials are well covering the mean infrared region. However, there is a limited number of materials in visible or mid-infrared wavelengths.

Recently, rare earth elements such as terbium and praseodymium have attracted much attention for the visible range [Richter 1963][Chang 1963][Cornacchia 2007][Cornacchia 2008]. There is indeed an area called "green gap" between 535 nm and 640 nm, which cannot be generated by the semiconductor laser diodes or by doubling Ti-Sapphire laser frequency. There is a gap between 500 and 700 nm. For instance, Praseodymium ions can be used to create enough gain and powder, when pumped by blue GaN LEDs, for laser development. By introducing new host lattice with low phonon energy, Pr-doped compounds would cover from orange to red wavelengths.

Rare earth materials such as erbium, thulium and holmium have transitions at around 2 microns in the mid-infrared range. Emissions around 2 μm allow to pump $\text{Cr}^{2+}:\text{ZnSe}$ [Sorokin 2007][Stoeppler 2012], which open the new wavelengths of 3-5 μm . This spectral window of 3-5 μm is of great interest for the defense sector.

Current studies focus on bulk crystals, which performances should be identical to those already tested for emissions at 1 micron. There is, therefore, a great challenge in order to expand the current range of laser wavelengths based on the same material. In addition, crystal growth processes like Bridgman, Czochralski, etc..., require expensive and longtime consuming techniques. Ceramic materials can be used to obtain crystallized materials of lower cost and competitive performances. At present, the main drawbacks of ceramics are the optical losses due to scattering. Actually, Rayleigh scattering induces critical losses in the visible. But this effect is considerably reduced in the mid-infrared which is compatible with our main area of interest, directed towards the infrared range.

1.2. Sintering technique devoted to the preparation of optical ceramics

The choice and optimization of the sintering process are the key points to fabricate transparent ceramics in visible or mid-infrared. It includes a precise control of powder preparation with the choice of an adequate synthesis, pre-heat-treatment, reproducibility of the sintering cycle, polishing, and post-annealing of the ceramic. The densification is the main factor needed to reach the satisfying transparency.

Densification of powder materials has been successfully demonstrated by various sintering techniques such as vacuum sintering (VS) [Jin 2010], hot-pressing (HP) [Podowitz 2010], hot-isostatic pressing (HIP) [Goldstein 2009][Mouzon 2009], spark plasma sintering (SPS) [An 2011-1][An 2013][Fu 2013][Morita 2015][Li 2016] plasma-activated sintering (PAS) [Groza 1992], or pulse electric sintering (PECS) [Zhou 2003] etc.

The VS is the one of the traditional sintering processes. This technique achieves better results than natural sintering under atmospheric pressure. The HP and HIP are low-strain-rate processes. Their main advantage is to strongly reduce the internal porosity. Sintered pellet can reach a relative density of 99.9%. Then, fast heating processes (SPS, PAS or PECS) are listed in table 1.1. They can achieve high densification of $\geq 99\%$ in relatively short time. In contrast, VS process requires a long time treatment at high temperature to obtain good results. HP and HIP need sintering times longer than SPS but still shorter than VS.

Table 1.1- Examples of different sintering conditions

Sintering Method	Materials	Sintering temperature	Dwell time	Pressure	Density (%)	Ref.
VS	ZrO ₂ -doped Y ₂ O ₃	1730-1900°C	5-15h	2 x 10 ⁻³ Pa		[Jin 2010]
HP	Eu doped Y ₂ O ₃	1580°C	8h	40MPa	90~99	[Podowitz 2010]
HIP	Y ₂ O ₃	1500-1625°C	2h	200MPa	99.5	[Mouzon 2009]
SPS	Y ₂ O ₃	1100-1550°C	45min	100MPa	98~99	[An 2012-1]

Some of these sintering processes result in carbon contamination due to the graphite present in the furnace. So, after the process, the materials are often annealed under oxygen or air environment. Some examples are listed in table 1.2.

Table 1.2- Post annealing treatments applied on SPS and HP pellets

Sintering Method	Material	Sintering temperature	Annealing temperature	Annealing time	Atmosphere	Ref.
SPS	Y ₂ O ₃	1300-1500°C	1050°C	6h	Air	[An 2012-1]
SPS	Al ₂ O ₃	1150°C	1000°C	10min	Air	[Krell 2003]
SPS	Lu ₂ O ₃	1450°C	1050°C	12h	Air	[An 2011-2]

Lu *et al* [An 2012-1] investigated the effects of post-annealing treatments on Y₂O₃ ceramics sintered at three different temperatures: 1300°C, 1400°C and 1500°C. Fig.1.1 shows the difference between non-annealed and post-annealed ceramics (1050°C, 6 hours in air). Fig.1.2 shows the transmittance graph of Y₂O₃ bodies, which is sintered at 1200–1500°C with post-annealing at 1050°C and 6 hours in air. The increase of the heat-treatment temperature first improves the transparency. Oxygen vacancies are stabilized under vacuum during SPS which results in a grey color of the pellet. After annealing, the oxygen vacancies can be removed and the UV absorption edge is blue shifted. The highest transmittance was occurred with Y₂O₃

bodies sintered at 1300°C. Above this temperature a degradation of the pellet occurs reducing the pellet transmission.

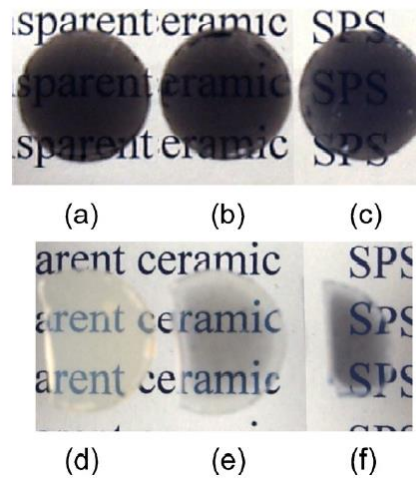


Figure 1.1. Micrographs of Y_2O_3 ceramics sintered at (a) 1300°C, (b) 1400°C and (c) 1500°C before annealing and after post-annealing treatment at 1050°C for 6 h in air: (d) 1300°C, (e) 1400°C and (f) 1500°C sintering. [An 2012-1]

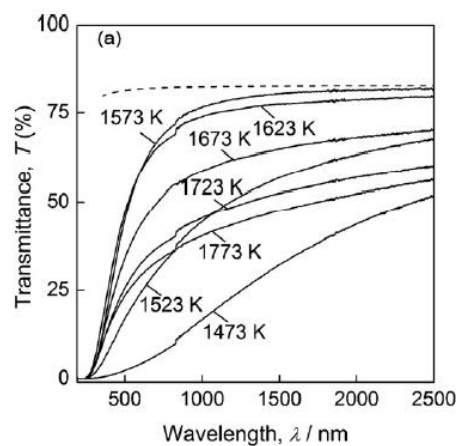


Figure 1.2. Transmittance of Y_2O_3 bodies sintered at 1473–1773 K (1200–1500°C) after annealing at 1323 K (1050°C) and those calculated from the refractive index of an Y_2O_3 single crystal (dashed line). [An 2012-1]

1.3. Single crystals versus ceramic

The stimulated emission was first observed on a ruby crystal, doped with chromium in corundum by Maiman 55 years ago [Maiman 1960]. Many researches on various doped materials with transition ions (Ti^{3+} , Cr^{3+}) or rare earth ions (Nd^{3+} , Yb^{3+} , Tm^{3+} , Er^{3+} , Ho^{3+}) have been carried out, leading considerable development of solid laser materials. Among the laser materials, garnet matrices, Nd:YAG [Rabinovitch 2008] (YAG = yttrium aluminum garnet, i.e. $Y_3Al_5O_{12}$), tungstates, Yb:KGW ($KY(WO_4)_2$) [Kasproicz 2011], sesquioxides, and Yb:RE₂O₃

(RE: rare earth) [Takaichi 2007] have been actively investigated. The development of amplifying media has accelerated in the 80s with the help of large sales of laser diodes based on semiconductor materials [Bour 1989].

To obtain crystals of large sizes ($> \text{cm}^3$), compounds having a congruent melting are required. The limitation of the growth process by pulling is the melting temperature. YAG and REVO₄ vanadates (RE = Y, Gd) crystals are obtained by Czochralski pulling. KRE(WO₄)₂ tungstates (RE = Y, Gd) are usually prepared from "top seed solution growth" technical by flow methods. HEM techniques (Heat Exchanger Method) allow the production of titanium sapphire crystals that may produce large dimensions. In this case, the temperatures could be as high as 2450°C and the crystal growth requires rhenium crucibles. Therefore, difficult and expensive processes are needed to grow high quality refractory materials.

The development of sintering technology appears as another alternative to prepare massive optically active compounds. Considering in particular recent laser performances with ceramic materials, this pathway is credible to address new materials for future markets, avoiding the difficulties of the conventional crystal growth methods [Bonnet 2015][Boulesteix 2014].

With excellent optical and mechanical properties, optical ceramics can be used as transparent media in hostile environments such as visible/IR window, high intensity discharge lamps, scintillator, optical lens, electron microscope domes and transparent armor for solid-state lasers [Peuchert 2009][Klement 2008][Choi 1990][Cherepy 2007].

Their application fields are numerous. One of them could be laser amplification. The efficiency of a solid state laser could be different depending on different criteria. The material must be obtained with a large size (mm to cm at least) and a sufficiently high optical quality so that free areas of defects and scattering centers can be selected. Moreover, polishing steps require good mechanical properties and a certain thermal and chemical stability. The material must have good durability under flux as well as a good thermal conductivity for eliminating local heating. The variations of refraction index or nonlinear indices of non-centrosymmetric materials can affect the geometry of the laser beam and lead to self-focusing phenomena, resulting in localized thermal effect.

The indispensable prerequisite for obtaining optimum transparency of ceramics is the degree of densification, as already mentioned. But the intrinsic thermal conductivity decreases also in a sintered ceramic, which can also affect strongly the gain value. It is then important to select proper materials with a good thermal conductivity. YAG has for instance a thermal conductivity of 9.5~14.5 W/mK [Wechsler 2000]. The materials are also supposed to have high strength, hardness, and high temperature stability.

For improving the mechanical properties such as strength and hardness, grain size is an important factor to control during the sintering process. However, this has also an impact on the transparency. The transmission of the ceramic must achieve levels above 99 %. Therefore,

all closed porosity should be removed [Boulesteix 2013]. The optimization of diffusion losses also requires ceramics with a nanoscale microstructure, generally less than one hundred of nanometers. In addition, symmetry of the unit cell plays a crucial role in the diffusion rate of the material. Therefore, compounds with a cubic symmetry, having an isotropic refractive index, is preferred. In this case, grain growth is not an obstacle to obtain good transparency.

Comparing with single crystals, it should be emphasized that ceramics have advantages such as chemical homogeneity, lower fabrication temperature, higher doping concentration and feasibility for laser size specimen than single crystal.

1.4. State of art on laser ceramic development

Manufacturing translucent ceramics began in the 50s [Coble 1961] and continued in the 70s [Anderson 1970][Greskovitch 1973], but the first laser performance was recorded on a ceramic in 1992 [Ikesue 1992]. The development of chemistry synthesis routes led to the optimization of powders and densification, giving rise to the transparency thresholds required for optical applications [Dupont 2004]. Current sintering techniques can produce high quality transparent ceramics. Since their properties are close to crystal ones, the ceramic method is a credible substitute of the conventional crystal growth methods. It should allow exotic geometries for the next-generation of commercialized laser materials.

In order to fulfil the requirements of optical applications, the following compounds have been developed: YAG, LuAG garnets [Lu 2002][Frage 2010][Li 2011] [Cheng 2010][Yang 2012][Wang 2014][Kamada 2009][An 2012-2][Kuwano 2004][Xu 2013][Yang 2014][Zhang 2004], Al₂O₃ [Krell 2003][Kim 2009], ALON [Chen 2014-1], Y₂O₃, Lu₂O₃ sesquioxides [An 2011-2] [Seeley 2011][Dutta 1969][Hou 2011][Li 2009], MgAl₂O₄ spinel [Bonfont 2012][Wang 2009][Sanghera 2011], CaF₂ [Chen 2014-2][Lyberis 2012] and more recently Lu₃NbO₇ fluorites [An 2011-1][An 2013]. The following figure illustrates the evolution of transparent ceramics in the last decades (Fig. 1.3).

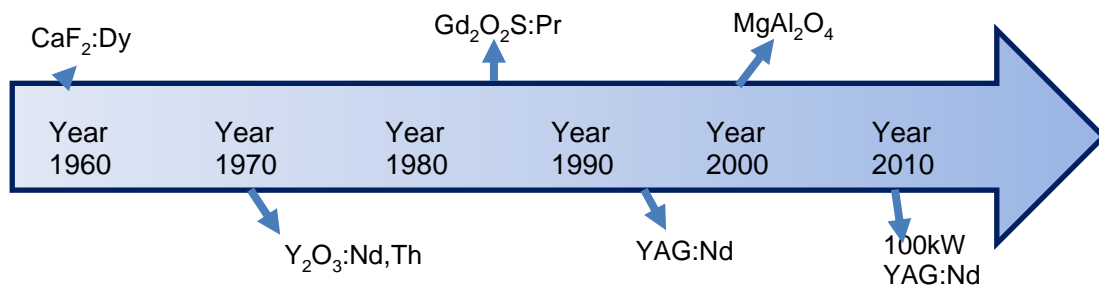


Figure 1.3. A timeline of some major accomplishments for the transparent ceramics [Chen 2013]

1.4.1 Garnet matrices

1.4.1.1: YAG (yttrium aluminum garnet) ceramics

The results presented below clearly show that the quality of transparent polycrystalline of Nd:YAG ceramics have made great improvements in past years.

J.Lu *et al* [Lu 2002] reported the fabrication of nano-crystalline Nd:YAG ceramics using the fabrication process described in Fig.1.4. The precursor was calcinated at 1200°C and the powder was sintered under vacuum at 1750°C for 5 ~20 hours. Fig. 1.5 shows a micrograph of the obtained Nd:YAG ceramics of good optical quality.

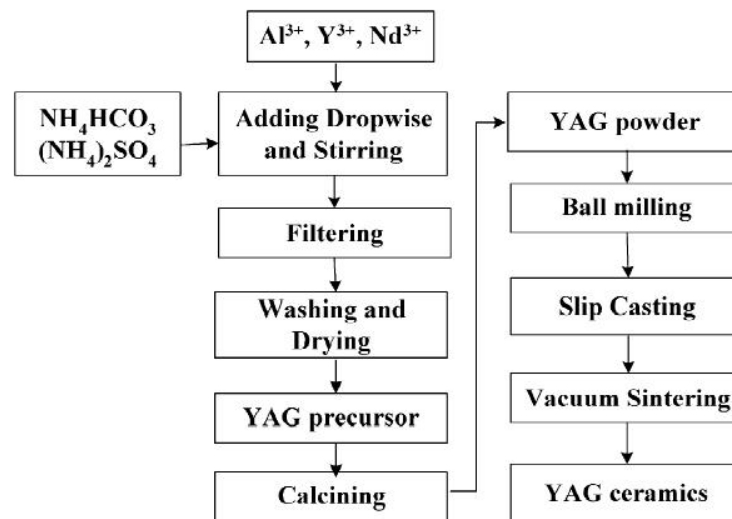


Figure 1.4. Scheme strategy of the fabrication of Nd:YAG ceramics [Lu 2002]

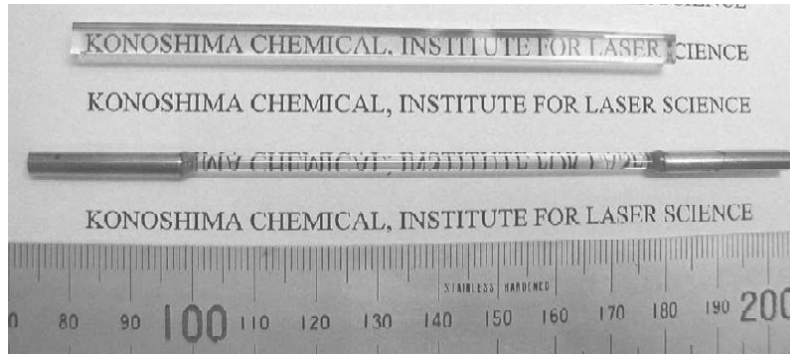


Figure 1.5. Micrograph of Nd:YAG laser ceramics shaped as rods [Lu 2002]

N.Frage *et al.* [Frage 2010] studied YAG sintering by spark plasma sintering (SPS). To fabricate transparent polycrystalline YAG, nano-size YAG powder was prepared by using 50 nm average size particles with purity of 99.985%. LiF was added during the preparation in order to evaluate its effect on transparency. For comparison, powders were prepared through two synthetic routes. The first one is LiF free and the other one is a co-mixed preparation with a LiF content 0.25 wt.%. YAG ceramics with LiF additive achieved nearly full densification after a 2hours heat treatment at 1300°C under 80 MPa. LiF addition has a positive effect on the densification and also on the removal of residual carbon which contributes to contamination of the medium. It is obviously shown in Fig. 1.6.

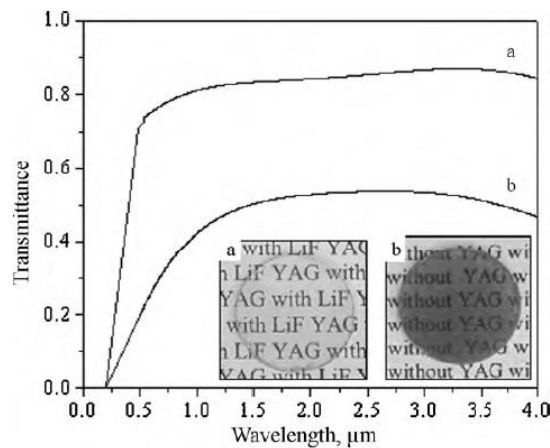


Figure 1.6. Transmittance of YAG ceramics (a) with and (b) without LiF [Frage 2010]

Concerning the optical performances of these garnet host lattices, Nd doped YAG ceramic was tested in 1995 for a successful outcome with respect to the bulk crystal. Recently, an output power of 1.47 kW [Lu 2002] was extracted with an efficiency of only 15% below the value of the corresponding single crystal. Other authors generated an output power of 425 W

in a cylindrical Nd:YAG ceramic with a pump power of 1kW, which corresponds to a conversion efficiency of 42.5% [Li 2011]. A pumping at 1,907 nm of a Ho:YAG ceramic has achieved a 60% efficiency (output power of 20 W), which is comparable to the performance recorded on crystal [Cheng 2010].

Fig.1.7 illustrates the dependence of output power versus pump power for a Nd:YAG single crystal and a ceramic laser. An output power of 1.72 kW with an optical-to-optical conversion efficiency of 49% could be obtained. For Nd:YAG single crystal, Toshiba Corporation, Japan, showed an optical-to-optical conversion efficiency of 42% for Nd:YAG ceramics with 1.46kW pumping power. In this graph, Nd:YAG ceramic laser efficiency is inferior to that of Nd:YAG crystal laser. However, quality improvement of Nd:YAG ceramic laser is really promising.

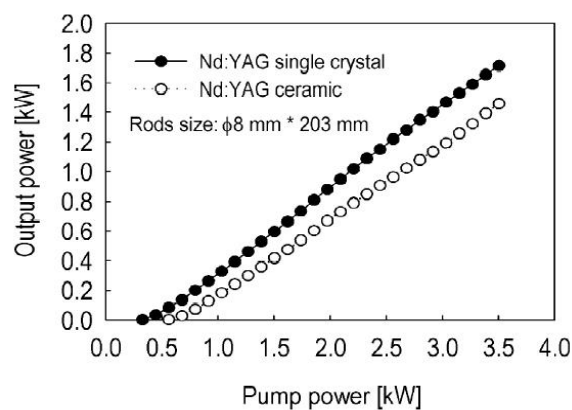


Figure 1.7. Laser output as a function of pump power of Nd:YAG ceramic and single crystal laser [Lu 2002]

1.4.1.2 LuAG (lutetium aluminum garnet) ceramics

$\text{Lu}_3\text{Al}_5\text{O}_{12}$ (LuAG) is isostructural to yttrium aluminum garnet (YAG). A research work reported the optical properties of LuAG single-crystals grown by Czochralski method [Kamada 2009]. The transparent LuAG bodies were fabricated by SPS process [An 2012-2]. The starting materials were commercial powders of Lu_2O_3 and $\alpha\text{-Al}_2\text{O}_3$, that were ball-milled in a stoichiometric ratio (Lu:Al=3:5). Temperature was increased up to 1650°C and maintained at this value for a duration of 45 minutes. The final pressure was 100 MPa. Fig.1.8 shows, the micrographs of as-sintered and annealed LuAG bodies for the five different temperatures. The LuAG bodies became more and more transparent with the increase of temperature. Defects like oxygen vacancies might cause the yellow color of as-sintered LuAG bodies. But after annealing under oxidizing atmosphere LuAG bodies became transparent.

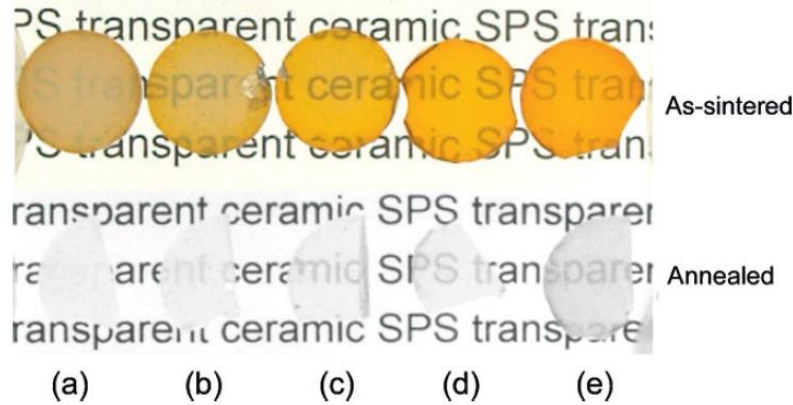


Figure 1.8. Pictures of as-sintered and post-SPS annealed LuAG ceramics at (a)1350°C, (b) 1400°C, (c) 1450°C, (d) 1500°C and (e) 1550°C [An 2012-2]

Fig. 1.9 shows the transmittance spectra of several pellets annealed at 1150°C in the air for 12 hours after the SPS process performed between 1350°C and 1650°C. The dotted line represents the transmittance of LuAG single-crystal in the 410–1970 nm wavelength range [Kuwano 2004]. An improvement of the transmittance is observed in the ultraviolet and visible ranges.

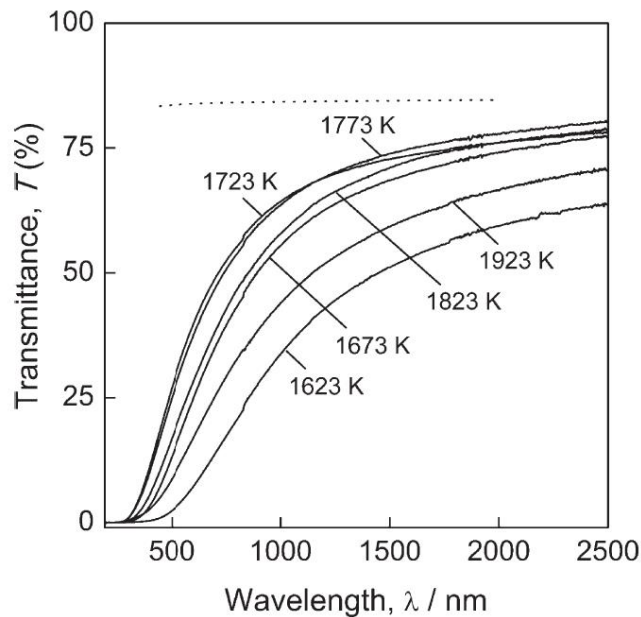


Figure 1.9. Transmittance spectra of LuAG bodies after annealing at 1150°C in air for 12 h (full line). Transmittance of LuAG single crystal in the wavelength range of 410–1970 nm (dotted line) [An 2012-2]

Ce^{3+} doped LuAG is an attractive material for scintillator because of its good physical properties and its high density due to high atomic number elements. Xu et al [Xu 2013] investigated a Ce^{3+} :LuAG (0.5 % molar substitution). The powder was synthesized through co-precipitation method. A vacuum sintering process at 1750°C for 10 h was applied. The

obtained pellets were then annealed at 1450°C for 20 h. The sample densities were close to the theoretical one and the transmittance was 73.48% at 550 nm. Fig.1.10 presents the corresponding Ce³⁺ doped LuAG ceramics.

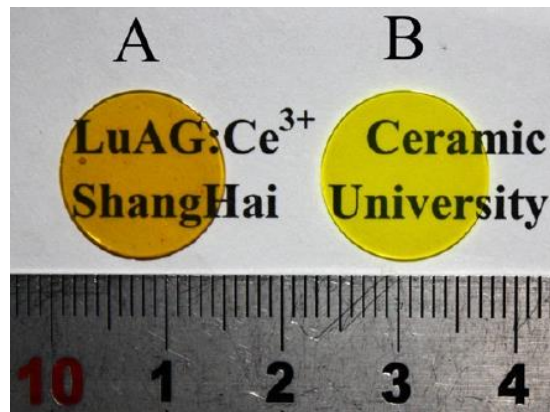


Figure 1.10. (a) Raw ceramic and (b) post-annealed pellet (1450°C, 20 h under air [Xu 2013]

Hao Yang *et al* [Yang 2014] investigated fabrication of isostructural Ho:YAG and Ho:LuAG ceramics. The starting powders were commercial α -Al₂O₃, Lu₂O₃, Ho₂O₃ powders and co-precipitated Y₂O₃ powder. The Y₂O₃ precursor was synthesized using ammonia following the synthetic route described by Zhang *et al* [Zhang 2004]. It was calcined at 1000°C for 3 h in air. The powders were mixed in ethanol (99.99% of purity), ball milled for 15 h and then dried at 120°C for 24 h. The resulting powder was sieved with a 200-mesh. A calcination was then performed at 800°C for 3 h to remove residual organic components. The precursor was first uniaxially pressed under 15 MPa and in a second step under cold isostatic pressure (CIP) at 200 MPa. After CIP, a vacuum sintering process was realized on Ho:YAG and Ho:LuAG materials at 1780°C and 1830°C for 8 h. After sintering, the pellets were annealed at 1400°C during 15 h in air.

Transmittances and micrographs of the transparent Ho:YAG and Ho:LuAG ceramics are shown in Fig.1.11. 83.9% and 84.6% values of Ho:YAG were recorded at 1000 nm and 2500 nm respectively.

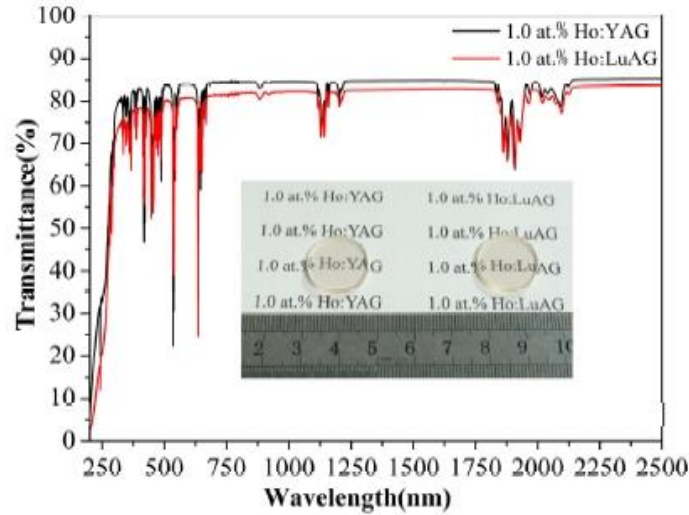


Figure 1.11. Transmissions curves of Ho:YAG and Ho:LuAG ceramics [Yang 2014]

The laser output power as a function of incident pump power is shown in Fig. 1.12. For the 1.0 at.% Ho:YAG ceramic, a maximum output power of 2.97 W under an incident pump power of 11.3 W was generated. A maximum output power of 0.7 W was recorded under an incident pump power of 6.9 W for the Ho:LuAG ceramic. Finally, slope efficiencies of 28.5% and 17.3% were obtained for the 1.0 at.% Ho:YAG sample and 1.0 at.% Ho:LuAG sample, respectively. The output laser wavelengths are centered at 2095 nm and 2100 nm.

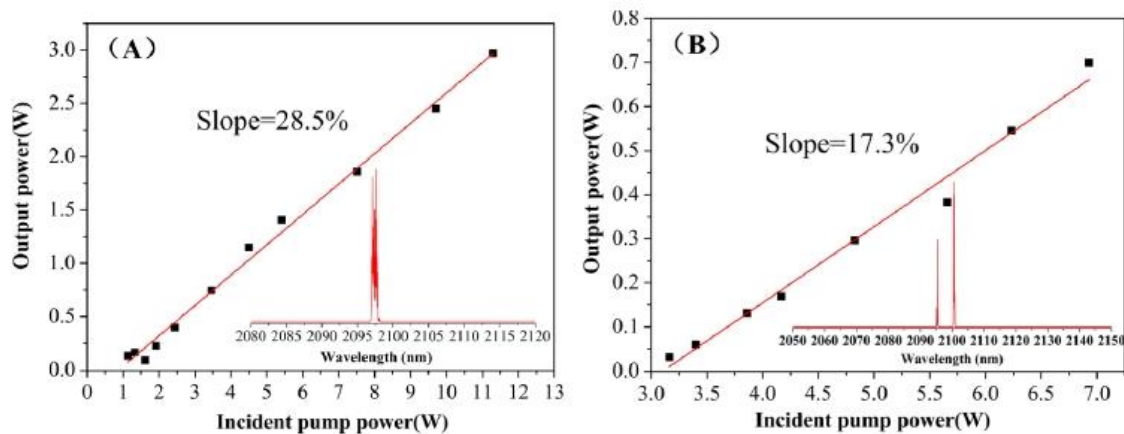


Figure 1.12. Laser output powers of (a) Ho:YAG and (b) Ho:LuAG ceramics [Yang 2014]

1.4.2 Al₂O₃ Alumina ceramics

Alumina ceramics were mainly obtained by using hot isostatic pressing (HIP) and SPS. In the first case (HIP), elimination of pores was effective at 1200-1300°C and relative density \geq

99.9% were obtained. The resulting dense ceramic presented in-line transmission of ~60% at a wavelength of 650 nm [Krell 2003].

B.-N.Kim *et al* [Kim 2009] investigated microstructural changes as a function of the heating rate by using spark plasma sintering (SPS). The starting powder was a commercial α -Al₂O₃ powder with high purity of 99.99%. There was no specific pre-treatment and the powder was directly sintered. Different cycles were tested between 600°C and 1150°C. The authors applied different heating rates between to 2°C/min and 100°C/min under a uniaxial pressure of 80 MPa. The targeted temperature was held during 20 minutes. A post annealing treatment was then performed at 1000°C during 10 minutes. Fig 1.13. shows that grain size of alumina ceramic was smaller at the lowest heating rate. One should also note that porosity is still present when the fastest heating rate was used.

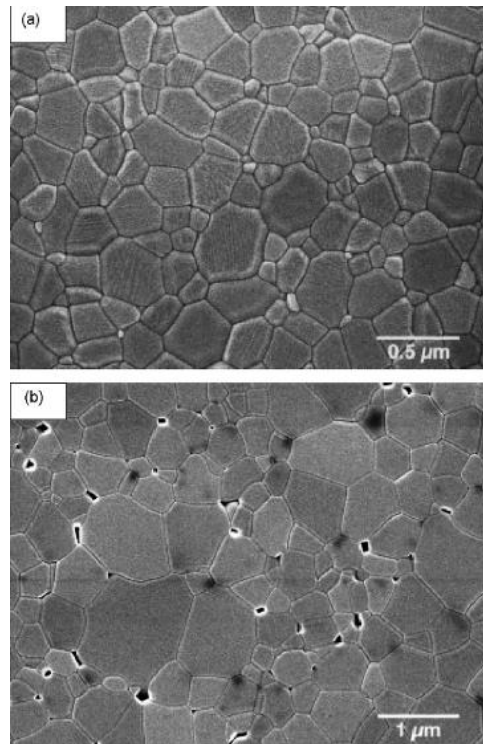


Figure 1.13. SEM micrographs of the microstructure of alumina pellets sintered at 1150°C with a heating rate of (a) 2°C/min and (b) 100°C/min [Kim 2009]

Grain size and residual porosity are closely connected with optical and mechanical properties. The alumina ceramics sintered at different heating rate are presented in Fig.1.14. An improvement of transparency is observed when the lowest heating rate was used. The best result for these alumina ceramics was obtained when the heat treatment temperature was at 1150°C during 20 minutes. The average grain size was equal to 0.29 μm. The transmission was about 46% at 640 nm.

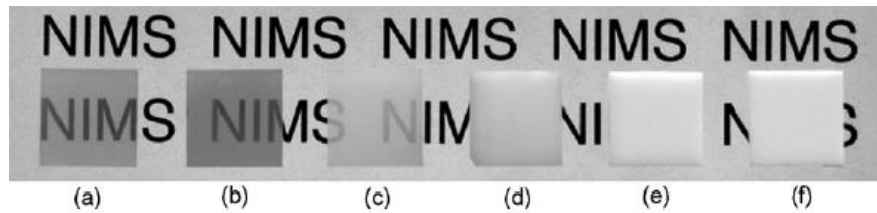


Figure 1.14. Alumina ceramics sintered by SPS at a heating rate of (a) 2°C/min, (b) 5°C/min, (c) 10°C/min, (d) 25°C/min, (e) 50°C/min and (f) 100°C/min [Kim 2009]

1.4.3 Aluminum oxynitride (AlON) ceramics

The aluminum oxynitride (AlON) ceramics consist of a defect cubic crystalline structure of $Al_{(64+x)/3}O_{32-x}N_x$ ($2 \leq x \leq 5$). F. Chen *et al* [Chen 2014-1], used hot isostatic pressing (HIP) method to elaborate high transparent AlON ceramics. To synthesize, AlON, Al_5O_6N and $Y_2O_3-La_2O_3$ reactants were ball-milled in stoichiometric proportions. The powder mixture was shaped using cold isostatic pressing (CIP) under 200 MPa. Pellets were pre-sintered at 1800°C, 1850°C and 1900°C. HIP process was carried out under Ar (190 MPa) at 1900°C for 2 h. One pellet was also prepared under a lower pressure at 1930°C during 15 h for comparison.

In Fig.1.15, the transmittances of HIPed pellets show that the increase of the pre-sintering temperature leads to higher transparency. The 1900°C pre-sintered pellet possesses a 78.8% transmission at 500 nm and a 84.4% transmission at 1084 nm. The corresponding relative density reaches 99.99%.

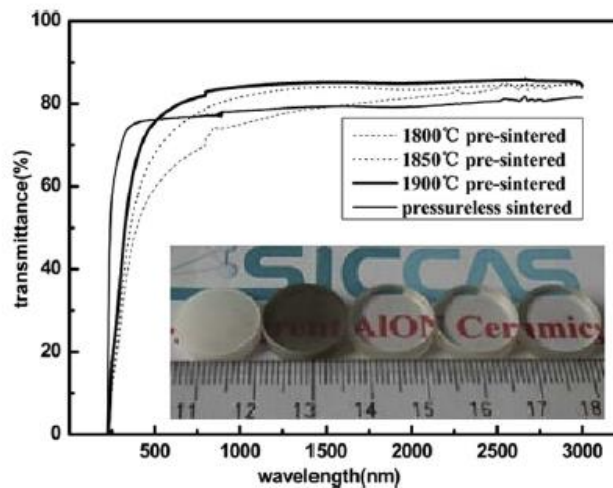


Figure 1.15. Transmittance of a 1900°C HIPed AlON (4.2 mm thick, pre-sintered at 1800, 1850 and 1900°C) compared to pressureless sintered AlON (4.2mm thick, sintered at 1930°C for 15 h). Insert: micrographs of AlON presintered at 1900°C in N_2 (white disk), HIPed at 1900°C in Ar (black disk), and annealed at 1200°C in air (transparent disk), respectively [Chen 2014-1]

1.4.4 Rare earth sesquioxide ceramics

1.4.4.1 Lu₂O₃

L. An *et al* [An 2011-2] prepared ceramics from a commercial high purity Lu₂O₃ powder, using SPS method. Initial powder was ball-milled before the sintering process. The obtained pellets were compared to each other as a function of the ball milling and the SPS post-annealing treatment. The sintering temperature was increased up to 1450°C and maintained for 45 minutes. The pressure was pre-loaded at 10 MPa at room temperature and finally increased up to 100 MPa. The annealing treatment was performed at 1050°C during 12 hours in air. Illustration of final materials is given in Fig.1.16. It can be seen that the higher transparency was obtained from the ball-milled powder with an annealing heat treatment. Indeed, the transmittance was increased from 50 % to 81.6 % at a wavelength of 2000 nm.

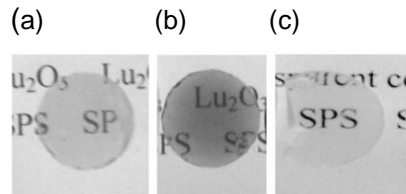


Figure 1.16. Micrographs of Lu₂O₃ ceramics using (a) as-received powder and (b) ball-milled powder without annealing (c) ball-milled powder with annealing at 1050°C for 12h [An 2011-2]

Europium doped lutetium oxide was elaborated by vacuum sintering and hot isostatic pressing by Z.M. seeley *et al* [Seeley 2011]. Nanosize powder was synthesized through spray pyrolysis technique (Flame spray pyrolysis, FSP). The powder was uniaxially pressed before the sintering. Various temperatures between 1575°C and 1850°C were applied during 2 hours. A second sintering process (HIP) was applied at 1850°C for 4 hours under a 200 MPa argon gas pressure. The final sintered material reached a 99 % relative density. Evolution of the pellet aspect is shown in Fig. 1.17. It is clear that the optimized thermal window of the sintering treatment is between 1600°C and 1650°C.

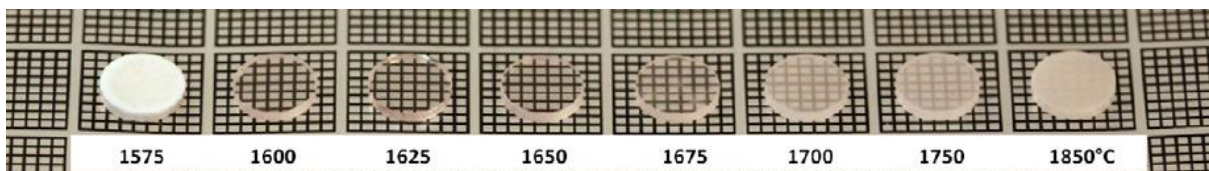


Figure 1.17. Micrographs of Eu doped Lu₂O₃ ceramics obtained by vacuum sintering at 1575-1850°C [Seeley 2011]

1.4.4.2 Y₂O₃

First intent to stabilize transparent Y₂O₃ ceramics was run by S.K. Dutta and G.E. Gazza [Dutta 1969], 50 years ago. In this investigation, a commercial Y₂O₃ powder with a 99.9~99.99 % purity was cold pressed. A first step for the sintering cycle was realized at 300°C-600°C with a heating rate of 5~6°C/min during approximately one hour. During the second step the temperature was raised up to 1300-1500°C with a holding time of about 1~2 hours; the pressure applied ranged between 24.4736~48.263 MPa. After the process, the pellet was annealed at 1000°C under oxygen in order to remove residual carbon. Fig.1.18 shows Y₂O₃ specimens sintered at different temperatures.

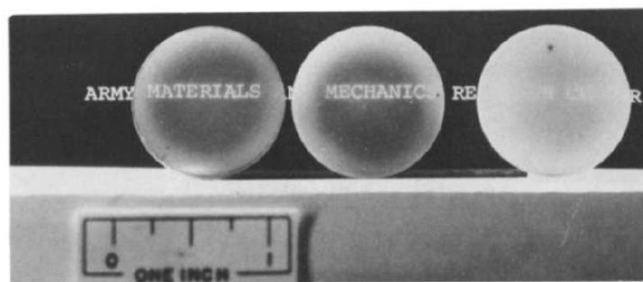


Figure 1.18. Y₂O₃ ceramics, hot pressed at 1300°C, 1400°C, and 1500°C, for 2 hours [Dutta 1969]

Recently, X.Hou *et al* [Hou 2011] made Nd:Y₂O₃ transparent ceramics. The starting powders were prepared by using high purity Y₂O₃ and Nd₂O₃ powders with an addition of 1 mol% of ZrO₂ in order to synthesize the (Nd_xY_{0.99-x}Zr_{0.01})₂O₃ (x = 0.001-0.07) material. The powders were ball milled with ethanol for 24 hours and were dried at 130°C for 24 hours. Pellets were shaped first by using a 10 MPa uniaxial pressure and then a 200 MPa isostatic pressure (CIP). The Nd:Y₂O₃ green bodies were then sintered at 1800°C for 20 hours under a ~ 1.0x10⁻³ Pa pressure. Micrographs of Nd:Y₂O₃ transparent ceramics with different Nd concentrations are shown in Fig 1.19.

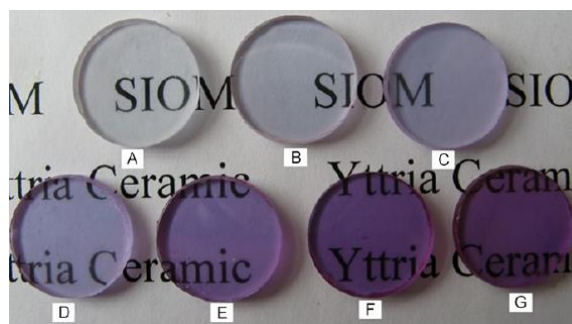


Figure 1.19. Micrographs of Nd doped Y₂O₃ ceramics as a function of Nd concentrations: (a) 0.1 at%. (b) 0.4 at%. (c) 0.7 at%. (d) 1.0 at%. (e) 3.0 at%. (f) 5.0 at%. (g) 7.0 at%. [Hou 2011]

Nowadays, laser tests are performed on such sesquioxide compositions. For instance, a repetition rate of 90.7 MHz mode-locked regime was recorded, for instance, on a Yb:Y_{1.8}La_{0.2}O₃ ceramic [Li 2009].

1.4.5 MgAl₂O₄ spinel ceramics

G. Bonnefont *et al* [Bonnefont 2012] obtained transparent MgAl₂O₄ spinel by using SPS method. The SPS cycle was the following: a fast heating rate (100°C/min) was first applied until reaching 800°C. It was reduced to 10°C/min up to 1100°C and finally fixed at 1°C/min up to 1300°C. A 72 MPa pressure was applied at the beginning of the process and during all the cycle. The obtained transparent MgAl₂O₄ ceramic is presented in Fig.1.20. It has a transmission of 74 % and 84 % in the visible at 550 nm and in the near infrared at 2000 nm, respectively,



Figure 1.20. Micrograph of a sintered MgAl₂O₄ spinel [Bonnefont 2012]

Other sintering experiments were performed by C. Wang and Z. Zhao [Wang 2009]. Commercial high-purity MgAl₂O₄ powder with particle size of 60 nm was used. The temperature was increased up to 600°C within 3 minutes and then increased to 1250°C in 6 minutes. The final 1300°C temperature was held during 3 minutes. After then, two-step pressure cycles were performed. A first pressure (5, 10, 20, 30, 50 or 100 MPa) was applied and kept until 1250°C. It was then increased to 100 MPa in one minute. All sintered MgAl₂O₄ ceramics reached a relative density superior to 99.8%. Fig.1.21 shows the polished corresponding pellets. The highest measured transmission was 51 % at 550 nm and 85 % at 2000 nm. These values were obtained with the lowest initial pressure of 5 MPa.

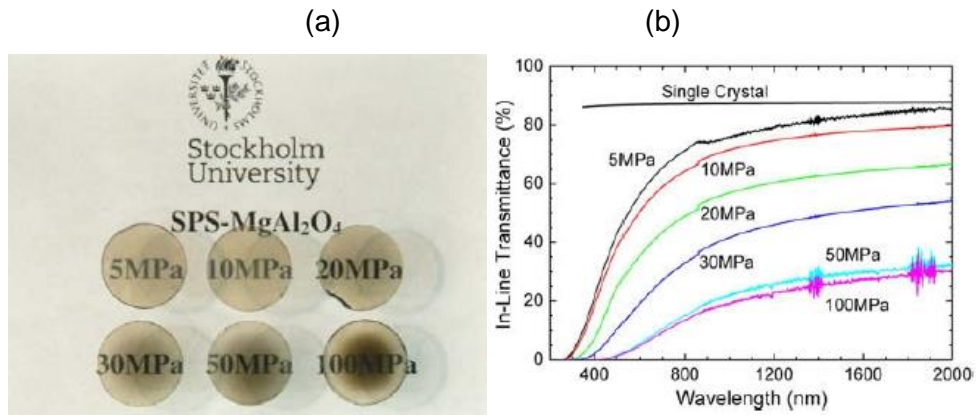


Figure 1.21. (a) Sintered MgAl_2O_4 ceramics obtained with different initial pressures in the SPS cycle, (b) Transmission of five MgAl_2O_4 spinel [Wang 2009]

Transparent MgAl_2O_4 spinel ceramics is now used as a window. J. Sanghera *et al* [Sanghera 2011] succeeded in obtaining transparent spinel ceramics using aqueous chemical methods to synthesized high purity powder. Hot pressing technique was adopted with a temperature of 1400–1650°C for 2 to 4 hours. A small amount of LiF was added. The hot-pressed transparent spinel ceramics were obtained with relative densities higher than 99 %. To obtain fully dense spinel ceramics, a secondary HIP sintering process was applied at 1600°C during 2 hours under Ar gas pressure. The obtained transparent spinel ceramics are illustrated in Fig. 1.22. As it can be seen, large size samples are achieved with this technique.

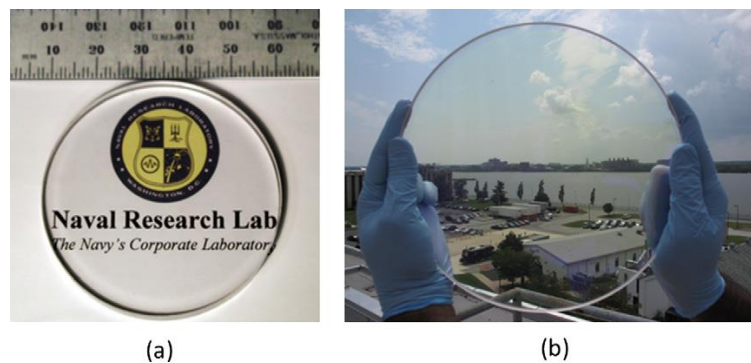


Figure 1.22. (a) Uncoated 5 cm diameter and (b) AR coated 10inch spinel windows [Sanghera 2011]

1.4.6 Fluorite matrices

1.4.6.1 CaF_2

Calcium fluoride ceramics were studied by S.Chen *et al* [Chen 2014-2]. The initial commercial CaF_2 powder has a 97% purity It was used as-received for spark plasma sintering

experiments. The maximum temperature range fixed by the authors was 500–850°C and the pressure was held at 70 MPa. Final result is shown in Fig.1.23. A grey colored pellet is obtained, revealing the presence of defect and/or residual carbon.

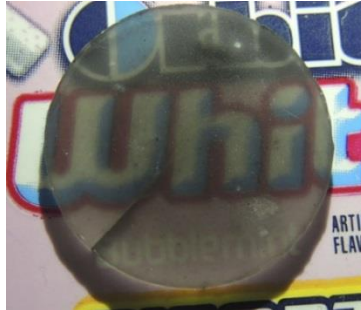


Figure 1.23. Sintered CaF₂ ceramic obtained by SPS at 700°C [Chen 2014-2]

A. Lyberis *et al* [Lyberis 2012] investigated the ytterbium doped fluorite system (Yb:CaF₂). Commercial water soluble salts such as calcium nitrate (99.98%) and ytterbium nitrate (99.999%) were dissolved in water. The Yb:CaF₂ fluorite was obtained by co-precipitation in aqueous hydrofluoric acid according to the scheme presented in Fig. 1.24. Then, the co-precipitated powder was annealed at 400°C under anhydrous argon atmosphere for 4 hours. It was isostatically pressed before vacuum sintering at 600°C for 1 hour. The final Yb:CaF₂ ceramic was obtained after a hot pressing stage at 900°C and 60 MPa in vacuum, resulting in a satisfying grade of transparency as shown in Fig 1.25.

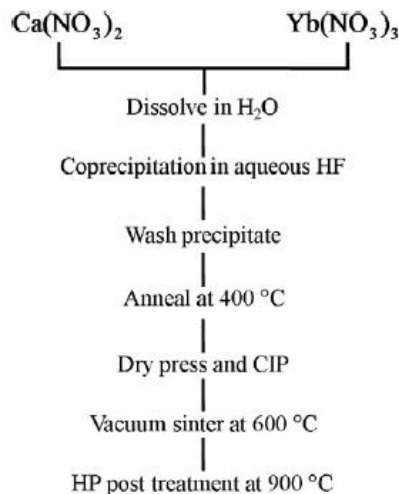


Figure 1.24. Schematic diagram to fabricate Yb:CaF₂ ceramics [Lyberis 2012]

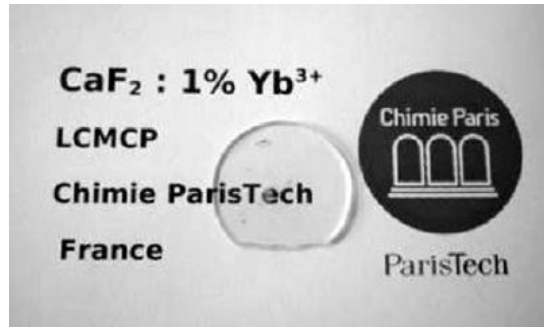


Figure 1.25. Transparent Yb doped CaF₂ ceramic [Lyberis 2012]

1.4.6.2 Lu₃NbO₇

In addition to the cited materials, in 2011 a new composition was proposed by L. An *et al* [An 2011-1]. They investigated the sintering of a Lu₃NbO₇ matrix. The starting materials were commercial Lu₂O₃ (99.99% of purity) and Nb₂O₅ (99.9% of purity). After shaping, the powder mixture was sintered by a SPS apparatus, according to the following cycle: the temperature was increased up to 600°C in 3 minutes, then up to 1000°C in 4 minutes, and they stayed at this temperature during 5 minutes in order to apply a 10 MPa pressure. After this first step, the pressure was increased to 100 MPa in 1 minute. The temperature was raised to 1450°C at 10°C/min (45 minute plateau). After sintering, a post-annealing treatment was performed at 850°C in air for 6 hours. The obtained transparent Lu₃NbO₇ ceramic has a transmittance of 68% at 550 nm (Fig.1.26).

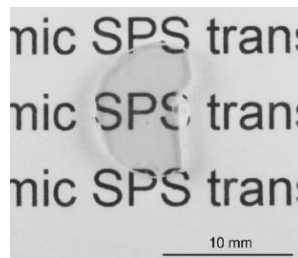


Figure 1.26. Micrograph of a Lu₃NbO₇ ceramic sintered at 1450°C and annealed at 850°C in air [An 2011-1]

The same author [An 2013] investigated the effects of post-annealing temperatures on this material. Post heat treatments were performed at 750°C, 850°C, 950°C, 1050°C, 1150°C, and 1250°C in air during 6 hours. Evolution of transmittance is shown in Fig.1.27.

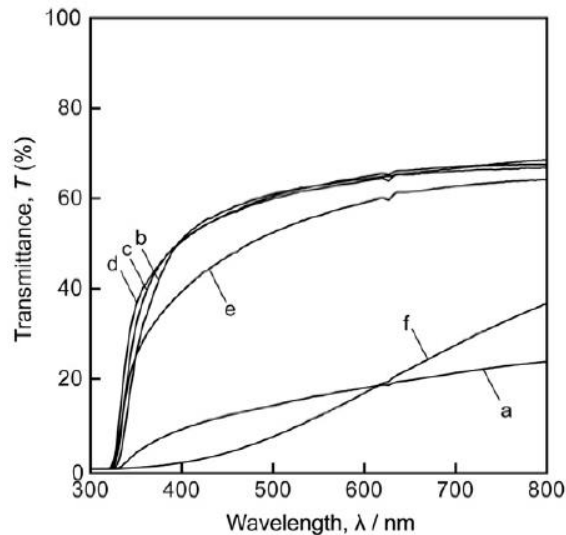


Figure 1.27. Transmittance of Lu_3NbO_7 ceramics sintered by SPS at 1450°C with different post-annealing temperature (a) 750°C , (b) 850°C , (c) 950°C , (d) 1050°C , (e) 1150°C , and (f) 1250°C [An 2013]

The lack of transparency obtained at the lowest and highest sintering temperatures results from a porous structure and grain coarsening. The best results are obtained on 1450°C SPS heat-treated pellets.

No additional papers related to the optical properties of this ceramic material has been published yet.

1.5. Discussion

The majority of published works describes the compositions and their efficiencies for a laser materials laser performance. This includes YAG, spinel, sesquioxides alumina and fluorite materials. The main goal of the research works in this field is to reach equivalent efficiencies in laser performances. However, beyond the choice of original compositions, sintering techniques allow to consider new compositions and multi-compositions in material to improve the heat diffusion. Therefore, even if the optical properties are still lower than that of crystals, the crystalline ceramics appear as promising materials. In addition, the ceramics has a potential to be used as a gain medium for implementation of the optical device.

The subject of this PhD program is to investigate new active media for amplification in the visible and infrared ranges. The rare earth niobate compounds with RE_3NbO_7 (RE: rare earth elements) composition are really promising since they are new compositions having a large

transparency window from visible to infrared ranges. The results described by L. An *et al.* previously demonstrate that this host can be used as transparent ceramics.

We have studied the Y_3NbO_7 host lattice in order to understand the behavior of this material under SPS process and its impact on the optical properties. Moreover, europium luminescence can be an efficient tool to understand the potential structural modification occurring around the rare earth element, when the niobate matrix was doped with europium ions.

The manuscript first list the experimental setup used during this project. It also describes the thermal stability of the selected phase through the emission of europium doped powders. Another aspect of the manuscript is devoted to the powder synthesis and the influence of SPS parameters on densification. In addition, the effects of SPS on the structural and optical properties of optimized doped pellet are discussed. The last part of the manuscript summarizes the different key points identified during this investigation.

References

- [An 2011-1] L. An, A. Ito, T. Goto, Mater. Lett. **65**, (2011) 3167-3169
- [An 2011-2] L. An, A. Ito, T. Goto, Ceram. Int. **37**, (2011) 2263–2267
- [An 2012-1] L. An, A. Ito, T. Goto, J. Eur. Ceram. Soc **32**, (2012) 1035-1040
- [An 2012-2] L. An, A. Ito, T. Goto, J. Eur. Ceram. Soc. **32**, (2012) 3097-3102
- [An 2013] L. An, A. Ito, T. Goto, Ceram. Int. **39**, (2013) 383-387
- [Anderson 1970] R.C. Anderson, US patent n°3 545 987 (1970)
- [Bonnet 2015] L. Bonnet, R. Boulesteix, A. Maitre, C. Salle, V. Couderc, A. Brenier, Opt. Mater. **50**, (2015) 2-10
- [Bonnefont 2012] G. Bonnefont, G. Fantozzi, S. Trombert, L. Bonneau, Ceram. Int. **38**, (2012) 131–140
- [Boulesteix 2013] R. Boulesteix, A. Maitre, L. Chretien, Y. Rabinovitch, C. Salle, J. Am. Ceram. Soc. **96** (6), (2013) 1724-1731.
- [Boulesteix 2014] R. Boulesteix, R. Epherre, S. Noyau, M. Vandenhende, A. Maitre, C. Salle, G. Alombert-Goget, Y. Guyot, A. Brenier, Scr. Mater. **75**, (2014), 54-57
- [Bour 1989] D. P. Bour, G. A Evans, D. B. Gilbert, J. Appl. Phys. **65** (9), (1989) 3340-3343
- [Chang 1963] N.C. Chang, J. Appl. Phys. **34** (12), (1963) 3500-3504
- [Chen 2013] S. Chen, Y. Wu, Am. Ceram. Soc. Bull. **92** (2), (2013) 32-37
- [Chen 2014-1] F. Chen, F. Zhang, J. Wang, H. Zhang, R. Tian, J. Zhang, Z. Zhang, F. Sunb, S. Wang, Scr. Mater. **81**, (2014) 20–23
- [Chen 2014-2] S. Chen, Y. Wu, J. Mater. Res. **29** (19), (2014) 2297-2302
- [Cheng 2010] X.J. Cheng, J.Q. Xu, M.J. Wang, B.X. Jiang, W. X. Zhang, Y.B. Pan, Laser Phys. Lett. **7**, (2010) 351-354
- [Cherepy 2007] N.J. Cherepy, J.D. Kuntz, T.M. Tillotson, D.T. Speaks, S.A. Payne, B.H.T. Chai, Y. Porter-Chapman, S.E. Derenzo, Nucl. Instrum.: Methods Phys. Res. Sect. A **579**, (2007) 38-41

- [Choi 1990]** H.K. Choi, C.A. Wang, Appl. Phys. Lett. **57**, (1990) 321-323
- [Coble 1961]** R. L. Coble, Am. Ceram. Soc. Bull. **38**, (1959) 507-510
- [Cornacchia 2007]** F. Cornacchia, A. Richter, E. Heumann, G. Huber, D. Parisi, M. Tonelli, Opt. Express **15** (3), (2007) 992-1002
- [Cornacchia 2008]** F. Cornacchia, A. Di Lieto, M. Tonelli, A. Richter, E. Heumann, G. Huber, Opt. Express **16** (20), (2008) 15932-15941
- [Dahotre 2008]** N. B. Dahotre, S.P. Harimkar, Fabrication and machining of materials, Springer, Berlin, (2008)
- [Deter 2000]** C. Deter, J. Kraenert, Proc. SPIE 3954, (2000) 175-184
- [Dupont 2004]** A. Dupont, PhD thesis (n°2835) University of Bordeaux (2004)
- [Dutta 1969]** S.K. Dutta, G.E. Gazza, Mat. Res. Bull. **4**, (1969) 791-796
- [Frage 2010]** N. Frage, S. Kalabukhov, N. Sverdlov, V. Ezersky, M. P. Dariel, J. Eur. Ceram. Soc. **30**, (2010) 3331–3337
- [Fu 2013]** P. Fu, W. Lu, W. Lei, Y. Xu, X. Wang, J. Wu, Ceram. Int. **39**, (2013) 2481-2487
- [Goldstein 2009]** A. Goldstein, A. Goldenberg, M. Hefetz, J. Ceram. Soc. Jpn. **117** (11), (2009) 1281-1283
- [Greskovitch 1973]** G. Greskovitch, J.P. Chernoch, J. Appl. Phys. **44**, (1973), 4599-4606
- [Groza 1992]** J.R. Groza, S.H. Risbud, K Yamazaki, J. Mater. Res **7(10)**, (1992) 2643-2645
- [Hering 2004]** P. Hering, J.P. Lay, S. Stry, Laser in environment and life sciences, Springer, Heidelberg, (2004)
- [Hönninger 2005]** C. Hönninger, A. Courjaud, P. Rigail, E. Mottay, M. Delaigue, N. Deguil-Robin, J. Limpert, I. Manek-Honninger, F. Salin, C. Denman, I.T. Sorokina, Trends in optics and photonics; Advanced solid-state photonics, Vienna, (2005) 657-662
- [Hou 2011]** X. Hou, S. Zhou, T. Jia, H. Lin, H. Teng, J. Lumin. **131**, (2011)1953–1958
- [Ikesue 1992]** A. Ikesue, Japanese patent, (1992) 3463941
- [Ikesue 2008]** A. Ikesue, Y. L. Aung, Nat. photonics **2**, (2008) 721-727

- [Innerhofer 2003]** E. Innerhofer, T. Südmeyer, F. Brunner, R. Häring, A. Aschwanden, R. Paschotta, C. Hönninger, M. Kumkar, and U. Keller, *Opt. Lett.* **28** (5), (2003) 367-369
- [Jin 2010]** L. Jin, G. Zhou, S. Shimai, J. Zhang, S. Wang, *J. Eur. Ceram. Soc.* **30** (2010) 2139-2143
- [Kamada 2009]** K. Kamada, T. Yanagida, K. Tsutsumi, Y. Usuki, M. Sato, H. Ogino, *IEEE Trans Nucl Sci.* **56**, (2009) 570-573.
- [Kasprowicz 2011]** D. Kasprowicz, M.G. Brik, A. Majchrowski, E. Michalski, P. Gluchowski, *Opt. Commun.* **284**, (2011) 2895-2899.
- [Killi 2005]** A. Killi, Steinmann, A., Dörring, J., Morgner, U., Lederer, M. J., Kopf, D. Fallnich, C., *Opt. Lett.* **30** (14), (2005) 1891-1893
- [Kim 2009]** B.-N. Kim, Keijiro Hiraga, Koji Morita, Hidehiro Yoshida, *J. Eur. Ceram. Soc.* **29**, (2009) 323-327
- [Klement 2008]** R. Klement, S. Rolc, R. Mikulikova, J. Krestan, *J. Eur. Ceram. Soc.* **28** (5), (2008) 1091-1095
- [Krell 2003]** A. Krell, P. Blank, H. Ma, T. Hutzler, *J. Am. Ceram. Soc.* **86** (1), (2003) 12–18
- [Kuwano 2004]** Y. Kuwano, K. Suda, N. Ishizawa, T. Yamada, *J. Cryst. Growth* **260**, (2004) 159-165.
- [Li 2009]** W. Li, Q. Hao, Q. Yang, H. Zeng, *Laser Phys. Lett.* **6** (8), (2009) 559-562
- [Li 2011]** C. Li, W. Liu, H. Gao, B. Jiang, Y. Wang, H. Kou, Y. Shen, Y. Pan, Y. Bo, Q. Peng, *Appl. Phys. B: Lasers Opt.* **104** (3), (2011) 625-631
- [Li 2016]** W. Li, B. Mei, J. Song, W. Zhu, G. Yi, *J. Alloys Comp.* **660**, (2016) 370-374
- [Limpert 2003]** J. Limpert, T. Clausnitzer, A. Liem, T. Schreiber, H.-J. Fuchs, H. Zellmer, E.-B. Kley, and A. Tünnermann, *Opt. Lett.* **28** (10), (2003) 1984-1986
- [Loesel 1998]** F. H. Loesel, J. P. Fischer, M. H. Gotz, C. Horvath, T. Juhasz, F. Noack, N. Suhm, J.F. Bille, *Appl. Phys. B: lasers and optics* **66**, (1998) 121-128
- [Lu 2002]** J. Lu, K-I Ueda, H. Yagi, T. Yanagitani, Y. Akiyama, A. Alexander. Kaminskii, *J. Alloys Compd.* **341**, (2002) 220-225

- [Lubatchowski 2007]** H. Lubatchowski, *Lasers in medicine: laser tissue interaction and applications*, Wiley, (2007)
- [Lyberis 2012]** A. Lyberis, A. J. Stevenson, A. Sukanuma, S. Ricaud, F. Druon, F. Herbst, D. Vivien, P. Gredin, M. Mortier, *Opt. Mater.* **34**, (2012) 965–968
- [Maiman 1960]** T.H. Maiman, *Nature* **187**, (1960) 494
- [Morita 2015]** K. Morita, B-N. Kim, H. Yoshida, K. Hiraga, Y. Sakka, *Acta Materialia* **84**, (2015) 9-19
- [Mouzon 2009]** J. Mouzon, A. Maître, L. Frisk, N. Lehto, M. Odén, *J. Eur. Ceram. Soc.* **29** (2), (2009) 311-316
- [Nolte 1997]** S. Nolte, C. Momma, H. Jacobs, A. Tünnermann, B. N. Chichkov, B. Wellegehausen, H. Welling, *J. Opt. Soc. Am. B* **14** (10), (1997) 2716-2722
- [Peuchert 2009]** U. Peuchert, Y. Okano, Y. Menke, S. Reichel, A. Ikesue, *J. Eur. Ceram. Soc.* **29**, (2009) 283–291
- [Podowitz 2010]** S. R. Podowitz, R. Gaumé, R. S. Feigelson, *J. Am. Ceram. Soc.* **93** (1) (2010) 82-88
- [Rabinovitch 2008]** Y. Rabinovitch, C. Bogicevic, F. Karolak, D. Tetard, H. Dammak, *J. mater. Process. Technol.* **199**, (2008) 314-320
- [Richter 1963]** A. Richter, E. Heumann, G. Huber, V. Ostroumov, W. Seelert, *Opt. Express* **15** (8), (2007) 5172-5178
- [Sanghera 2011]** J. Sanghera, S. Bayya, G. Villalobos, W. Kim, J. Frantz, B. Shaw, B. Sadowski, R. Miklos, C. Baker, M. Hunt, I. Aggarwal, F. Kung, D. Reicher, S. Peplinski, A. Ogloza, P. Langston, C. Lamar, P. Varmette, M. Dubinskiy, L. DeSandre, *Opt. Mater.* **33**, (2011) 511–518
- [Seeley 2011]** Z.M. Seeley, J.D. Kuntz, N.J. Cherepy, S.A. Payne, *Opt. Mater.* **33**, (2011) 1721–1726
- [Sorokin 2007]** E. Sorokin, I.T. Sorokina, J. Mandon, G. Guelachvili, N. picqué, *Opt. Express* **15** (25), (2007) 16540-16545

[Stoeppler 2012] G. Stoeppler M. Schellhorn, M. Eichhorn, Laser Phys. **22** (6), (2012) 1095-1098

[Takaichi 2007] K. Takaichi, H. Yagi, P Becker, A Shirakawa, K Ueda, L Bohatý, T Yanagitani and A A Kaminskii, Laser Phys. Lett. **4** (7), (2007) 507-510

[Wang 2009] C. Wang, Z. Zhao, Scr. Mater. **61**, (2009) 193–196

[Wang 2014] L. Wang, C. Gao, M. Gao, Y. Li, F. Yue, J. Zhang, D. Tang, Opt. Express **22** (1), (2014) 254-261

[Wechsler 2000] B. A. Wechsler, D. S. Sumida, Laser crystals handbook of laser science and technology, suppl. 2: Opt. Mater., CRC Press, Boca Raton, FL, (2000), p 595

[Xu 2013] J. Xu, Y. Shi, J. Xie, F. Lei, J. Am. Ceram. Soc. **96** (6), (2013) 1930–1936

[Yang 2012] H. Yang, J. Zhang, X. Qin, D. Luo, J. Ma, D. Tang, H. Chen, D. Shen, Q. Zhang, J. Am. Ceram. Soc. **95**, (2012) 52-55

[Yang 2014] H. Yang, L. Zhang, D. Luo, X. Qiao, J. Zhang, T. Zhao, D. Shen, D. Tang, Opt. Mater. Express 215076 **5** (1), (2014) 142-148

[Zhang 2004] J. Zhang, S. W. Wang, T. J. Rong, L. D. Chen, J. Am. Ceram. Soc. **87**, (6), (2004) 1072–1075

[Zhou 2003] Y. Zhou, K. Hirao, Y. Yamauchi, S. Kanzaki, Scr. Mater. **46**, (2003) 1631-1636

Chapter 2

Experimental results and discussion

2.1 Synthesis and characterization of Eu³⁺ doped Y₃NbO₇ powder

Investigation partially published in Journal of Solid State Chemistry, 235 (2016) 169-174

2.1.1 Introduction

Rare earth niobate compounds of formula RE₃NbO₇ (RE: rare earth elements [Rooksby 1964][Tilloca 1970][Tilloca 1972][Allpress 1979][Rossell 1979][Subramanian 1983][Barker 1984][Kahn-Harari 1995][Siqueira 2014]) have attracted considerable attention as they can present interesting magnetic [Vent 1994][Doi 2009][Wakeshima 2010], dielectric [Cai 2007] [Cai 2010], photocatalytic [Abe 2006][Zhao 2015], electric or ionic conductivity properties [Yamamura 1999][Marrocchelli 2009][Norberg 2009]. Holmium and erbium luminescent properties were also reported [Krylov 1971][Walasek 2007-1][Walasek 2007-2]. Depending on the rare earth element ionic radius size, these niobate materials crystallize in the orthorhombic (weberite), cubic (pyrochlore) or cubic fluorine type structure for the smallest cations. So, cubic zirconia was used to prepare nanocrystalline solid solution with Y_{3-x}Eu_xNbO₇ which allowed obtaining europium luminescence [Hirano 2013]. Recently, L. An et al [An 2011][An 2013] reported the possibility to prepare Lu₃NbO₇ transparent ceramics using a SPS sintering process. Such work enlarges the range of applications of these niobates to massive optical materials.

Considering the transparency of niobate matrices in the visible and infrared range and the high interest of doping an isotropic cubic RE₃NbO₇ phase for optical properties, we have studied Eu³⁺ doped Y₃NbO₇ phase. The Y₃NbO₇ compound presents a domain of existence corresponding to a Nb/[Y+Nb] cationic ratio ranging between 20 % to 31.5 %. This compound

is supposed to be stable at high temperatures, up to its peritectic decomposition that is reported at 1950°C [Bondar 1969][Babich 1989]. However, due to the capability of the fluorine structure to accept cationic disorder and oxygen vacancies, a detailed characterization of this phase is required to understand its luminescence properties. Such work is presented in the present investigation as a function of the thermal treatment of the initial raw powder.

2.1.2 Experimental results and discussion

2.1.2.1 Synthesis

The powder synthesis is one of the most crucial stages in the manufacturing process of ceramics. The purity of the powder, the grain size and the morphology will impact strongly the densification of the pellet. Scanning electron microscopy was performed to characterize the powders. The equipment used was a TESCAN Vega II SBH SEM.

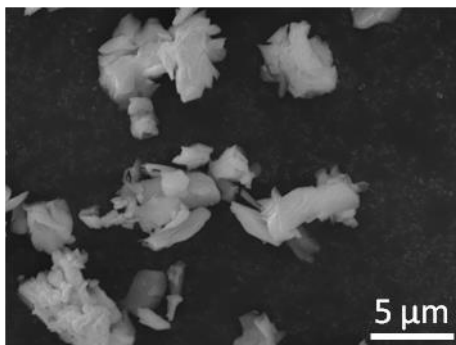
We have tested several synthesis routes to obtain a pure Eu^{3+} doped Y_3NbO_7 phase.

2.1.2.1.1 Solid state route

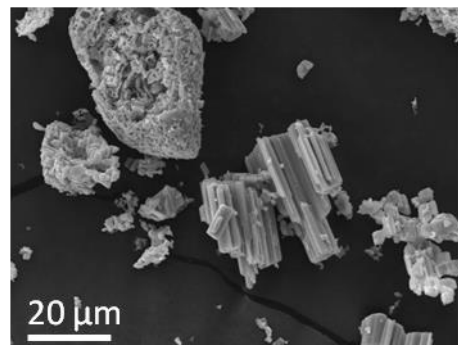
The synthesis of Eu^{3+} doped Y_3NbO_7 niobate phase was first conducted using a classical solid state route, starting from Nb_2O_5 , Y_2O_3 and Eu_2O_3 oxide powders (99.99% purity). The morphology and the grain sizes of initial powders are presented in Fig. 2.1. One can notice quite different grain shapes and sizes according to the chemical nature of the powders. Moreover, these powders look quite agglomerated. A two-step ball milling stage (30 min dry + 30 min with ethanol) was performed to homogenize the powder mixture and reduce the agglomerate sizes and the overall size distribution. Fig. 2.2 shows the powder mixture after grinding. A homogenization of the grain sizes is observed.

Then, this mixture was heat treated at 1200°C, 1300°C, 1400°C for a maximum of 10 hours under air, in order to form the niobate compound, before the sintering process.

(a) Y_2O_3



(b) Nb_2O_5



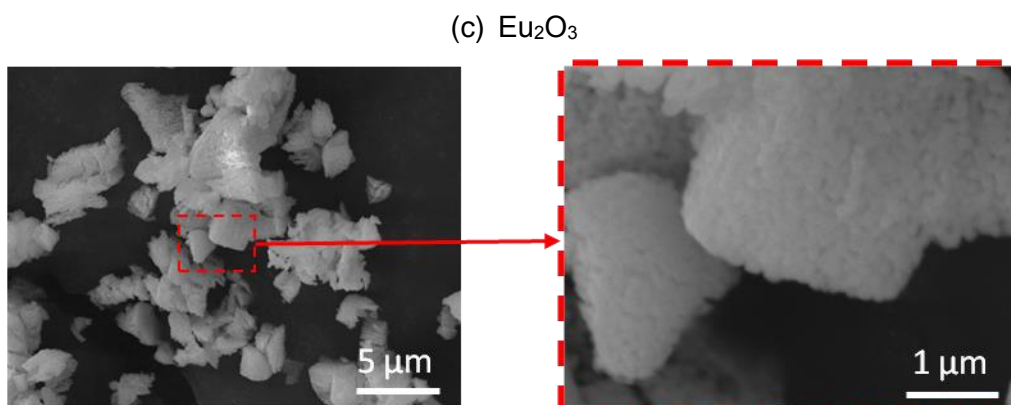


Figure 2.1: SEM micrographs of the initial oxide powders: (a) Y_2O_3 , (b) Nb_2O_5 and (c) Eu_2O_3 .

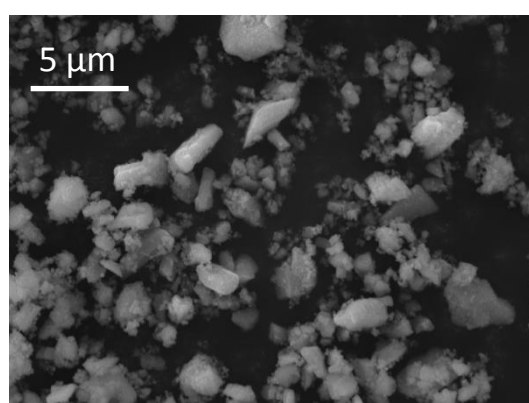


Figure 2.2: SEM micrograph of initial oxide powders after ball milling.

2.1.2.1.2 Self-combustion

The Glycine Nitrate Process was used to synthesize Eu^{3+} doped Y_3NbO_7 compound by self-combustion. Glycine/nitrate ratio was fixed at 0.555 (in mol) and starting materials used were $\text{Y}(\text{NO}_3)_3 \cdot 6\text{H}_2\text{O}$, $\text{Eu}(\text{NO}_3)_3 \cdot 6\text{H}_2\text{O}$, $\text{Nb}(\text{NO}_3)_5$, Glycine (99% purity). All the reactants were dissolved with stoichiometry proportion in 10 ml of stirred water. The solution was heated under a Meker flame. The aspect of the liquid phase changed and it turned into a gel. The reaction occurred (explosion) when the temperature reached 250°C – 300°C . A brown powder is finally recovered and a post-heat-treatment at 800°C during 10 hours under oxygen was necessary to eliminate the organic traces and to obtain a white powder.

2.1.2.1.3 Mineral Sol-gel (Pechini) route

A low temperature synthesis of Y_3NbO_7 compound based on a polymerizable complex method was proposed by T. Okubo *et al* [Okubo 1997]. We have substituted the carbonate rare earth precursors by nitrate precursors and slightly modified the experimental procedure as presented below. The purity of the starting materials was 99.99% for the oxides RE_2O_3

RE=lanthanides, 99.998% for NdCl_5 , >99% for ethylene glycol, 99.5% for citric acid and >99.9% for methanol.

Stoichiometric amounts of rare earth oxides were dissolved in concentrated nitric acid (11.76 mol.L^{-1}) in order to obtain a homogeneous distribution of the cation. Then the solutions were evaporated to dryness. Methanol was used to dissolve NbCl_5 . A large excess of citric acid relative to niobium cation ($\times 100$) was added into the solution. After dissolution of the citric acid, crushed powder of rare earth nitrates was poured into the reactive medium. A continuous stirring was applied. Finally, the ethylene glycol ($\times 4$) was added to the solution. The solution was stirred continuously and heated at 140°C to accelerate the esterification reaction. The temperature was maintained until the formation of a brown resin. This residue was burned under a Meeker flame until obtaining a totally white powder.

As the stability of the niobate compound is announced between 20% and 31.5% (Nb/RE ratio), we fixed the final reactant proportion at 23% and 25% to obtain the $\text{Y}_{2.85}\text{Eu}_{0.15}\text{Nb}_{0.9}\text{O}_{6.75}$ and the $\text{Y}_{2.85}\text{Eu}_{0.15}\text{NbO}_7$ compositions, respectively.

Concerning the investigation of the thermal stability, after a 6 hours heat treatment at 700°C under O_2 atmosphere, 1 hour successive heat-treatments were performed each 50 degree from 700°C to 1650°C .

Eu-doped YNbO_4 was prepared through an equivalent synthetic route by changing the proportion of rare earth and niobium reactants.

The purity of all final products was controlled after each step by X-ray diffraction.

2.1.2.1.4 Comparison of powders issued from the 3 syntheses

Fig. 2.3 shows the different powder morphologies obtained according to the syntheses routes. The powder prepared by solid state route (a) present irregular morphology of the grains and large aggregates whereas the powder obtained by Pechini synthesis shows nanometric and homogeneous shape grains (c). The self-combustion method also gives nanometric grains but quite agglomerated (b)

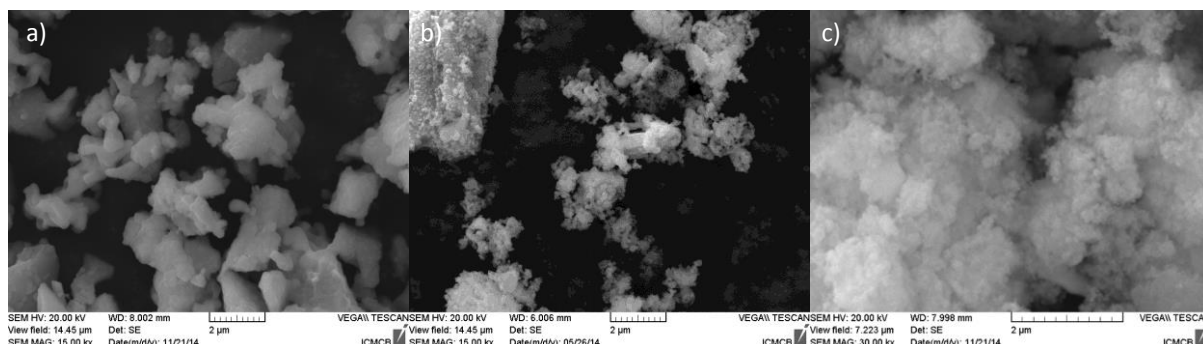


Figure 2.3: SEM pictures of powders synthesized by (a) solid state reaction ($T = 1300^\circ\text{C}$), (b) self-combustion (800°C) and (c) sol-gel route (700°C).

2.1.2.2 X-Ray diffraction analyses

Room temperature powder X-ray diffraction patterns were collected on a PANalytical X'pert PRO MPD using a Bragg-Brentano θ - 2θ geometry and equipped with a Ge (111) monochromator to obtain a monochromatic Cu K α 1 ($\lambda = 1.54059 \text{ \AA}$). The europium/yttrium niobate matrix diffractogram was refined using the Rietveld method with the conventional reliability factors. The Fullprof program package was used [Rodriguez 2001]. The unit cell parameters, atomic positions and Debye-Waller factors were refined on the basis of the Fm-3m space group corresponding to the fluorite type structure.

The XRD pattern associated to the $Y_{2.85}Eu_{0.15}NbO_7$ composition, prepared from the solid state route, is presented in Fig. 2.4. Y_3NbO_7 niobate phase is the main phase present in the calcined powder ($T = 1300^\circ\text{C}$). It corresponds in fact to the $Y_{2.85}Eu_{0.15}NbO_7$ phase since the substitution of Y^{3+} by Eu^{3+} is expected in the final structure. However, Y_2O_3 and $YNbO_4$ are also present. It can be explained taking into account the Y_2O_3 - Nb_2O_5 equilibrium diagram (fig.2.5). It shows the presence of another compound in this system, i.e. $YNbO_4$. During solid state reaction, local heterogeneities within the ball milled powder could induce the formation of $YNbO_4$ from Y_2O_3 and Nb_2O_5 and therefore it gave rise to some residual Y_2O_3 .

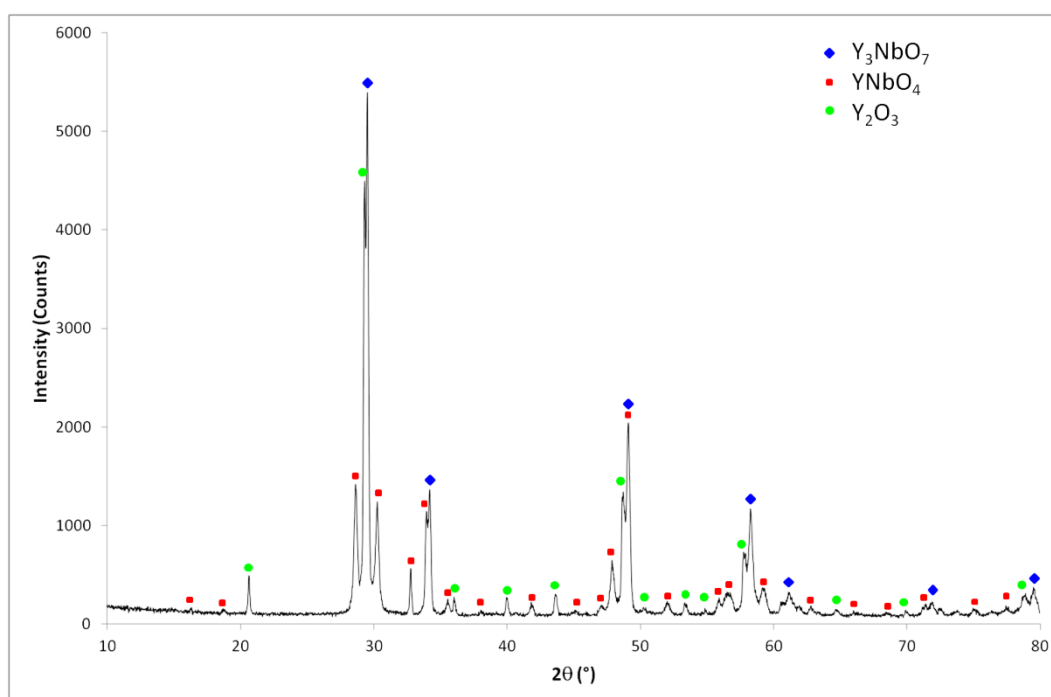


Figure 2.4: X-ray diffraction pattern of the powder calcined at $T = 1300^\circ\text{C}$ during 10 h. under air.

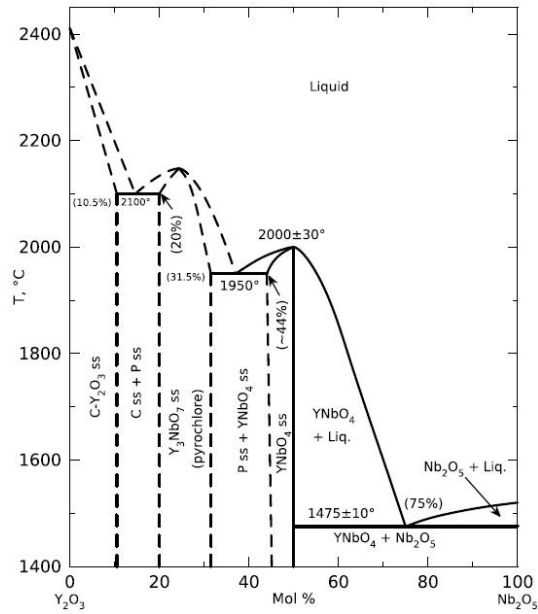


Figure 2.5: Y_2O_3 - Nb_2O_5 equilibrium phase diagram [Kakahana 1996].

To improve the synthesis, successive heat-treatments were performed at 1200°C, 1300°C, 1400°C in air. But they were not sufficient to remove totally traces of impurities. $YNbO_4$ and Y_2O_3 oxides are clearly detected on the diffractograms (Fig. 2.6).

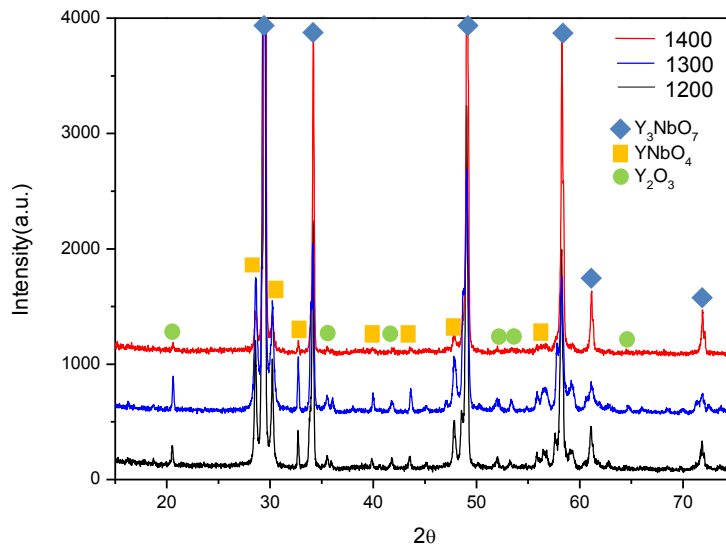


Figure 2.6: Evolution of X-Ray patterns of powders obtained through solid state reaction.

The different heat treatments improve the powder purity but it results in a natural growth of the crystallites. Therefore, it also contributes to a decrease of the sinterability of the powder, which will avoid a high densification of the material.

Results obtained by using self-combustion method based on the glycine nitrate route are illustrated below (Fig. 2.7). Unfortunately, the only phases obtained through this synthesis were Y_2O_3 and Nb_2O_5 .

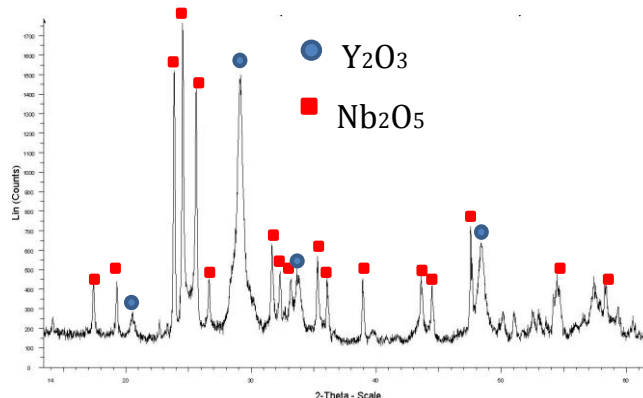


Figure 2.7: X-Ray pattern of powders obtained through self-combustion reaction.

As the first results were not satisfying, the self-combustion synthesis method was definitely abandoned given the absence of formation of the desired niobate.

Finally, the Pechini synthesis seems to be the best method to prepare Eu^{3+} doped Y_3NbO_7 powder. XRD analysis of the resulting powder obtained after a $700^\circ C$ heat treatment (Fig. 2.8) only shows the presence of the $Y_{2.85}Eu_{0.15}NbO_7$ phase. One can notice the line broadening, characteristic of the presence of small size crystallites usually obtained from a sol-gel process. Calculation from the Scherrer's equation gives an average crystallite size of 9 nm [Scherrer 1918].

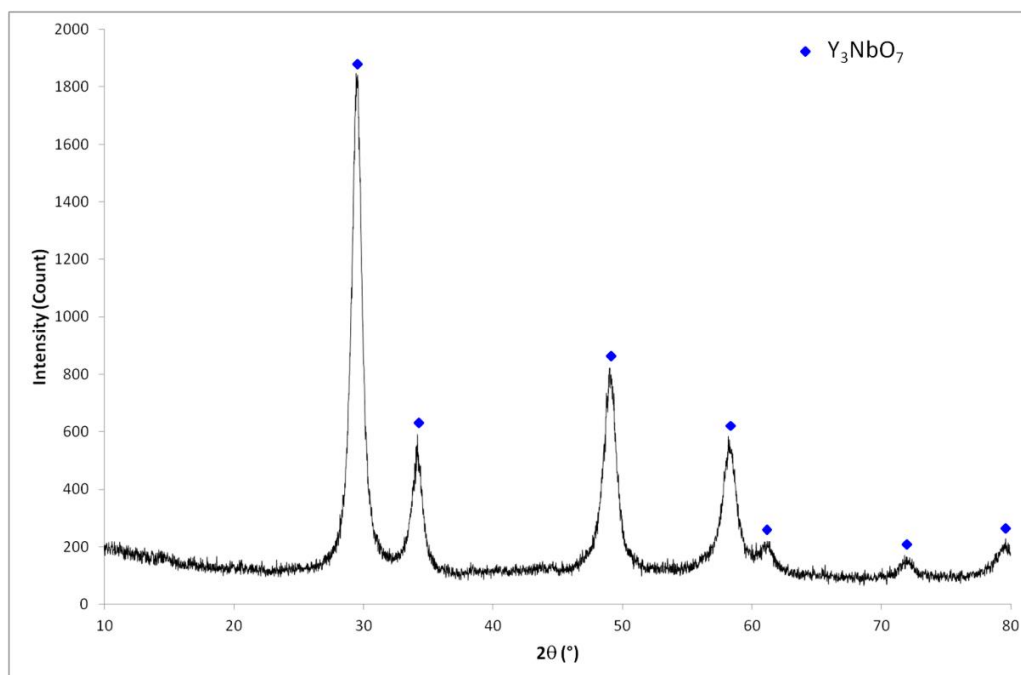


Figure 2.8: X-ray diffraction pattern of a sol-gel powder heat treated at $700^\circ C$ under O_2 .

However, one drawback of this mineral sol-gel route is the presence of a high proportion of residual carbon within the powder as a consequence of the use of organic reactants. Prior to sintering, powders have been treated at different temperatures under oxygen atmosphere in order to test the stability of the phase as a function of the temperature and the time of the treatment. Results obtained at 500°C, 700°C during 2 hours are illustrated in Fig. 2.9.

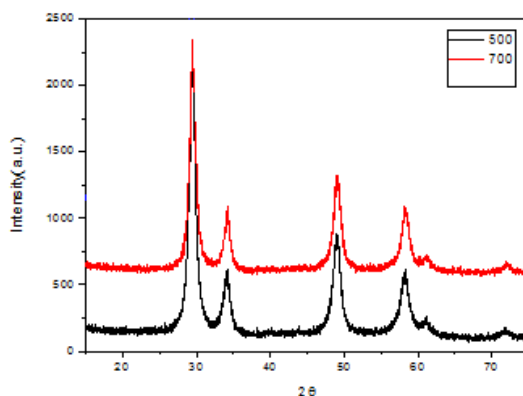


Figure 2.9: X-Ray patterns of the sol-gel synthesized powder as function of the temperature (duration time of heat-treatment equal to 2 hours).

Because no trace of impurities or significant change in the full width at half maximum of the diffraction peaks was detected between 500°C and 700°C, the condition fixed to eliminate the carbon impurities and to preserve the purity of the initial powders was a heat-treatment at 700°C during 2 hours.

2.1.2.3 Structural characterization- Effect of temperature

The effect of temperature was studied with to evaluate the thermal stability of Y_3NbO_7 powder obtained through Pechini synthesis route.

Fig. 2.10 shows the evolution of X-ray diffraction patterns obtained at room temperature after each thermal treatment. A clear decrease of the full width at half maximum of each peak is visible when temperature increases according to the improvement of the crystallization state. Crystallite average sizes were calculated using the Scherrer formula for the lowest heat-treatment [Scherrer 1918][Patterson 1939].

$$D = \frac{0.89\lambda}{\beta \cos\theta}$$

With, λ being the wavelength of the Cu K_α radiation (1.54 Å), β the full width at half maximum of the peak and θ the Bragg's angle obtained from 2θ value corresponding to the maximum intensity peak in XRD pattern. Calculation were performed using a spherical shape of the particles.

A 60 nm dimension is obtained for the 700°C heat treatment; it increases up to 75 nm at 900°C.

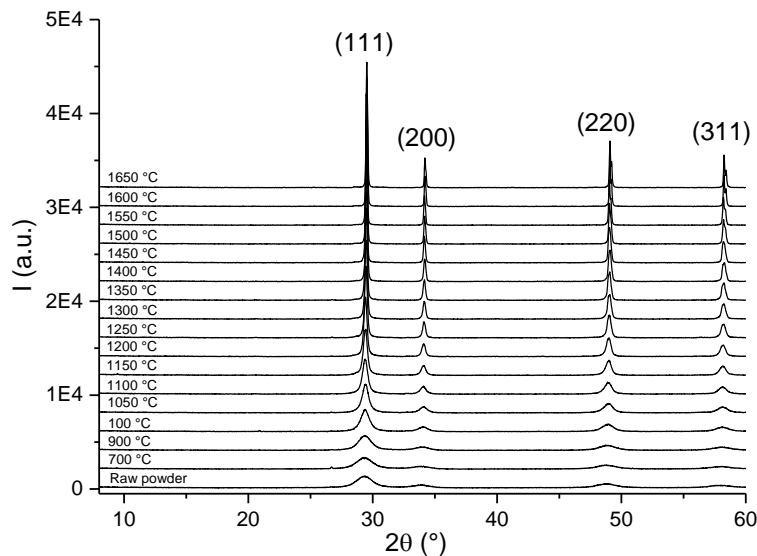


Figure 2.10: X-ray patterns of $Y_{2.85}Eu_{0.15}Nb_{0.9}O_{6.75}$

X-Ray diffraction patterns are all consistent with the fluorine cubic type structure (JPDS N° 01-074-6421). However, Raman spectra (Raman acquisition were performed on a thermoscientific DXR raman microscope operating with a 632 nm laser source) presented on Fig. 2.11 shows vibrations which are not compatible with the $Fm\bar{3}m$ symmetry group. This figure illustrates the Raman shift observed on the samples heat-treated at 900°C and 1100°C.

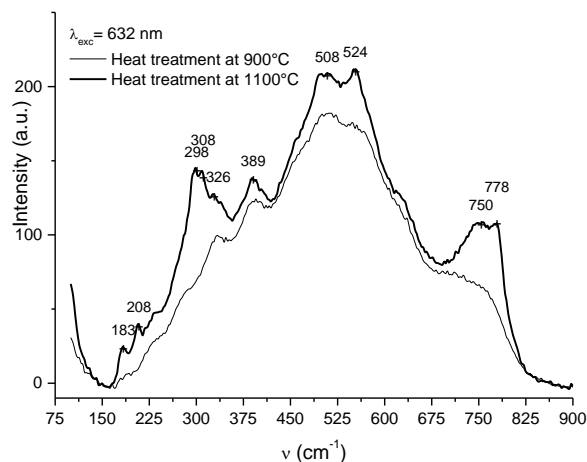


Figure 2.11: Raman shift of $Y_{2.85}Eu_{0.15}Nb_{0.9}O_{6.75}$ heat treated up to 900°C and 1100°C.

An increase of the temperature allows a better discrimination of the vibrations observed, although it remains quite complicated to analyze Raman scattering results when a high number of predicted bands is expected. Raman spectroscopy reported by Kovyazina *et al* [Kovyazina 2003] showed six active modes characteristic of a pyrochlore structure for the yttrium niobate compound. The authors conclude to the existence of a local ordering of the vacancies leading to domains which sizes are lower than the sensitivity of the X-Ray analysis. Same local ordering was also proposed by L. Cai *et al* [Cai 2007] for the Dy, Er and Yb compound. For the Sm, Eu and Gd niobate phases, a mode peaking at 389 cm^{-1} was attributed, for instance, to the signature of the orthorhombic C cmm structure [Siquiera 2014]. The group of lines observed on Fig. 2.11 in the 150 cm^{-1} to 450 cm^{-1} range and around 750 cm^{-1} are similar to the vibrations reported by Kovyazina *et al* [Kovyazina 2003]. Another large band, centered at 510 cm^{-1} , can be attributed to an electron-phonon coupling. Indeed, the energy difference between the maximum of the electric dipole transition at 612 nm and the laser excitation wavelength being equal to this value (luminescence characterization is provided below). As no additional peak can be distinguished whatever the temperature of heat treatment, we indexed, at this stage, the X-Ray diffraction patterns using the F m-3m space group of a fluorine defect type unit cell.

The evolution of grain morphology as a function of the heat treatment is proposed in Fig. 2.12. The powder obtained after synthesis and calcination with the Meker flame (name as raw powder in the following) is made of an agglomeration of grains whose sizes are in the nanometric range, in agreement with the evolution observed on X-ray diffraction measurements. After several heat treatments, sintering of the powders is observed, with a clear grain growth, giving rise to micron size particles at 1600°C .

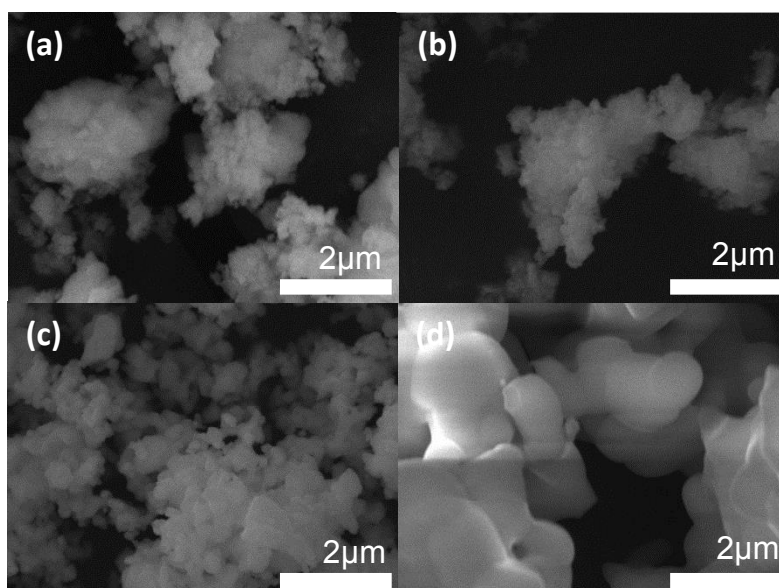


Figure 2.12: SEM micrographs of $\text{Y}_{2.85}\text{Eu}_{0.15}\text{Nb}_{0.9}\text{O}_{6.75}$ as a function of the temperature. (a) Raw powder, powder heat treated (b) at 1000°C , (c) at 1350°C and (d) at 1600°C .

2.1.2.4. Luminescence characterization- Effect of temperature

The photoluminescence properties were analyzed using a Horiba Fluorolog3 spectrofluorimeter. The excitation spectra were corrected for the variation of the incident flux, and the emission spectra were corrected for the transmission of the monochromator and the response of the photomultiplier. The equipment used consisted of a 450 W xenon lamp, an excitation double monochromator, an emission double monochromator and a thermoelectrically cooled photomultiplier tube.

The room temperature luminescence of the raw powder is compared to that of the potential impurities which can be encountered in the Y_2O_3 - Nb_2O_3 system *i.e.* Eu-doped $YNbO_4$ and Eu-doped Y_2O_3 . Results are shown in Fig. 2.13.

Whatever the composition, emission maxima are due to the hypersensitive 5D_0 - 7F_2 electric dipole transition. The emission of $Y_3Nb_{0.9}O_{6.75}:Eu^{3+}$ is quite large compared to that of $YNbO_4:Eu^{3+}$ and $Y_2O_3:Eu^{3+}$. Surprisingly, it is similar to the europium ions response expected in a glass material in which the environment of the rare earth element is not well defined [Tarafder 2011][Kozhevnikova 2015][Kaewkhao 2015]. Conversely, the two other compounds present well-structured emission lines peaking at 611.5 nm for the europium doped sesquioxide and at 612.5 nm, 613.5 nm and 615 nm for $YNbO_4:Eu^{3+}$. The spectral distribution of $Y_2O_3:Eu^{3+}$ is due to the location of the rare earth element in S_6 and C_2 crystallographic sites (six oxygen atoms located at the corners of a cube) [Forest 1969]. The luminescence of $YNbO_4:Eu^{3+}$ differs from the literature. Hirano et al. and Lj.R. Đačanin et al. recently described the emission of this europium doped niobate synthesized through hydrothermal and solid state routes respectively [Hirano 2014][Đačanin 2014]. In both cases, the monoclinic fergusonite β crystal structure was obtained (JCPDS 72-2077) [Trunov 1981]. It presents a maximum as a unique line at 613 nm. After X-ray analysis, the monoclinic fergusonite β and the tetragonal scheelite allotropic forms (JCPDS 00-038-0187) [Amaguchki 1985] of $YNbO_4$ were stabilized by the sol-gel route optimized in the present investigation. Coexistence of the two varieties was observed for lower temperature by K. Jurkschat *et al.* who studied phase transformation of the niobate [Jurkschat 2004]. As the distorted eightfold coordination polyhedra of the rare earth element and their connection with niobate anionic group differ in both unit cells, a modification is expected in the Stark component splitting of the electric dipole transitions. Then fig. 2.13 b (blue curve) illustrates the response of all europium ions in both type of environments.

The excitation spectra are constituted by large UV absorption bands. For the highest energies, the band is due to the electron charge transfer from the oxygen ligand to the rare earth element. Moreover, one can expect to detect at lower energy, between 270 and 300 nm, the O^{2-} - Nb^{5+} charge transfer band (CTB) due to energy transfer towards europium cations. Considering $Y_3Nb_{0.9}O_{6.75}:Eu^{3+}$ compound, the CTB which maximum points at 290 nm, is

strongly shifted to the lowest energies compared to the sesquioxide and the other niobate compounds. The direct consequence is a configurational quenching of the emission. Because of its low energy, main part of the electrons promoted to the CTB under excitation can relax non radiatively through the vibrational levels of the 7F_J fundamental manifold. The global emission is weaker than the one expected even if it is easily detectable and the forbidden 4f-4f absorption lines intensity appears nearly as intense as the CTB on the normalized excitation graph. This relative intensity can also be enhanced by nanometric sizes of the observed particles, which favors multi-reflection phenomenon and absorption between the irradiated particles. The real contribution of the 4f-4f absorption lines to the global absorption can be observed on the diffuse reflectance spectrum superimposed on Fig. 2.13 a.

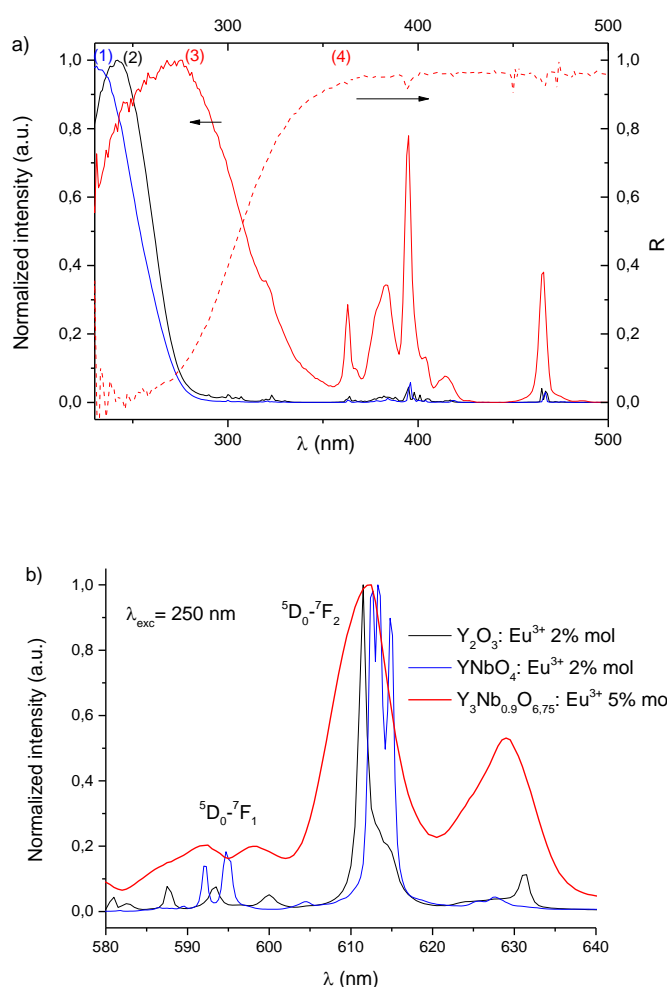


Figure 2.13. Luminescence spectra of europium doped compounds of the $Y_2O_3-Nb_2O_5$ binary composition (room temperature).

a) Normalized excitation spectra of $YNbO_4:Eu^{3+}$ 2%mol ($\lambda_{em}=613.5$ nm) (blue line 1), $Y_2O_3:Eu^{3+}$ 2%mol ($\lambda_{em}=611.5$ nm) (black line 2), $Y_3Nb_{0.9}O_{6.75}:Eu^{3+}$ 5%mol ($\lambda_{em}=597$ nm) (red line 3) at the maximum of the charge transfer band and diffuse reflectance spectra of $Y_3Nb_{0.9}O_{6.75}:Eu^{3+}$ 5%mol (dotted line 4)
b) Normalized emission spectra of $YNbO_4:Eu^{3+}$ 2%mol (blue line 1), $Y_2O_3:Eu^{3+}$ 2%mol (black line 2) and $Y_3Nb_{0.9}O_{6.75}:Eu^{3+}$ 5%mol (red line) excited at 250 nm.

Considering the absorption zones, a 290 nm excitation beam seems to be quite selective to detect $Y_3Nb_{0.9}O_{6.75}:Eu^{3+}$ whereas a 250 nm excitation wavelength will favor the other compounds.

The evolution of the emission spectra as function of the heat-treatment is shown in Fig. 2.14.

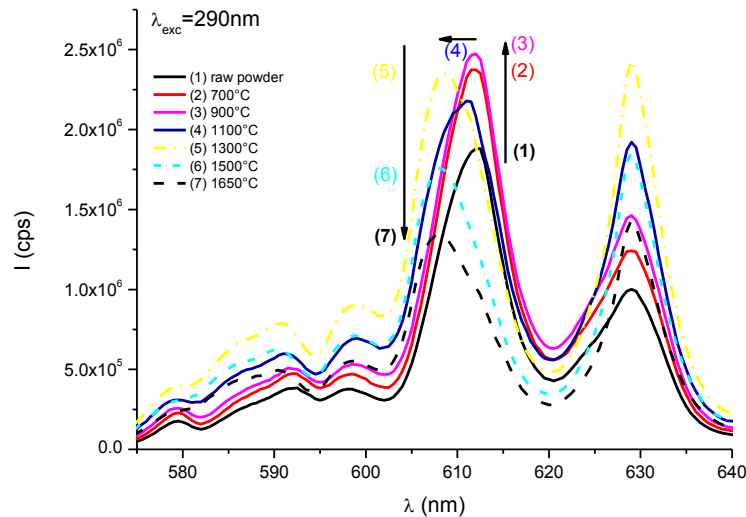


Figure 2.14: Room emission spectra of $Y_3Nb_{0.9}O_{6.75}:Eu^{3+}$ 5% mol under a 290 nm excitation beam as a function of the heat treatment.

The different heat-treatments do not change the full width at half maximum of the emission lines but a shift of the maximum can be noted. From the raw powder spectral distribution, the emission intensity of $Y_3Nb_{0.9}O_{6.75}:Eu^{3+}$ increases up to the 900°C treatment (curve (1)→(3)). From this temperature, it tends to decrease ($T=1100^\circ\text{C}$, curve (4)) and it is then shifted to higher energy. After this spectral modification, a higher intensity level is recovered at 1300°C, before a new decrease for heat-treatments superior to 1300°C. A gradual loss of intensity is then observed for the latest treatments. For the first spectra, the improvement of the crystallization rate results in a higher efficiency of the compounds. The decrease and shift of the maxima from 612 nm to 610 nm observed latter reflects in a first step a re-organization and a change in the local environment of the rare earth element. The loss of efficiency is quite surprising and deserve a deeper characterization of the powder. Fig. 2.15 shows a zoom of the $^5D_0-^7F_2$ electric dipole transitions obtained under an excitation at 250 nm. This wavelength, as illustrated in Fig. 2.13 a, favors the absorption of $YNbO_4/Y_2O_3$ compounds versus that of $Y_3Nb_{0.9}O_{6.75}:Eu^{3+}$.

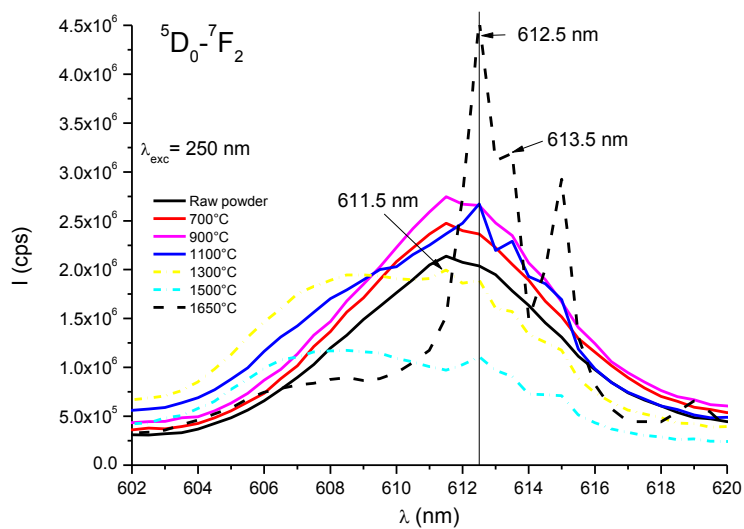


Figure 2.15: Room emission spectra of $Y_3Nb_{0.9}O_{6.75}:Eu^{3+}$ 5% mol under a 250 nm excitation beam as a function of the heat treatment.

As previously, the spectral distribution of europium ions is strongly modified by the heat treatment. The intensity of the maximum increase up to the 900°C thermal treatment. From this temperature, additional small peaks can be distinguished at 612.5 nm, 613.5 nm and 615 nm, which matches perfectly with the location of $YNbO_4:Eu^{3+}$ emission lines. The global intensity decreases up to 1500°C. At 1600°C, the new contribution becomes predominant over the spectral response peaking at 610 nm which matches with the $Y_3Nb_{0.9}O_{6.75}:Eu^{3+}$ emission. One can deduce from these observations, that as the temperature of the applied thermal treatments increases above 900°C, a decomposition of the studied phase is occurring as well as the stabilization of $YNbO_4:Eu^{3+}$. The formation of a richer Nb/Y ratio phase implies a modification of the initial $Y_3Nb_{0.9}O_{6.75}:Eu^{3+}$ composition.

Selective excitation graphs made possible the identification of specific 4f lines (Fig. 2.16). By consequence, additional excitation was performed at 468 nm, in the 4f-4f absorption line of $Y_2O_3:Eu^{3+}$ (Fig. 2.17).

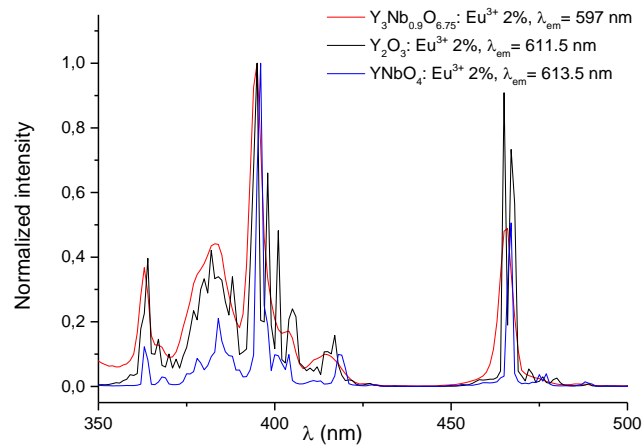


Figure 2.16: Excitation spectra normalized at the maximum of the 4f-4f absorption lines.

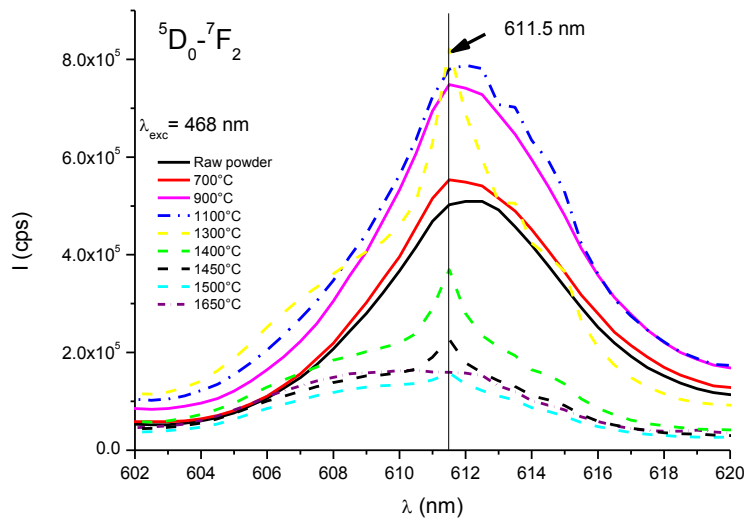


Figure 2.17: Room emission spectra of $\text{Y}_3\text{Nb}_{0.9}\text{O}_{6.75}:\text{Eu}^{3+}$ 5% mol under a 468 nm excitation beam as a function of the heat treatment.

The fingerprint of the $\text{Y}_2\text{O}_3:\text{Eu}^{3+}$ is detected at 1100°C. The corresponding thin line at 611.5 nm is clearly visible on the 1300°C spectrum. However it tends to decrease and totally disappear on the 1650°C spectrum in parallel to the shift of the $\text{Y}_3\text{Nb}_{0.9}\text{O}_{6.75}:\text{Eu}^{3+}$ response. Considering this spectral behavior, it can be said that the thermal treatment of the $\text{Y}_3\text{Nb}_{0.9}\text{O}_{6.75}:\text{Eu}^{3+}$ powder leads first to an improvement of its crystallinity and second to the beginning of its decomposition in $\text{Y}_2\text{O}_3:\text{Eu}^{3+}$ and $\text{YNbO}_4:\text{Eu}^{3+}$. Then, if the europium doped fergusonite niobate is definitely stabilized, the niobate solid solution and the sesquioxide should react giving rise to a new solid solution composition for which the Nb cationic ratio is lower than the initial 23% rate. In parallel, an increase of the oxygen vacancies is expected.

The evolution of the oxygen vacancies as function of the Nb/(Nb+Y+Eu) ratio is reported in fig.2.18 and fig.2.19. Consequently, the slight shift of the luminescence may be explained by a reorganization of the cation environments.

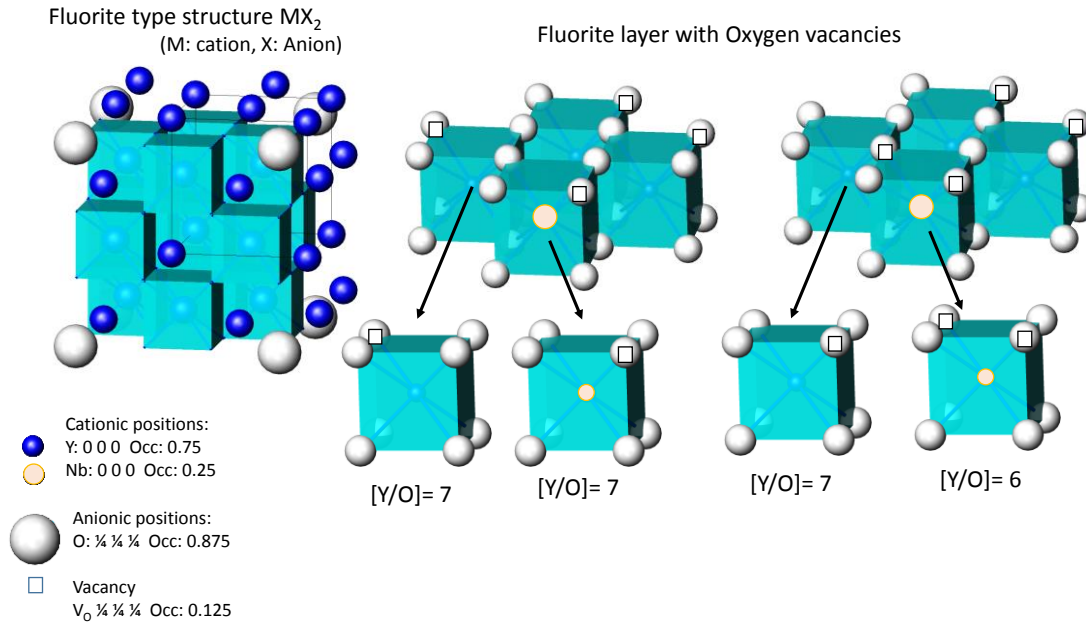


Figure 2.18: Impact of oxygen vacancies on the cationic polyhedra of the fluorite structure

The initial Nb/(Y+Nb) ratio was fixed at 23% ($Y_3Nb_{0.9}\square_{0.1}O_{6.75}\square_{0.25}$). The decomposition of this phase towards $YNbO_4$ has to be associated to the formation of the $Y_3Nb_{0.9-x}\square_{0.1+x}O_{6.75-5x/2}\square_{0.25+5x/2}$ solid solution. The evolution of the calculated oxygen vacancies as function of the Nb/Y ratio is shown below.

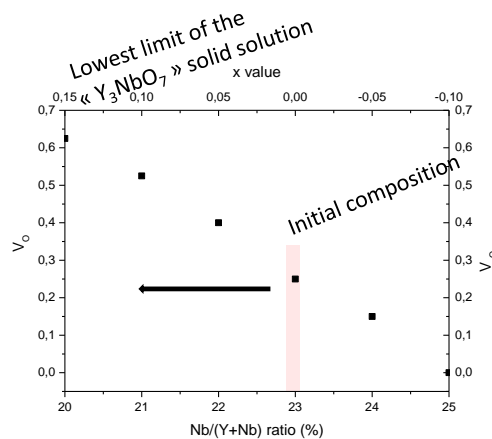


Figure 2.19: Evolution of the oxygen vacancies proportion in the $Y_3Nb_{0.9-x}\square_{0.1+x}O_{6.75-5x/2}\square_{0.25+5x/2}$ as a function of the Nb/(Y+Nb) ratio

2.1.3 Intermediary conclusion

Even if the Y_3NbO_7 compound is announced to be stable up to 1950°C , the luminescence studies performed on europium doped compounds clearly indicate that the environment of the doping element can be modified according to the heat treatment up to the phase decomposition. It should be noted that the spectral distribution appears clearly perturbed whereas the X-ray diffraction patterns show well crystallized fluorite-type defect materials.

2.2 Spark plasma sintering of Y_3NbO_7 : Eu phase

2.2.1 Introduction

Transparent ceramics attract a lot of attention as alternative materials to glasses and single crystals in a number of application fields such as armor, optical fibers, lasers, infrared materials.

Especially, considering optical materials, when transparency is reached, such ceramics can be used as scintillators, optical components solid state lasers and nonlinear optics **[Peuchert 2009][Klement 2008][Choi 1990][Cherepy 2007] [Chen 2013]**.

Indeed, transparent ceramics have been prepared for quite a long time, starting in the 50's **[Coble 1961]** and the first laser performance was recorded on a ceramic in the 90's **[Ikesue 1992][Ikesue 1995]**. Powder metallurgy processes are used to fabricate these transparent materials. The starting powders have been prepared using various methods such as solid state route **[Kobayashi 1992]** or chemistry synthesis routes **[Pechini 1967][Kakihana 1996][Okubo 1997]**. The densification processes have been performed by various sintering techniques. Most of the preparation processes of these ceramics rely on vacuum sintering. Such technique achieves better results than natural sintering under atmospheric pressure **[Jin 2010]**. Hot-pressing and hot-isostatic pressing methods present the main advantage to strongly reduce the internal porosity, giving rise to relative densities of 99.9% **[Podowitz 2010][Goldstein 2009]**. Fast heating processes like spark plasma sintering (SPS), plasma-activated sintering (PAS) or pulse electric sintering (PECS) are also known to lead to high density ceramics ($\geq 99\%$) but in very short times **[Krell 2003][An 2011-1][An 2011-2][An 2013][Fu 2013][Morita 2015][Li 2016][Groza 1992][Zhou 2003]**. Recently, use of spark plasma sintering technique has conducted to the development of new phases and it has been shown to be an effective process to obtain these dense and transparent materials **[An 2013]**. The current work is dealing with the development of ceramics for laser application in the visible range. Up to now, many results have already been reported on the sintering and the properties of Y_2O_3 , YAG or $MgAl_2O_3$ materials times **[Krell 2003][An 2011-1][An 2011-2][An 2013]**. In our work, we propose to investigate the sintering of a new class of materials, i.e. rare earth niobates in order to investigate their potential optical properties. These compounds present a RE_3NbO_7 formula (RE: rare earth elements). Recently, L. An *et al* **[An 2013]** reported the possibility to prepare Lu_3NbO_7 transparent ceramics using a SPS sintering process. For our part, we consider here Y_3NbO_7 and more precisely the Eu^{3+} doped Y_3NbO_7 phase, in order to investigate the sintering conditions that could lead to optical properties.

Since a pure phase and a completely dense ceramic are required to obtain interesting optical properties, SPS has been used to complete chemical reaction processes and sintering. Also, two preparation routes have been considered to prepare the Y_3NbO_7 phase and their influence on the sintering ability of the resulting powders has been investigated.

2.2.2 Experimental results and discussions

2.2.2.1 Synthesis

The sintered powders of composition $Y_{2.85}Eu_{0.15}NbO_7$ were prepared through solid state reaction and mineral sol-gel (Pechini) method described in part 2.1.2.1.1 and 2.1.2.1.3.

2.2.2.2 Sintering setup

SPS experiments were carried out in a Syntex Dr Sinter 515S machine. Powders were sintered at different heating rates (2, 5, 10°C/minute) up to several temperatures (from 1000°C to 1600°C) and held during 5 to 120 minutes under primary vacuum. A 100 MPa pressure was applied uniaxially from room temperature during all the sintering process.

After sintering, the obtained black ceramics were annealed at 900°C under oxygen during 2 hours to remove carbon contamination and oxygen vacancies. Then, the ceramics were mirror polished on both sides using diamond slurry.

2.2.2.3 SPS sintering of powders obtained from solid state route

The SPS sintering behavior of the calcined powder mixture was investigated by considering 3 sintering temperatures. Other parameters such as heating ramp or duration of the plateau were fixed to 5°C/min and 20 min, respectively. Sintered densities are given in Table 2.1 and corresponding XRD patterns are presented in Fig. 2.20.

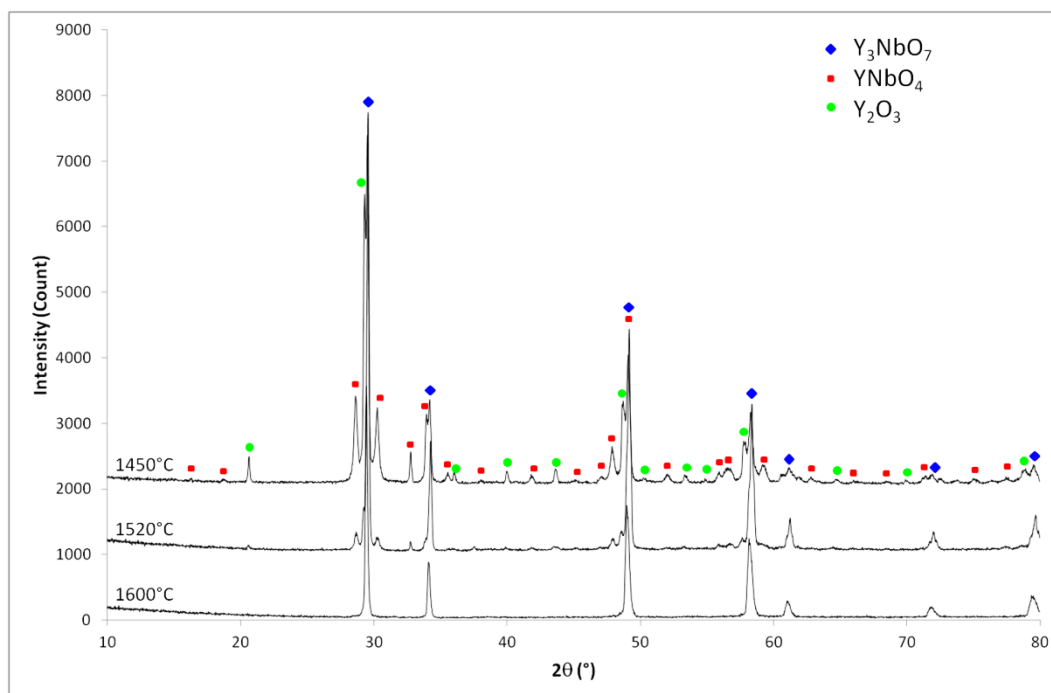


Figure 2.20: X-ray diffraction pattern of SPS sintered pellets (powder from the solid state route) as a function of the sintering temperatures (1450°C, 1520°C and 1600°C).

Table 2.1: Sintering conditions and final densities of SPS sintered pellets

SPS conditions	Relative density
5°C/min – 1450°C – 20 min	$d_{rel} = 99,2\%$
5°C/min – 1520°C – 20 min	$d_{rel} = 99,5\%$
5°C/min – 1600°C – 20 min	$d_{rel} = 98,9\%$

XRD measurements clearly shows that neither 1450°C nor 1520°C SPS heat treatment allows obtaining the pure Eu doped Y_3NbO_7 desired phase, although the final relative densities are quite high. Only the highest sintering temperature leads to the pure phase with a relative sintered density close to 99 %. As a matter of fact, for this solid state route, the Y_3NbO_7 phase is not completely formed after the 1300°C calcination step. Therefore, the SPS sintering step corresponds to a reaction sintering process and an increase of the sintering temperature is needed to obtain both the pure niobate phase and a high density. It should be noted that, even if final relative densities were equal or higher than 99 %, none of them were transparent, nor translucent. We tried to improve sintered densities and therefore optical properties by increasing the duration of the plateau from 20 to 120 minutes at 1600°C. Nevertheless, these samples were not transparent. In fact, XRD pattern (Fig. 2.21) shows new small peaks besides the niobate phase that can be attributed to $YNbO_4$ and Y_2O_3 . In that case, it could correspond

to the beginning of a decomposition of the Y_3NbO_7 phase under SPS conditions (high temperature, long sintering time and pulsed electric current).

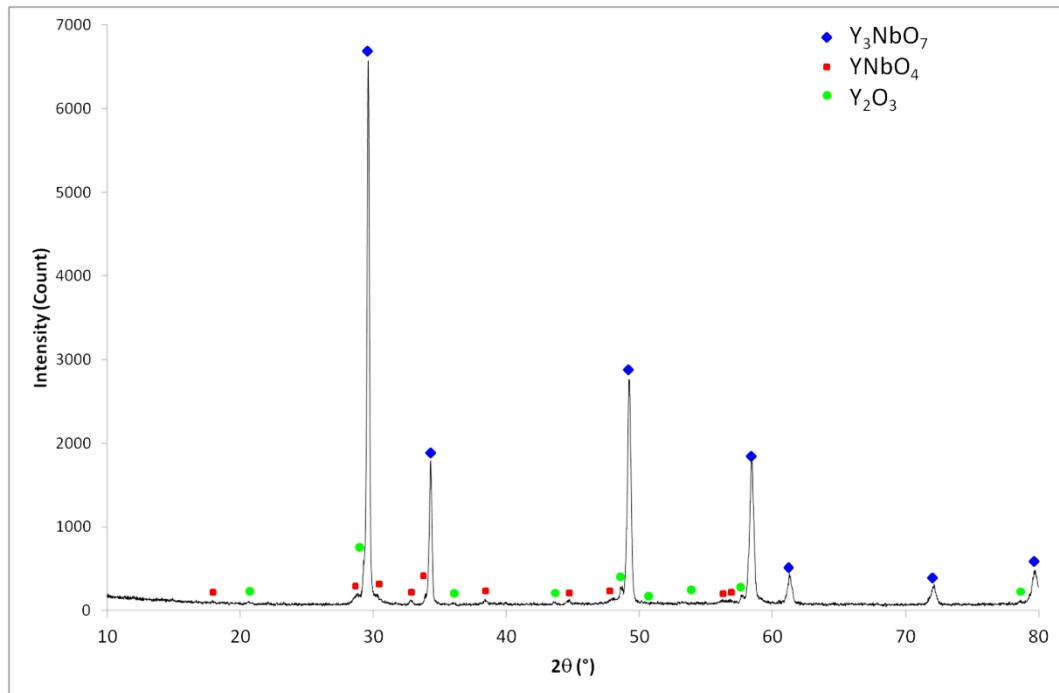


Figure 2.21: X-ray diffraction pattern of a SPS pellet, sintered at 1600°C during 120 min. Initial powder was obtained by solid state reaction

Therefore, we investigated another way to prepare the niobate phase, using a sol-gel route that aims to improve powder reactivity and sinterability.

2.2.2.4 SPS sintering of powders obtained Pechini route

The effect of the sintering temperature was first investigated. X-Ray patterns corresponding to the pellets sintered at 1100°C and at 1600°C are illustrated in Fig. 2.22.

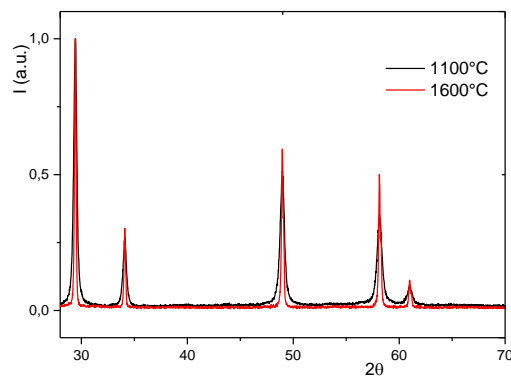


Figure 2.22: X-Ray patterns of the SPS pellets.

In addition to a strong increase of the crystallinity, the pellet does not present trace of impurities. A large increase of the pellet density from 62% to 97% is also associated to the increase of sintering temperature.

Based on these preliminary results, in order to obtain sufficiently high final densities, the following SPS sintering experiments were performed at 1600°C. In a first part, the role of the sintering time at 1600°C was investigated, considering a 5°C.min⁻¹ heating ramp. The purity of the phase and the relative density obtained after sintering are presented in Fig.2.23 and in Table 2.2. XRD measurements (Fig. 2.23) show that for the shorter times (10 and 20 min.), a pure niobate phase is obtained while some impurity peaks appear when the sintering time is higher than 40 min. Otherwise, SPS relative densities remain lower than 99 % for all samples and these values seem decreasing when sintering time is increasing. These two phenomena may be related to a partial decomposition of the Y₃NbO₇ phase as it was observed for the ceramics issued from the solid state route.

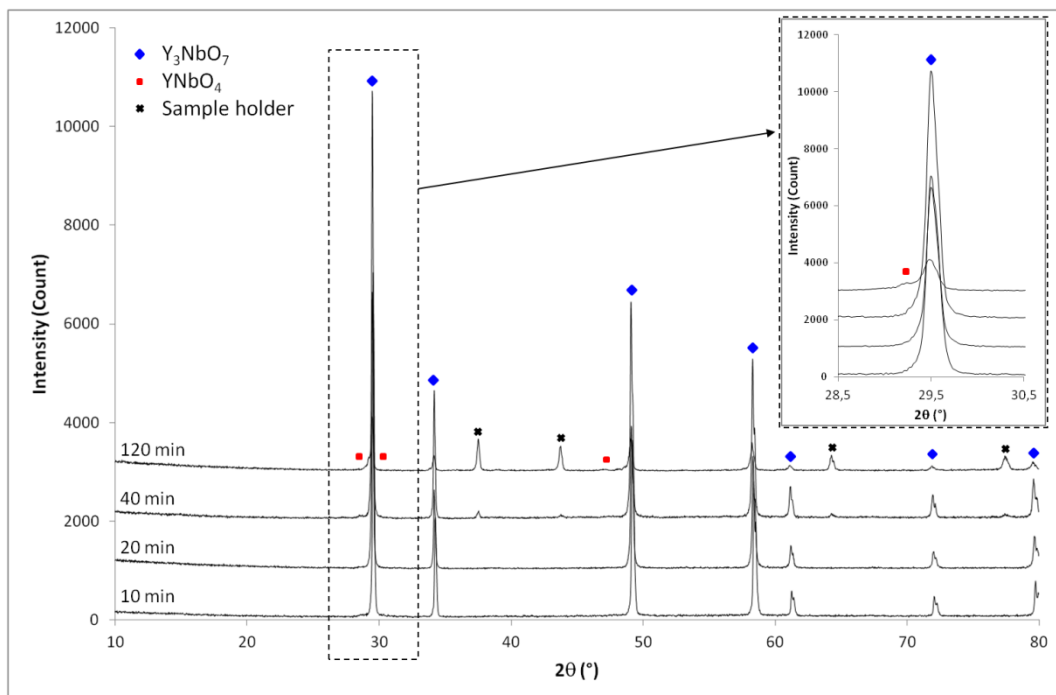


Figure 2.23: X-ray diffraction patterns of SPS pellets (sol-gel powder), as a function of sintering time at 1600°C (10 min, 20 min, 40 min and 120 min).

In a second part, the role of the heating rate was investigated, like in the case of the solid state route. Sintering results are given in Table 2.2, the microstructure of fractured pellets is presented in Fig. 2.24 and the corresponding X-Ray patterns in Fig. 2.25.

Table 2.2: Sintering conditions and final relative densities of sol-gel powders sintered by SPS.

SPS conditions	Relative density
5°C/min – 1600°C – 10 min	$d_{rel} = 98,7\%$
5°C/min – 1600°C – 20 min	$d_{rel} = 98,4\%$
5°C/min – 1600°C – 40 min	$d_{rel} = 97,8\%$
5°C/min – 1600°C – 120 min	$d_{rel} = 95,9\%$
5°C/min – 1600°C – 20 min	$d_{rel} = 98,4\%$
10°C/min – 1600°C – 20 min	$d_{rel} = 98,9\%$
50°C/min – 1600°C – 20 min	$d_{rel} \sim 90 \%$

In all cases, grains size looks homogeneous and a large grain growth can be observed, considering the size of the initial sol-gel powder heat treated at 700°C ($G_{700} \sim 9$ nm). For the highest heating rate (50°C.min⁻¹, Fig. 2.24 c, grain size is about a few hundred of nm but lower than 1 μm and grain shape remains rounded. Moreover, porosity appears quite high. It means that sintering is not complete in these conditions. For the other heating rates, average gains size is about 2 μm and polyhedron grain shapes are observed (Fig. 2.24 a and b). Some intragranular fracture is also observed which is consistent with the high level of densification of these samples.

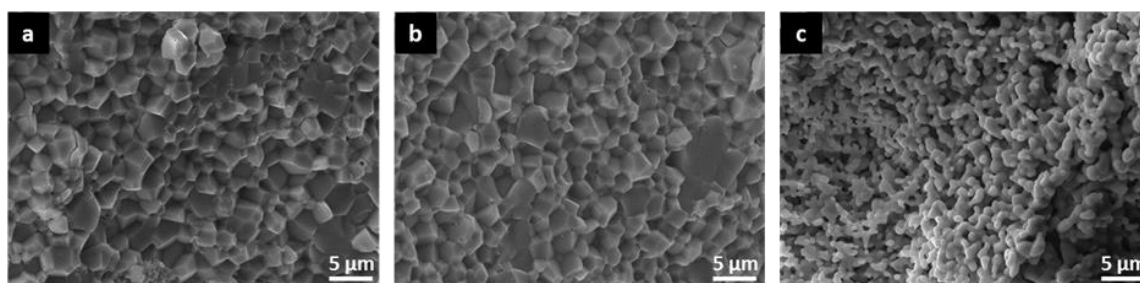


Figure 2.24: SEM micrographs of fractured SPS pellets (sol-gel powder), sintered at 1600°C during 20 minutes as a function of SPS heating ramp a) 5°C/min, b) 10°C/min, c) 50°C/min.

Concerning X-ray phase purity (Fig. 2.25), one can notice that only the lowest heating rate allows obtaining the pure niobate phase. A very low amount of $YNbO_4$ can be identified for a 10°C.min⁻¹ heating rate and some other phases are also present for the highest heating rate.

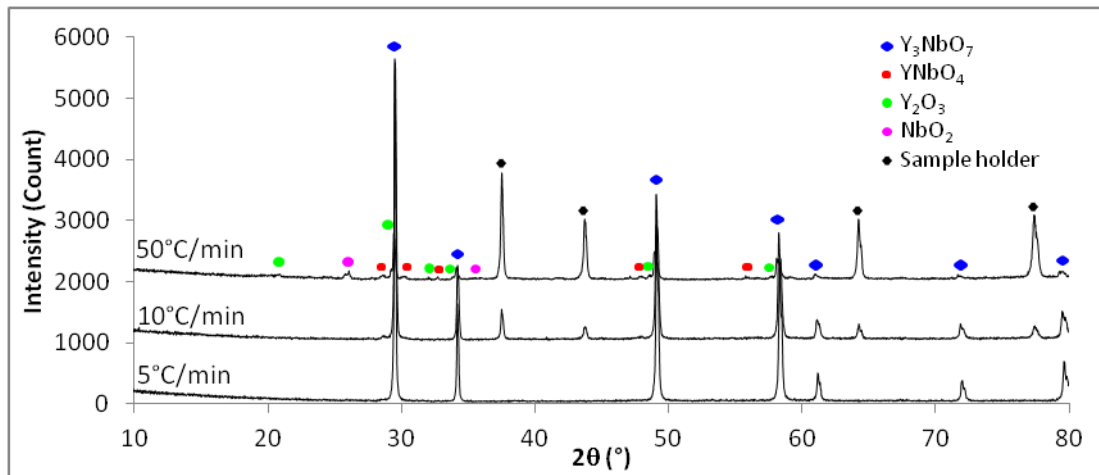


Figure 2.25: X-ray diffraction patterns of SPS pellets (initial powder obtained by Pechini synthesis route), sintered at 1600°C during 20 min. as a function of SPS heating ramp.

2.2.2.5 Influence of the reoxidation step

As demonstrated, the Y_3NbO_7 phase is really sensitive to the temperature. The SPS cycle is a reductive process and the as-sintered pellets are totally black colored (Fig. 2.26).



Figure 2.26: SPS pellets: as-sintered (left), heat-treated under oxygen at 900°C during 6h under O_2 (medium) and additional treatment at 1300°C 2h in air (right).

Regarding the XRD patterns, the SEM pictures and the optical analyses, a 6 hour heat-treatment at 900°C seems to be a good compromise to remove residual carbon at the surface of the pellet (due to the contact of the powder with graphite papyex during SPS), to re-oxidize the niobate phase and to avoid its decomposition into Y_2O_3 and/or $YNbO_4$.

The reoxidation step has to be taken into account the preparation of the raw powder. If a too high quantity of carbon is kept trapped within the grains, because of a too fast heat-treatment, the reoxidation step can result into a total disaggregation of the pellet. An example of a pellet prepared with a powder heat-treated under a Meker flame is presented below (Fig. 2.27).



Figure 2.27: SPS pellet issued from a powder heat-treated under a flame.

2.2.2.6 Optical characterization of the SPSed pellets

In order to go further in the chemical characterization of these ceramics, luminescence characterizations were performed on these pellets, taking advantage of the presence of Eu^{3+} as a local probe. Emissions curves are illustrated in Fig. 2.28, for excitations realized at 250 nm (a) and 290 nm (b). These wavelengths correspond to the maximum emission of (a) Eu^{3+} doped Y_2O_3 or YNbO_4 and (b) Y_3NbO_7 . Normalization of the curves was done at 629 nm. An increased contribution of Y_2O_3 and YNbO_4 impurities is clearly detected for the $10^\circ\text{C}.\text{min}^{-1}$ and $50^\circ\text{C}.\text{min}^{-1}$ samples (Fig. 2.28 a), reducing considerably the contribution of the Y_3NbO_7 niobate phase to the global emission. Response of the Eu^{3+} doped Y_3NbO_7 compound is reported in Fig. 2.28 b. Even if it is weak, the $50^\circ\text{C}.\text{min}^{-1}$ sample shows a lower response of the expected matrix and an additional contribution of the phases, resulting likely from the decomposition.

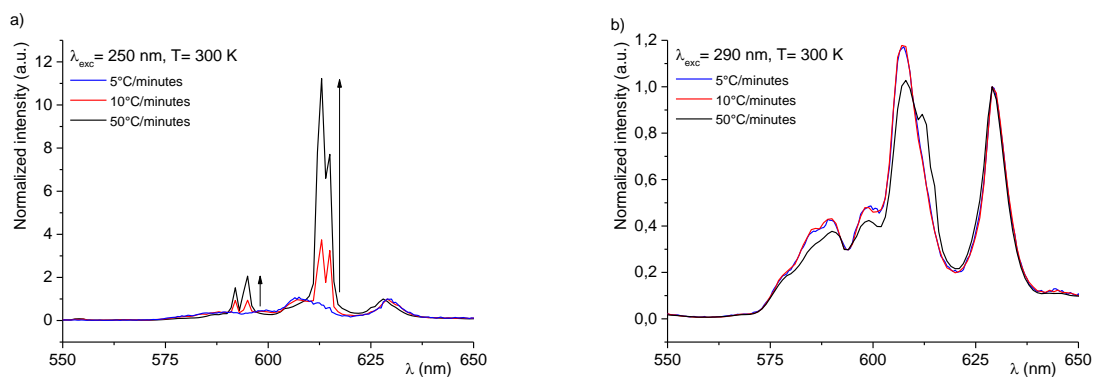


Figure 2.28: Emission spectra of Eu^{3+} doped Y_3NbO_7 ceramics (sol-gel powder) sintered at 1600°C during 20 min. as a function of SPS heating ramp, a) for an excitation at $\lambda_{\text{exc}} = 250$ nm revealing preferentially $\text{Y}_2\text{O}_3:\text{Eu}^{3+}$ and $\text{YNbO}_4:\text{Eu}^{3+}$ and b) for an excitation at $\lambda_{\text{exc}} = 290$ nm revealing preferentially $\text{Y}_3\text{NbO}_7:\text{Eu}^{3+}$.

2.2.3 Discussion

Solid state syntheses are generally easy to process and the purity of the as obtained phases can be controlled by the purity of the starting powders. In the case of the studied system, the $\text{Y}_2\text{O}_3\text{-Nb}_2\text{O}_5$ phase diagram (Fig. 2.5) shows the presence of another compound (YNbO_4)

besides the desired niobate phase (Y_3NbO_7). Given the grain size of the grinded powders and unavoidable heterogeneity present at grain scale in the powder mixture, a simple heat treatment performed at 1300°C has not been sufficient to form only Y_3NbO_7 , without $YNbO_4$. Increasing the temperature and/or duration of the heat treatment is the simplest way to improve the synthesis and reach the thermodynamic equilibrium. However, the niobate phase under study is a refractory material ($T_{\text{melting}} > 2100^\circ\text{C}$). So, it requires high temperatures which do not allow obtaining a powder presenting a high sintering ability (small grain size and non-agglomerated powder). That's why the use of SPS, combining temperature and pressure, on a 1300°C pre-reacted powder, has been looked as an effective way to obtain both phase formation and densification. The results presented in the previous sections show that i) high temperature, close to 1600°C , are required to form the Y_3NbO_7 phase, ii) final relative densities are high ($\sim 99\%$) but not enough to obtain transparency. This behavior is in agreement with the phase diagram and the high melting temperature of Y_3NbO_7 phase. Sintering temperatures of oxides are usually estimated at about $0,75 \times T_{\text{melting}}$ [German 1996] which is consistent with the 1600°C used value. Moreover, the increase of the sintering time, needed to improve sintered densities, results in the presence of new phases (as observed on XRD patterns). This was not observed on a Y_3NbO_7 powder, heat treated at 1600°C during 120 min. X-ray pattern only shows Y_3NbO_7 peaks. The specificity of the SPS method which applies an additional electrical field compared to natural or hot pressing sintering techniques is certainly the cause of this effect that can be attributed to a beginning of decomposition of the phase, as it will be discussed below. So, the experimental window (T° , time) for the SPS of a powder prepared by a solid state route appears quite small.

Two ways can be considered to overcome this drawback and increase sintered density of Y_3NbO_7 pellets. The first one would be the addition of a supplementary attrition milling step of the pre-reacted powder. But, in that case, pollution from the milling media may occur, even at the atomic level, which will be detrimental to the final optical properties. The second one is to promote the synthesis of a Y_3NbO_7 powder with smaller grain size. This corresponds to the sol-gel route that has been investigated in this work. Our results show that the proposed synthesis actually leads to the formation of Y_3NbO_7 at temperatures as low as 700°C , with nanometric grain size. Therefore, it has allowed us to study the SPS of a pure Y_3NbO_7 phase.

Our experiments show first that densification of this powder still needs high temperature, close to 1600°C . Second, the increase of the sintering time does not result in an improvement of the final densities. This is accompanied by the formation of new phases as demonstrated by XRD measurement for the longer times. Such a behavior is also observed when the effect of the heating rate is considered. XRD patterns also show new additional peaks for the highest heating rate. This is confirmed by the luminescence measurements which prove that some

Y_2O_3 and $YNbO_4$ impurities are present. Therefore, decomposition of the Y_3NbO_7 phase must be considered according to the simple following reaction: $Y_3NbO_7 \rightarrow YNbO_4 + Y_2O_3$

According to the Y_2O_3 - Nb_2O_5 phase diagram (Fig. 2.5), Y_3NbO_7 compound is supposed to be stable at high temperatures, up to its congruent melting that is reported above $2100^\circ C$ [Kakihana 1996]. So, the question of the stability of the Y_3NbO_7 phase in the conditions of SPS is raised, since either increasing sintering time or heating rate leads to a decomposition of the phase. The role of the current is clearly pointed out considering the highest heating rate. For a $50^\circ C \cdot min^{-1}$ value, the increase of temperature needs a high intensity current. The powder is then submitted to a high electrical field that can induce ionic conduction and therefore promote decomposition of the Y_3NbO_7 , phase. In a previous work dealing with the thermal evolution of a $Y_3Nb_{0.9}O_{6.75}:Eu^{3+}$ (5% molar substitution) powder followed by luminescence characterization, we have demonstrated that the environment of the doping element (Eu) is changing according to the heat treatment, up to the beginning of the decomposition of the initial phase above $1600^\circ C$ [Kim 2016]. It means that the Y_3NbO_7 , phase is not so stable at high temperature and this metastability is enhanced in SPS conditions, under electrical current. As a matter of fact, more investigations should be done on the Y_2O_3 - Nb_2O_5 equilibrium phase diagram, around the Y_3NbO_7 composition at high temperature.

The densification of a pure Y_3NbO_7 phase appears not so straightforward, even using SPS. It needs a high temperature, a short sintering cycle and a moderate heating rate, in order to avoid the beginning of the decomposition of the phase. For our sol-gel powder, the optimal sintering cycle was actually realized with a $5^\circ C \cdot min^{-1}$ heating ramp, up to $1600^\circ C$ during 20 min, under a 100 MPa pressure. The obtained ceramic was pure and translucent but not transparent. The presence of agglomerates within the calcined sol-gel powder may explain that full density and transparency was not reached. A mild additional grinding of the calcined powder before sintering could be a way to improve final density in the optimal sintering conditions.

2.2.4 Intermediary conclusion

The synthesis and the sintering of the Y_3NbO_7 phase have been investigated. Due to the refractory nature of this phase, solid state reaction from individual oxides needs high temperature, about $1600^\circ C$, to obtain a pure phase (XRD characterization). SPS of a $1300^\circ C$ pre-reacted mixture powder gives dense and pure pellets after $1600^\circ C$ SPS. However, densities are not high enough to observe transparency. The use of a sol-gel synthesis allows obtaining the pure Y_3NbO_7 phase from $700^\circ C$. However, SPS of this powder is still difficult. The sintering study of the pure Y_3NbO_7 phase shows that, at $1600^\circ C$, the niobate phase is metastable, especially in SPS conditions, i.e. in the presence of a high electrical field. A

decomposition of the pure Y_3NbO_7 compound is clearly demonstrated when high heating rates were used, as shown by luminescence measurements. So, the SPS experimental conditions are quite constraints. The optimal sintering cycle implies a $5^\circ\text{C}\cdot\text{min}^{-1}$ heating rate, a 1600°C sintering temperature and a 20 min. sintering time. The as-obtained ceramic is translucent. In order to reach full transparency, sintering ability of the sol-gel powder should be increased, by limiting for example presence of agglomerates within the powder.

2.3 Tailoring of the composition and optical properties of Eu³⁺ doped-Y₃NbO₇ niobate induced by spark plasma sintering

2.3.1 Introduction

Structural studies of the Re₃NbO₇ (Re, rare earth) were performed and revealed peculiar behaviors. For the biggest rare earth matrix (from La, to Nd) the materials crystallize in the Pnma space group. It adopts the C222₁ symmetry for Sm-Tb and finally a cubic Fm-3m space group for the smallest rare earth elements, Dy-Lu [Rossel 1979][Doi 2009]. Within the cubic space group compound (Lu, Y), microscopy characterization revealed local nano-domains which were identified as pyrochlore nano-domains [López-Conesa 2013][Miida 1997]. even if some authors announced that the too low intensity of the additional diffraction spots are not consistent with the reflections of the Fd-3m space group [Allpress 1979][Withers 1992]. Complementary Raman spectroscopy confirms the position of vibrational modes, which excludes a pure fluorite structure [Kovyazina 2003].

Because trivalent europium luminescence is sensitive to the local environment, we doped the yttrium matrix to investigate this structure. We recently published first results of the europium emission as function of the temperature [Kim 2016]. This study reports a maximum of intensity due to the ⁵D₀₋₇F₂ electric dipole transitions. The global spectral distribution shows a thermal evolution of the solid state solution and a decomposition is detected for the longest thermal treatment above 1100°C. This results in the appearance of emission peaks associated with the location of Eu³⁺ ions in Y₂O₃ and YNbO₄ phases resulting from the decomposition process.

Powder material was sintered through SPS process to ensure a high crystalline state and favor the stabilization of the rare earth environment within the host. A pellet which does not present trace of impurity regarding the optical response was selected for the present investigation. We propose here a correlation between the optical response, the structural characterization performed through SEM, X-Ray diffraction, TEM and the SPS process.

2.3.2 Experimental results and discussion

2.3.2.1 Synthesis

The synthesis route is based on the mineral sol-gel (Pechini) method described in part 2.1.2.1.3. The ratio between Nb/Nb+Y was fixed to 25% and the amount of Eu³⁺ ions was equal to 5% of cationic molar substitution.

2.3.2.2 SEM pictures

The initial europium doped niobate powder, prepared by Sol-Gel method, is observed in Fig. 2.29 a-b. These micrographs show micrometric agglomerates, made of nanometric grains with homogeneous size between 80 and 100 nm.

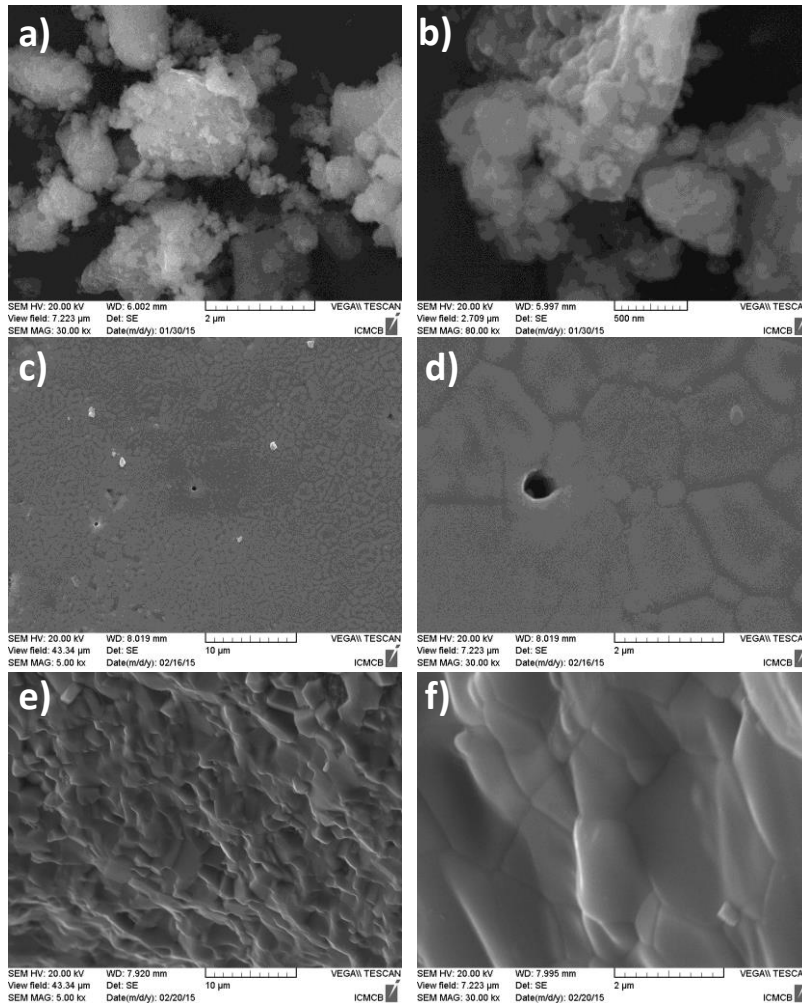


Figure 2.29 SEM pictures of the Eu^{3+} doped niobate initial powder prepared by Pechini synthesis route (a, b), and of the sintered pellets : surface (c, d) and fracture (e, f).

Fig. 2.29 c-d show the surface of the dense ceramics obtained after SPS sintering process. A low amount of intergranular porosity with a spherical shape can be observed which is consistent with the high relative density (98%) measured by the Archimedes method. The SPS sintering process induced an increase of the grain size and a large distribution in sizes, ranging from 400 nm to 2 μm (Fig. 2.29 c-f).

The fracture of the sintered material is occurring through an intergranular mode as it can be seen in figures 2.29 e-f. It is a classic feature for dense ceramic materials and it is consistent

with the high density obtained in our case. These micrographs also reveal a good densification in the volume of the samples.

2.3.2.3 Luminescence characterization

Excitation and emission spectra obtained at room temperature on the Eu^{3+} (5 mol%) doped- Y_3NbO_7 pellet are shown in Fig. 2.30.

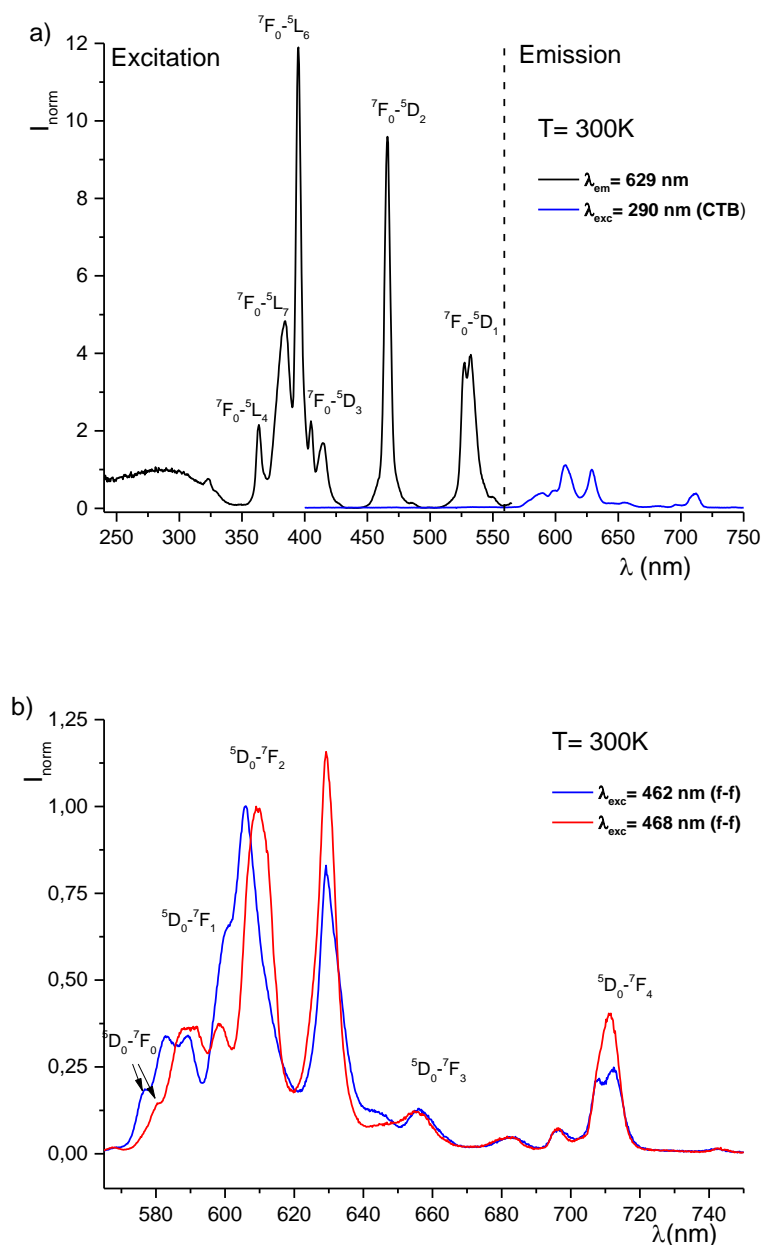


Figure 2.30- Luminescence spectra of Eu^{3+} doped Y_3NbO_7 pellet. Excitation graph, illustrated in a-left), shows a strong quenching of the charge transfer band (CTB). Excitations in the CTB a-right) or in the 4f lines b) lead to unstructured emission lines maximum in the red range.

Excitation performed at 290 nm revealed a maximum of the emission due to the hypersensitive 5D_0 - 7F_2 electric dipole transition. As observed on powder in previous work, the spectral distribution is quite large and similar to that observed in an amorphous or low crystallized environment [Kim 2016]. No clear discrimination of the Stark component splitting can be done under such an excitation wavelength. The excitation spectrum is constituted by large UV absorption bands ranging between 230 nm and 300 nm. The absorptions are linked to the electron charge transfer from the oxygen ligand (charge transfer band, CTB) to the empty orbital of europium ions at the highest energies [Jubera 2013] and probably to the charge transfer from oxygen to niobium at the lowest energies [Hirano 2013]. One can notice a significant decrease of the pellet CTB intensity in comparison to that of the initial powder described in paragraph 2.1.2.5 (Fig. 2.13). Because of the reducing SPS conditions, one cannot totally re-oxidize the pellet and remove the oxygen vacancies. In addition it may be possible that traces of the niobium cations are not present at the +V oxidation state but are stabilized at the +IV oxidation state. First EPR characterization seems to confirm this last point. All these phenomena should contribute to competitive absorptions which may reduce the efficiency of Eu^{3+} ions. In addition to the large band, 4f-4f absorption lines of the rare earth ions are detected. Their intensities are enhanced compared to that of the UV CTB due to a configurational quenching of the emission which results in a direct non radiative de-excitation from the charge transfer band to the 7F_J fundamental states. This non-radiative process is by consequence a drawback that forbids the use of such red emitting phosphor for application requiring high quantum efficiency.

Selective excitations were performed to obtain a more precise resolution of the emission graph. Two spectral distributions were isolated under excitation at 462 nm and at 468 nm. The corresponding emission graphs are reported in Fig. 2.30 b. The two Eu^{3+} fingerprints revealed that the anionic polyhedra around the doping element possess two specific geometries which induce changes of the Stark component splitting. None of these sites seem to be well defined as the width of each peak is large and the intensity of the electric dipole transitions reveals a lack of inversion center. These measurements were repeated at liquid He temperature (4 K) to reduce the thermal contribution to the global emission broadening (Fig. 2.31).

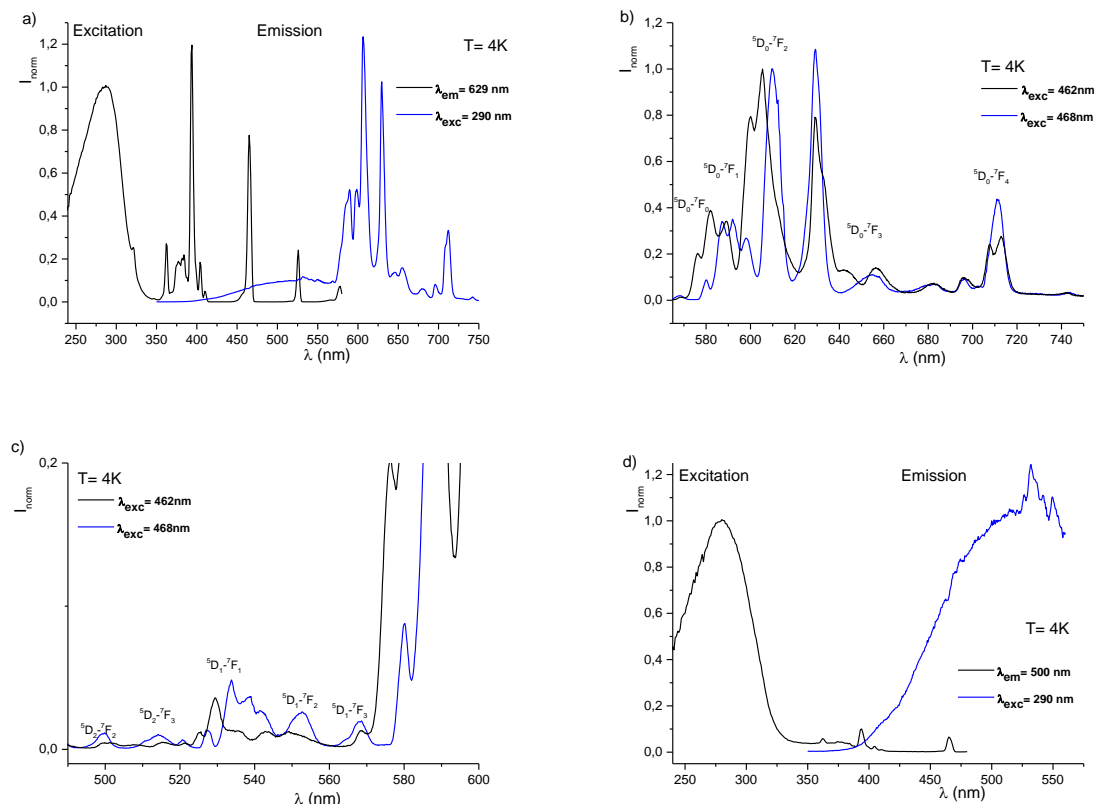


Figure 2.31- Luminescence spectra of Eu^{3+} doped Y_3NbO_7 pellet at 4 K. Excitation graph, illustrated in a-left), shows a higher contribution of the Eu-O charge transfer band (CTB). Excitations in the CTB or in the 4f lines are shown in a-right) and b), c) respectively. d) illustrates an intrinsic emission of the niobate matrix.

Fig. 2.31 a-c illustrates the excitation and emission graphs related to the europium luminescence, measured at 4K. One can observe on the excitation curve (Fig. 2.31 a) a clear increase of the CTB intensity in comparison to that of the 4f-4f absorption lines. This confirms the high impact of a too low location of the CTB, which contributes to the strong configurational quenching observed at room temperature. The decrease in temperature does not reveal a better structuration of the lines. Selective excitation and emission spectra were performed to definitely attribute the nature of the observed lines. Corresponding graphs are reported in Fig. 2.32. The decrease of the 600-620 nm lines intensity clearly discriminates the contribution of the magnetic and electric dipole transitions. Table 2.3 lists the position and attribution of the different lines observed on the emission curve under a 462 nm and a 468 nm excitation wavelengths.

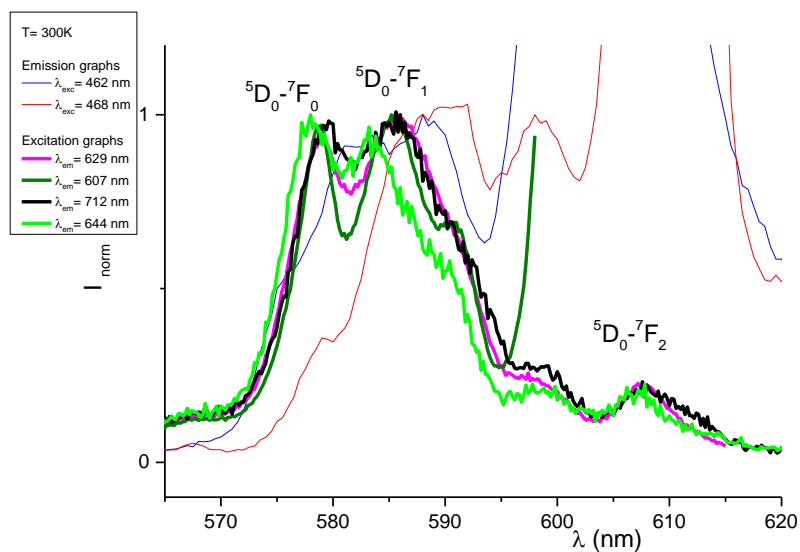


Figure 2.32- Superposition of different emission and excitation graphs of Eu^{3+} doped Y_3NbO_7 .

Table 2.3- Eu^{3+} transitions observed at 4 K/300 K

Transitions	Emission 1	Emission 2
	$\lambda_{\text{exc}} = 462 \text{ nm}$	$\lambda_{\text{exc}} = 468 \text{ nm}$
${}^5\text{D}_2\text{-}{}^7\text{F}_2$	495-503	495-503
${}^5\text{D}_2\text{-}{}^7\text{F}_3$	506-522	506-522
${}^5\text{D}_1\text{-}{}^7\text{F}_1$	522-546	522-546
${}^5\text{D}_1\text{-}{}^7\text{F}_2$	546-560	546-560
${}^5\text{D}_1\text{-}{}^7\text{F}_3$	568	568
${}^5\text{D}_0\text{-}{}^7\text{F}_0$	576*	580*
${}^5\text{D}_0\text{-}{}^7\text{F}_1$	582 589.2	587 592 598
${}^5\text{D}_0\text{-}{}^7\text{F}_2$	600 605.4 629.4	610 629.2
${}^5\text{D}_0\text{-}{}^7\text{F}_3$	642.7 656.6	655
${}^5\text{D}_0\text{-}{}^7\text{F}_4$	682 695.8 707.6 712.8	682 696.4 702.8 711.2

* Uncertainty remains in the attribution of these lines because of the presence of a thermal population of the ${}^7\text{F}_1$ at room temperature.

At this concentration (5% of molar substitution equivalent to 10^{21} ions.cm⁻³), radiative de-excitation from ⁵D₂ and ⁵D₁ level are still detected between 480 nm and 570 nm (Fig. 2.31 c) under excitation in the ⁵D₂ level.

Regarding the global emission, it is quite unexpected to obtain such a proportion of the electric dipole transition of Eu³⁺ within a fluorite matrix. Indeed, one can totally exclude the location of europium ions in the octahedral regular cationic environment of the fluorite host or the sixfold and eightfold coordination polyhedra of the pyrochlore structure which often results from the deformation of the fluorite structure. In later case, the larger site possesses a D_{3d} symmetry. The ⁵D₀-⁷F₁ magnetic dipole transitions split into A and E component. The energy difference between the two lines was studied in different pyrochlore matrices and it was shown that it varies as a function of the radius size difference between the A and B cations of the A₂B₂O₇ compounds [Cauley 1973][Hirayama 2008]. The luminescence of europium doped pyrochlore is mainly due to the magnetic dipole transitions and the corresponding emission is orange. Moreover, a few examples of red emission of fluorite or pyrochlore can be found in the literature. The local symmetry is lowered to the D_{2d} punctual symmetry for most distorted polyhedra in fluorite-type Ce_yZr_{1-y}O₂ solid solution [Fornasiero 2004]. The fluorite Ce_yZr_{1-y}O₂ presents a red surface emission due to disturbed local sites. Thermal evolution of surface and bulk response is reported by Montini et al [Montini 2009]. Among all the pyrochlore structures, the La₄Gd₁₁EuHf₁₆O₅₆ Hafnate or the La₄Gd₁₁EuZr₁₆O₅₆ zirconate present an optical response quite similar to the Eu³⁺ doped Y₃NbO₇. But the authors point out a low crystalline rate of the studied materials and the occurrence of amorphous-type environments which can justify the lack of symmetry around the rare earth element [Cauley 1973]. These optical characterizations definitely exclude the location of Eu³⁺ ions in pyrochlore-type environments. Considering the observed emission of Eu³⁺ doped niobate, we cannot exclude the fact that, each of the observed 1 and 2 emissions are associated to a unique environment, as selective excitations show modification in the intensity ratio of the electric dipole transitions (Fig. 2.33). But no fingerprint of the expected secondary phases as Eu³⁺ doped Y₂O₃ or YNbO₄ is detected. At this stage and knowing that thermal treatment affects the spectral distribution as previously demonstrated, we performed complementary structural characterizations to identify the optical response of europium ions in this material.

In addition, the low temperature makes possible the observation of a large emission band related to the niobium-oxygen charge transfer emission (Fig. 2.31 d-right, blue curve). The corresponding absorption consists of a large band, peaking at around 300 nm (Fig. 2.31 a-left, black curve). Such charge transfer emission of anionic groups is well known in molybdate or tungstate host lattice and because of a large Stokes shift, it is generally strongly quenched at room temperature [Blasse 1993][Glorieux 2011]. Recently it has been reported in the YNbO₄ matrix [Hirano 2013].

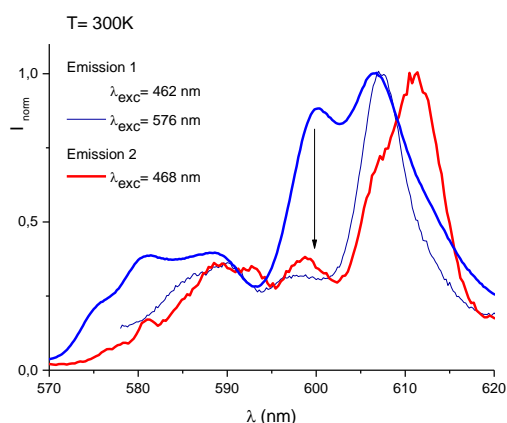


Figure 2.33: Selective emission spectra of Eu^{3+} doped Y_3NbO_7 .

2.3.2.4 X-ray diffraction

Synthesis of the pure Eu_3NbO_7 compound was performed through the same synthetic route as the yttrium phase to detect if the introduction of 5% of europium could reduce the cubic symmetry of the yttrium niobate phase. Indeed, the europium phase is announced to be orthorhombic and crystallizes with the $C 222_1$ space group [Doi 2009]. Experimental diffraction peaks perfectly match with the cubic yttrium phase crystallizing in the $Fm-3m$ space group (Fig. 2.34). As a consequence, it can be said that the substitution of yttrium ions by europium ions will not affect the global symmetry of the host.

Pattern matching and Rietveld refinements were then performed on a crushed pellet sintered in the same SPS conditions than the one studied before. A one hour longer post-heat-treatment under oxygen was performed on this sample in comparison with the one described on Fig. 2.30 to 2.32. The objective of the post-heat-treatment was to re-oxidize the pellet after the reducing SPS sintering process. The longer post-heat treatment results in a light decomposition of the niobate phase and traces of the Fergusonite are clearly visible on the Fig. 2.35. Moreover, the monochromatic-type acquisition makes possible the observation of diffraction peaks splitting, at the biggest angles range, which reveals the stabilization of two distinct fluorite-type compounds. By consequence, the refinements were run with two fluorite unit cells crystallizing in the $F m-3m$ space group.

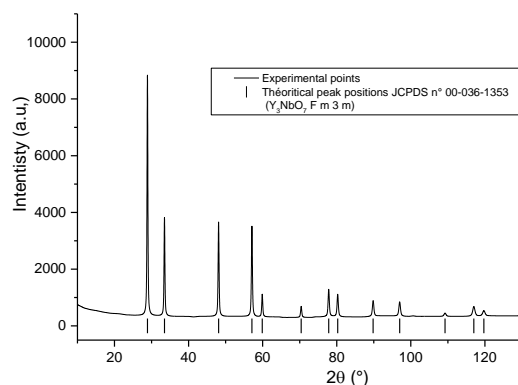


Figure 2.34: X-Ray diffraction pattern of Eu_3NbO_7 (JPDS N° 00-036-1353)

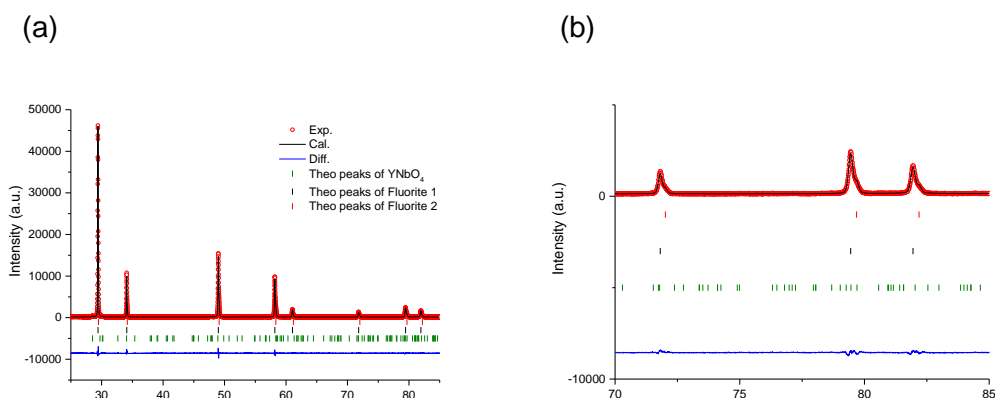


Figure 2.35: a) Pattern matching refinement of a Eu^{3+} (5 mol%) doped Y_3NbO_7 pellet °C sintered at 1600°C. b) Zoom of the highest angle region.

At this stage, different XRD patterns were run on several powders, containing different niobium content and heat-treated at 1600°C, in order to show the evolution of the cell parameters as well as the shape of diffraction peaks at the high angles as a function of the niobium content. Under an equivalent heat-treatment performed in a classical furnace during the same time, no splitting of the diffraction peaks can be distinguished on the X-Ray diffraction patterns (Fig. 2.36). But for the lowest niobium content (21 %), traces of Y_2O_3 are detected whereas the X-ray pattern reveals the predominance of Fergusonite impurities in the highest niobium content (27%) compound. Barker *et al* and J-H Lee *et al*. showed that a parameter of the fluorite cubic solution decreases from 5.264 Å to 5.243 Å in the 20 to 28% of niobium molar percentage range [Barker 1984][Lee 1998]. Fig. 2.37 reports our experimental results in the 21%-27% targeted range of niobium ratio. Unfortunately, our samples, with 21 and 27 % Nb ratio, underwent a decomposition giving rise to Y_2O_3 and/or YNbO_4 under the 1600°C heat-treatment; the corresponding refined cell parameters converge on a value which is consistent with 24-25% of niobium content. However, a 23% niobium content compound was obtained on

a material treated a lower temperature (900°C) and for which no trace of impurity was detected. This last point matches perfectly with the linear law obtained by Barker and Lee.

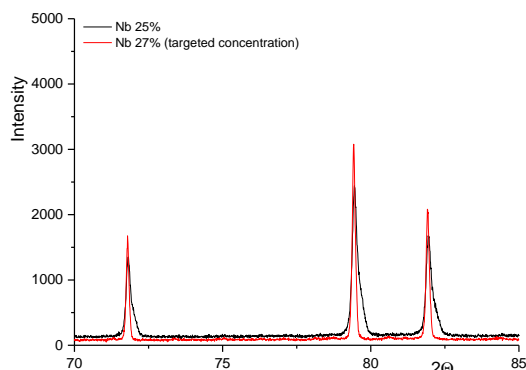


Figure 2.36: XRD patterns of Eu^{3+} doped Y_3NbO_7 (Nb 25%) and $\text{Y}_3\text{Nb}_{1.125}\text{O}_{7.31}$ (Nb 27%, targeted concentration).

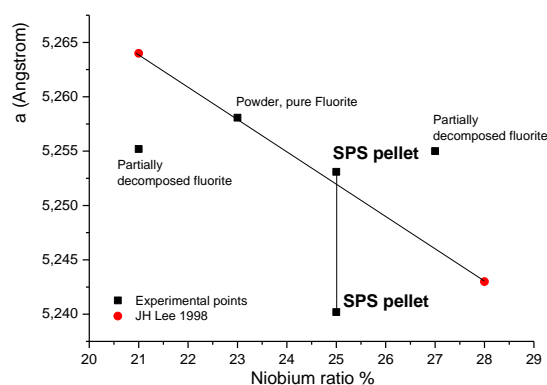


Figure 2.37: Evolution of the a-cell parameter as a function of niobium content in niobate compounds. The vertical line corresponds to the splitting of the diffraction peaks observed for SPS sintered samples. Linear variation is derived from the data of JH Lee [Lee 1998]

The cell parameters of the two fluorite-type host lattices stabilized in the pellet after SPS cycling are distributed on both side of the linear law which confirms the evolution of the composition during the sintering process. The obtained cell parameters are equal to $5.2531(1) \text{ \AA}$ and $5.2402(2) \text{ \AA}$.

This fluorite-type host lattice is known to present ionic conductivity properties. Due to oxygen mobility within the solid solution, the anionic conductivity was demonstrated by J-H Lee *et al* [Lee 1998] for several niobium contents. As a consequence, we suggest that the SPS sintering process, which implies current circulation from the top side to the back side of the pellet, forces oxygen mobility and favors the cubic fluorite-type solid solution splitting into two different compositions.

In addition, a zoom in the low intensity diffraction zone revealed additional large contribution which cannot be taken into account by the two defined fluorite composition or cannot be explained by a modification of the symmetry like pyrochlore deformation (Fd-3m space group), fluorite defective matrix as sesquioxide (I a-3) or a lowering of the symmetry as for the Gd₃NbO₇ matrix (C cmm space group) (Fig. 2.38).

Therefore, complementary characterizations have been performed by TEM in order to detect potential inhomogeneity at grain scale within the sintered pellet.

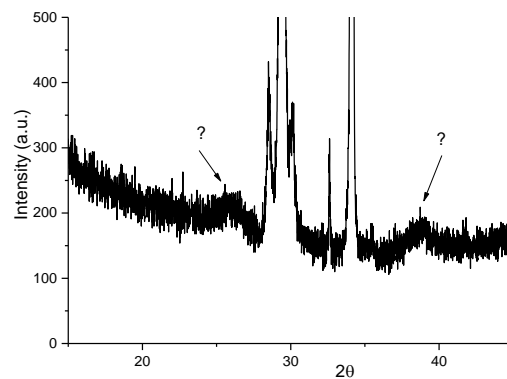


Figure 2.38: X-Ray diffraction pattern of Eu³⁺ doped-Y₃NbO₇ at low angle

2.3.2.5 Electron diffraction

Electron diffraction patterns were collected on a JEOL 2100 transmission electron microscope, working at 200 kV and equipped with a double tilt specimen stage. Prior to its observation, a suspension of the specimen in alcohol was prepared and a drop was deposited on a carbon coated grid.

TEM of several pyrochlore and fluorite cubic oxygenized matrices are reported in the literature [García-Martin 2000][Withers 1992][López-Conesa 2013]. In most of them and especially in the RE₂O₃-Nb₂O₃ systems, additional diffraction spots attributed to superstructure microdomains existing in fixed orientation or superstructure are discussed. Concerning the Y₃NbO₇ matrix, Allpress et al. and Miida *et al.* described several weak and diffuse spots in addition to the strong spots, typical of the fluorite phase [Allpress 1979][Milda 1997]. These spots cannot match with those of an orthorhombic or pyrochlore structure.

Fig. 2.39 illustrates electron diffraction patterns obtained on the SPS sintered crushed pellet. Nevertheless, differences exist from one grain to another one as illustrated on Fig. 2.39

a and 2.39 b. These two patterns correspond to the same zone axis. Strong and sharp Bragg reflections are clearly consistent with the fluorite Fm-3m cell. However, while only the Fm-3m reflections are observed on Fig. 2.39 a, diffused but localized spots are seen on fig. 2.39 b.

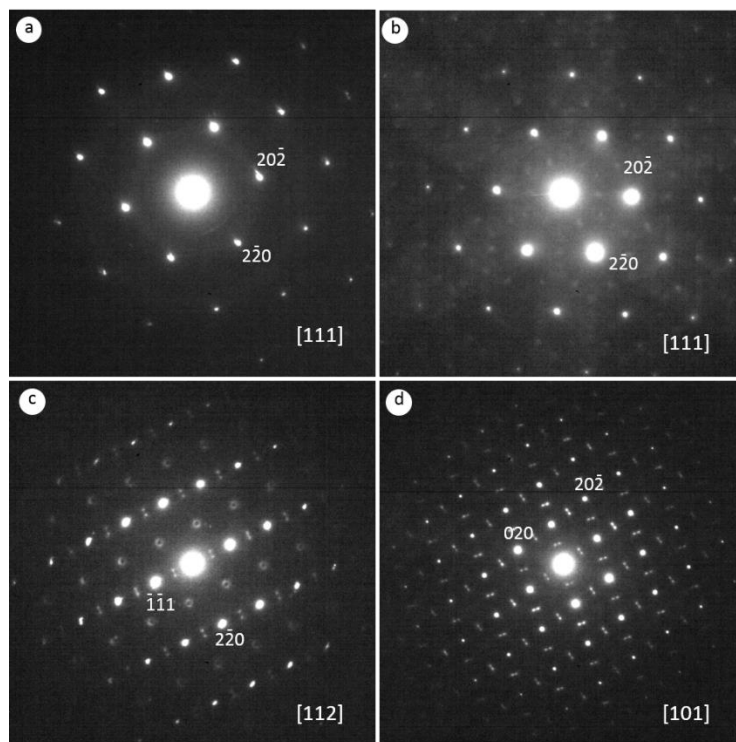


Figure 2.39: Electron diffraction patterns of the Eu^{3+} doped Y_3NbO_7 pellet

The orientation of the latter crystal in the microscope led to patterns 2.39 c and 2.39 d. In these patterns, the more intense reflections belong to the Fm-3m cell. Additional double spots as well as rings are clearly visible. The double spots lie systematically around the position $\{\frac{1}{2} \frac{1}{2} \frac{1}{2}\}$. The distance between the two spots of the doublet is around 0.45 nm^{-1} and this distance is always the same whatever the orientation of the pattern is. In Fig. 2.39 c in addition to the double spots already described, one can observe a ring centered at positions $\{\frac{1}{2} -\frac{3}{2} \frac{1}{2}\}$. The diameter of the ring, $\approx 0.45 \text{ nm}^{-1}$, is comparable to the distance between the two spots of a doublet. From these observations one can conclude, as Withers *et al.* [Withers 1991] already did, that the additional doublets are part of a ring of diffuse intensity. From the fluorite structure, two type of superstructures have been identified: the so called C-type structure and the pyrochlore structure. The former is characterized by two sets of additional reflections localized at $\frac{1}{4} \{220\}$ and $\{001\}$. The latter gives also rise to two sets of superstructure spots but located at $\frac{1}{2}\{111\}$ and $\{001\}$. The observed diffuse rings appear around the expected positions for the ideal pyrochlore superstructure. However, we observed diffuse rings and not ideal spots which indicates that there is only a local ordering. It should be

also noted that we did not observe any spot nor diffusion at the {001} position which is consistent with the observation of Lopez-Conesa *et al* [**López-Conesa 2013**].

At least, it should be noted that the very weak diffusion observed in the $\langle 220 \rangle^*$ directions on the 2.39 b pattern is no more present on the 2.39 c pattern. Two explanations can be proposed: either it is a very localized phenomena and the two diffraction patterns are not obtained exactly from the same area or as the orientation of the crystal is different, the projected thickness of the specimen is different and do not allow the observation of a so weak phenomena.

Such discrepancy concerning regular fluorite array was already mentioned by several authors who observed that Raman spectroscopy results were not consistent with the Fm-3m space group. Because of their compatibility with the Fd-3m symmetry, they were attributed to a pyrochlore structure and to a local ordering of the vacancies leading to domains which sizes are inferior to the sensitivity of the X-Ray analysis [**Cai 2007**][**Kovyazina 2003**].

2.3.2.6 Discussion

As demonstrated by the structural characterizations, the composition of the Y_3NbO_7 intermediate compound can be modulated by the SPS heat-treatment, which favors oxygen mobility under current and probably by the post re-oxidation step of the pellet, which could modify the oxygen ratio. The electronic diffraction microscopy reveals in addition to the typical satellite reflections of defect-type fluorite structure, inhomogeneity between grains belonging to the same pellet. As a consequence, the two spectral distributions of the europium emission could be attributed to the location of the europium ions into the two fluorite-type host lattice. The emission spectroscopy of trivalent europium reflects the dual nature of the sintered pellet as two extreme spectral distributions are observed. It can be reasonably said that it also reflects the gradual transition between two different compositions, which results in a large and undefined spectral distributions of the Eu^{3+} radiative transition.

The luminescence of the 21% and 27 % niobium content (targeted niobium content) were checked to determine if stabilization into two fluorite unit cells is linked to the thermal decomposition in addition to the SPS effects. In both cases, as for the 25% niobium content powder studied in K-Y Kim *et al* [**Kim 2016**], a unique large emission response is observed, whatever the excitation wavelength (Fig. 2.40). The spectral distributions indicate a small shift of the maximum between the two niobium content powders. The emission 1 is lightly closer to the highest niobium content whereas the emission 2 better matches with the 21% of niobium content (Fig. 2.40 a). A systematic study as function of the niobium content will be run to determine the attribution of emission 1 and 2 regarding the niobium concentration. At this stage, we can say that higher niobium content is associated with a decrease of the oxygen vacancy rate within the host. The local environment of the doping element is supposed to be

less defective and more regular. By consequence, even if the main part of the emission due to the electric dipole transition, the ratio between the magnetic dipole transition and the previous ones is expected to be higher for the highest niobium content matrix.

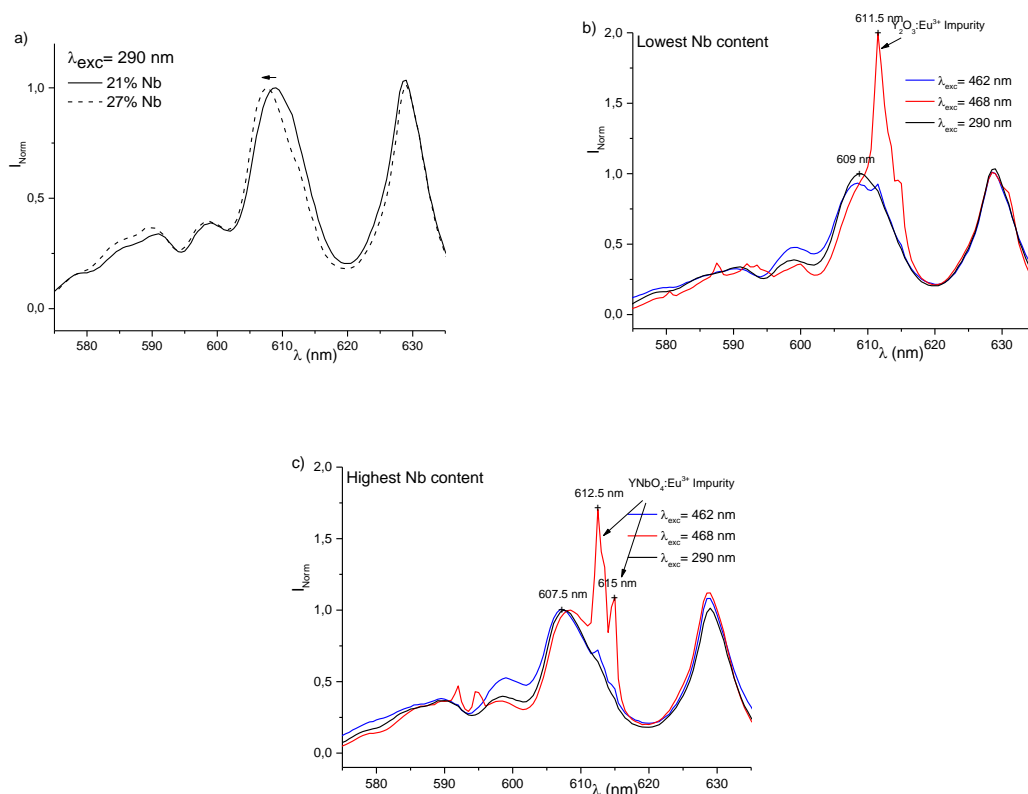


Figure 2.40: Emission of Eu³⁺ 5% doped- Y₃Nb_{0.8}O_{6.5} (21% of niobium) and Y₃Nb_{1.125}O_{7.5} (27% of niobium) powders under excitation in a) the charge transfer band at 290 nm and b) and c) in the 4f absorption line.

Excitations in the 4f lines reveal for both compositions the presence of impurity contribution. The lowest niobium content emission graph (Fig. 2.40 b) shows lines of Eu³⁺-doped Y₂O₃ sesquioxide whereas the 27% compound preparation contains Eu³⁺ doped YNbO₄ (Fig. 2.40 c) in agreement with XRD analyses and with the known Y₂O₃-Nb₂O₅ phase diagram. This tentative phase diagram actually shows a Y₂O₃-Y₃NbO₇ biphasic domain for Nb compositions lower than about 20 % and a Y₃NbO₇-YNbO₄ biphasic domain for Nb compositions higher than about 31 % [Babich 1989]. As said previously, these secondary phases result from the partial decomposition of the Y₃NbO₇ intermediate phase at 1600°C [Kim 2016]. But whatever the excitation wavelengths, for one given composition, the emission curves are perfectly superimposed and do not present co-existence between the 1 and 2 emission as observed previously on the SPS sintered pellet. This is confirmed by the XRD patterns of the powders (Fig. 2.36) which do not present splitting of the diffraction peaks at the highest angles. This is not related to a lowest crystallinity of the materials but it can be attributed to the heating mode (natural heating in a standard furnace) that does not exacerbate ion mobility like in SPS

sintering. Conversely, the specificity of the SPS technique results in the stabilization of two fluorite end-compositions of the niobate intermediate phase. We can conclude that the composition splitting into a low and a high niobium content fluorite-type composition is induced or accelerated by the SPS process and the post-reoxydation process. The SPS experiments seems to reveal the existence of a lack of miscibility at 1600°C between a 24% and a 28-29% of niobium content.

Interdiffusions of different phases within complex architecture pellets as sandwich pellets prepared by SPS and reactive sintering were observed previously. The corresponding studies clearly highlight the correlation between the direction of diffusion, creation of interphases, depletion zone and the current sense or current pulses frequency [**Santanach 2011**][**Albino 2016**]. Moreover, in these studies, intermediate phases are stabilized in the interphase because of a reactive sintering. In the present investigation, the experimental conditions make possible the preservation of the niobate solid solution but create a complex system leading to a larger dispersal of the properties.

2.3.3 Intermediary conclusion

The occurrence of two spectral fingerprints of europium emissions was enhanced on a pellet sintered through spark plasma sintering process. This is the consequence of a phase splitting into two fluorite-type compositions in which environments of the rare earth ions differ. The intrinsic disorder due to the occurrence of oxygen vacancies results in amorphous-type responses of the luminescent cations and it varies as a function of niobium content. These observations are also supported by electron diffraction patterns (TEM) that shows grain inhomogeneities within the observed materials.

Because such an optical response is not observed in powders heated under the same conditions of time and temperature in a standard furnace, we can conclude that this is related to the SPS sintering process, pressure coupled with a current effect, which activates or accelerates oxygen mobility resulting into the stabilization of two close compositions of the initial niobate phase. These analysis seems to confirm the existence of a lack of miscibility at high temperature in the phase diagram.

2.3.4. Luminescence of Ho³⁺ doped Y₃NbO₇

Using europium luminescence, we have fixed the optimized synthesis and SPS parameters to obtain pure pellets densified up to 98-99%. However, the visible efficiency of the europium doped matrix is poor regarding the strong configurational quenching. In addition, the final density is not good enough to perform laser tests. Moreover, the diffusion criteria due to

porosity are not so drastic in the mid-IR and the amorphous-type emission should be a strong advantage to play with the tunnability of doped materials.

We show here the first measurements of Ho^{3+} doped Y_3NbO_7 . This host is compared to that of the sesquioxide Ho^{3+} doped Y_2O_3 . The experimental conditions of the acquisitions are equivalent for both materials and we can observe similar resulting intensities of the niobate phase and the sesquioxide as raw powders (Fig. 2.41). The emission of a niobate pellet shows a much more defined signal due to the thermal treatment.

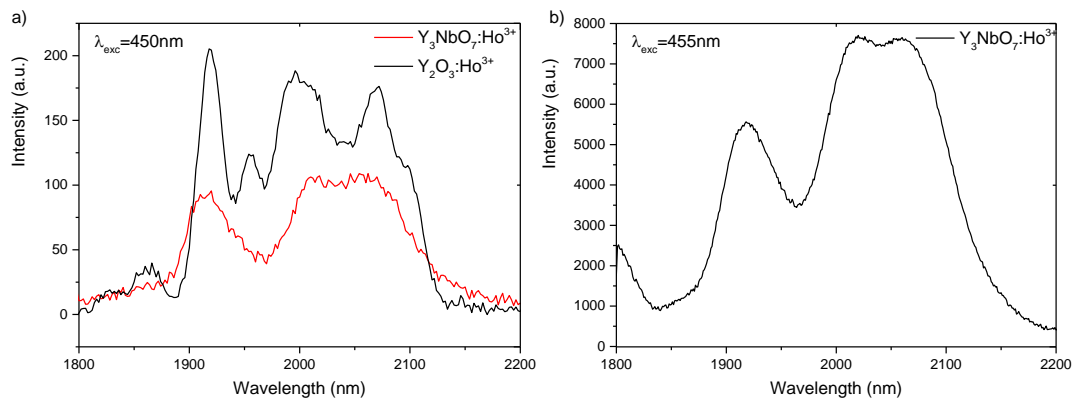


Figure 2.41: Mid-IR emission of (a) Ho^{3+} doped powder and (b) Ho^{3+} doped pellet niobate

References

- [Abe 2006]** R. Abe, M. Higashi, K. Sayama, Y. Abe, H. Sugihara, *J. Phys. Chem. B* **110**, (2006) 2219-2226
- [Albino 2016]** M. Albino, U-C. Chung, A. Kassas, J. Lesseur, D. Bernard, C. Elissalde, M. Maglione, *J. Am. Ceram. Soc.* **99** (2), (2016) 406–409
- [Amaguchki 1985]** O. Amaguchki, A. Atsuit, A. Wabe, K. Himizu, *J. Am. Ceram. Soc.* **68** (10), (1985) C-275-C-276
- [An 2011-1]** L. An, A. Ito, T. Goto, *Mater. Lett.* **65**, (2011) 3167-3169
- [An 2011-2]** L. An, A. Ito, T. Goto, *Ceram. Int.* **37**, (2011) 2263–2267
- [An 2013]** L. An, A. Ito, T. Goto, *Ceram. Int.* **39**, (2013) 383–387
- [Allpress 1979]** J.G. Allpress, H.J. Rossell, *J. Solid State Chem.* **27** (1), (1979) 105-114
- [Babich 1989]** T.G. Babich, A.V. Zagorodnyuk, G.A. Teterin, L.V. Sadkovskaya, A.P. Zhirnova, *Ukr. Khim. Zh.*, **55** (2), (1989) 132-134 ; translated *Sov. Progr. Chem.* **55** (2), (1989) 21-24.
- [Barker 1984]** W. W. Barker, *J. Mater. Sci. Lett.* **3** (6), (1984) 492-494
- [Blasse 1993]** G. Blasse, *Chem. Phys. Lett.* **70**, (1980) 1-3
- [Bondar 1969]** N.A. Bondar, L.N. Koroleva, N. A. Toropov, *Inorg. Mater.*, **5** (10), (1969) 1465-1465, translated from *Izv. Akad. Nauk SSSR, Neorg. Mater.* **5** (10), (1969) 1730-1733.
- [Cai 2007]** L. Cai, J.C. Nino, *J. Eur. Ceram. Soc.* **27**, (2007) 3971-3976
- [Cai 2010]** L. Cai, J.C. Nino, *J. Eur. Ceram. Soc.* **30**, (2010) 307–313
- [Cauley 1973]** R.A. Mc Cauley, F.A. Hummel, *J. Lumin.* **6**, (1973) 105-115
- [Chen 2013]** S. Chen, Y. Wu, *Am. Ceram. Soc. Bull.* **92** (2), (2013) 32-37
- [Cherepy 2007]** N.J. Cherepy, J.D. Kuntz, T.M. Tillotson, D.T. Speaks, S.A. Payne, B.H.T. Chai, Y. Porter-Chapman, S.E. Derenzo, *Nucl. Instrum.: Methods Phys. Res. Sect. A* **579**, (2007) 38-41
- [Choi 1990]** H.K. Choi, C.A. Wang, *Appl. Phys. Lett.* **57**, (1990) 321-323
- [Coble 1961]** R.L. Coble., *J Appl. Phys.* **32**, (1961) 793
- [Đačanin 2014]** Lj.R. Đačanin, S.R. Lukić-Petrović, D.M. Petrović, M.G. Nikolić, M.D. Dramićanin, *J. Lumin.* **151**, (2014) 82-87
- [Doi 2009]** Y. Doi, Y. Harada, Y. Hinatsu, *J. Solid State Chem.* **182** (4), (2009) 709-715

- [Forest 1969]** H. Forest, G. Ban, J. Electrochem. Soc.: solid state sciences **116** (4), (1969) 474-478
- [Fornasiero 2004]** P. Fornasiero, A. Speghini, R. Di Monte, M. Bettinelli, J. Kašpar, A. Bigotto, V. Sergo, M. Graziani, Chem. Mater. **16** (10), (2004) 1938
- [Fu 2013]** P. Fu, W. Lu, W. Lei, Y. Xu, X. Wang, J. Wu, Ceram. Int. **39**, (2013) 2481-2487
- [García-Martin 2000]** S. García-Martin, M.A. Alario-Franco, D.P. Fagg, A.J. Feighery, J.T.S. Irvine, Chem. Mater. **12**, (2000) 1729-1737
- [German 1996]** R.M. German, Sintering theory and practice, Ed. John Wiley & Sons, Inc., New York, USA. (1996)
- [Glorieux 2011]** B. Glorieux, V. Jubera, A. Apeceixborde, A. Garcia, Solid State Sci. **13**, (2011) 460-467
- [Goldstein 2009]** A. Goldstein, A. Goldenberg, M. Hefetz, J. Ceram. Soc. Jpn. **117** (11), (2009) 1281-1283
- [Groza 1992]** J.R. Groza, S.H. Risbud, K Yamazaki, J. Mater. Res. **7(10)**, (1992) 2643-2645
- [Hirano 2013]** M. Hirano, H. Dozono, J. Solid State Chem. **204**, (2013) 335-340
- [Hirano 2013]** M. Hirano, H. Dozono, J. Am. Ceram. Soc. **96** (11), (2013) 3389-3393
- [Hirano 2014]** M. Hirano, H. Dozono, Mat. Res. Bull. **50**, (2014) 213-220
- [Hirayama 2008]** M. Hirayama, N. Sonoyama, A. Yamada, R. Kanno, J. Lumin. **128**, (2008) 1819-1825
- [Ikesue 1992]** A. Ikesue, Japanese patent, (1992) 3463941
- [Ikesue 1995]** A. Ikesue, T. Kinoshita, K. Kamata, K. Yoshida, J. Am. Ceram. Soc. **78**, (1995) 1033–1040
- [Jin 2010]** L. Jin, G. Zhou, S. Shimai, J. Zhang, S. Wang, J. Eur. Ceram. Soc. **30** (2010) 2139-2143
- [Jubera 2013]** V. Jubera, J.P. Chaminade, A. Garcia, F. Guillen, C. Fouassier, J. Lumin. **101**, (2003) 1–10
- [Jurkschat 2004]** K. Jurkschat, P. Sarin, L. F. Siah, W.M. Kriven, Adv. X Ray Anal. **47**, (2004) 357-362
- [Kahn-Harari 1995]** A. Kahn-Harari, L. Mazerolles, D. Michel, F. Robert, J. Solid State Chem. **116** (1), (1995) 103-106

- [Kaewkhao 2015]** J. Kaewkhao, K. Boonin, P. Yasaka, H. J. Kim, *Mat. Res. Bull.* **71**, (2015) 37-41
- [Kakihana 1996]** M. Kakihana, *J. Sol-Gel Sci. Tech.* **6** (1), (1996) 7-55
- [Kim 2016]** K-Y. Kim, A. Durand, J-M. Heintz, A. Veillere, V. Jubera, *J. Solid State Chem.* **235**, (2016) 169–174
- [Klement 2008]** R. Klement, S. Rolc, R. Mikulikova, J. Krestan, *J. Eur. Ceram. Soc.* **28**, (2008) 1091–1095
- [Kobayashi 1992]** H. Kobayashi, H. Kuramochi, H. Ogino, T. Mori, H. Yamamura, T. Mitamura, *J. Ceram. Soc. Jpn.* **100**, (1992) 960-964.
- [Koepke 1993]** C. Koepke, A.J. Wojtowicz, J. Lempicki, *J. Lumin.* **54**, (1993) 345-355
- [Kovyazina 2003]** S.A. Kovyazina, L.A. Perelyaeva, I.A. Leonidov, Y. A. Bakhteeva, *J. Struc. Chem.* **44** (6), (2003) 975-979
- [Kozhevnikova 2015]** N. M. Kozhevnikova, S. Yu Tsyretarova, *Inorg. Mater.* **51** (5), (2015) 494-497
- [Krell 2003]** A. Krell, P. Blank, H. Ma, T. Hutzler, *J. Am. Ceram. Soc.* **86** (1), (2003) 12–18
- [Krylov 1971]** E.I. Krylov, B.V. Shul'gin, S.A. Leont'ev, L. B. Krivonosov, V. K. Slepukhin, *Izv Vuz Fiz*, **6** (1971) 143-145/ translated E. I. Krylov, B. V. Shul'gin, S. A. Leont'ev, L. B. Krivonosov, V. K. Slepukhin, *Soviet Physics Journal* **14** (6), (1971) 854-855.
- [Lee 1998]** J-H. Lee, M. Yashima, M. Kakihana, M. Yoshimura, *J. AM. Ceram. Soc.* **81** (4), (1998) 894-900
- [López-Conesa 2013]** L. López-Conesa, J.M. Rebled, M.H. Chambrier, K. Boulahya, J.M. González-Calbet, M.D. Braidá, G. Dezanneau, S. Estradé, F. Peiró, *Fuel Cells* **13**, (2013) 29-33
- [Li 2016]** W. Li, B. Mei, J. Song, W. Zhu, G. Yi, *J. Alloys Compd.* **660**, (2016) 370-374
- [Marrocchelli 2009]** D. Marrocchelli, P. A Madden, S. T Norberg, S. Hull, *J. Phys.: Condens. Mat.* **21** (40), (2009) 405403/1-405403/12
- [Montini 2009]** T. Montini, A. Speghini, L. De Rogatis, B. Lorenzut, M. Bettinelli, M. Graziani, P. Fornasiero, *J. Am. Ceram. Soc.* **131**, (2009) 13155-13160
- [Morita 2015]** K. Morita, B-N. Kim, H. Yoshida, K. Hiraga, Y. Sakka, *Acta Mater.* **84**, (2015) 9-19
- [Miida 1997]** R. Miida, F. Sato, M. Tanaka, H. Naito, H. Arashi, *J. Appl. Cryst.* **30**, (1997) 272-279

- [Norberg 2009]** S. T Norberg, I. Ahmed, S. Hull, D. Marrocchelli, P., A Madden, J. Phys: Condens. Mat. **21** (21), (2009) 215401/1-215401/11
- [Okubo 1997]** T. Okubo, M. Kakihana, J. Alloys Compd. **256**, (1997) 151-154
- [Patterson 1939]** A. L. Patterson, Phys. Rev. **56** (10), (1939) 978–982
- [Pechini 1967]** M. P. Pechini, US Patent n°3 330 697 (1967)
- [Podowitz 2010]** S. R. Podowitz, R. Gaumé, R. S. Feigelson, J. Am. Ceram. Soc. **93** (1) (2010) 82-88
- [Peuchert 2009]** U. Peuchert, Y. Okano, Y. Menke, S. Reichel, A. Ikesue, J. Eur. Ceram. Soc. **29**, (2009) 283–291
- [Rodriguez-Carvajal 2001]** J. Rodriguez-Carvajal, Commission on Powder Diffraction (IUCr) Newsletter, 2001
- [Rodriguez 2001]** J. Rodriguez-Carvajal, Commission on Powder Diffraction (IUCr) Newsletter (2001)
- [Rooksby 1964]** H.P. Rooksby, E.A.D. White, J. Am. Ceram. Soc. **47** (2), (1964) 94-96
- [Rossell 1979]** H.J. Rossell, J. Solid State Chem. **27** (1), (1979) 115-122
- [Santanach 2011]** J. G. Santanach, C. Estournès, A. Weibel, G. Chevallier, V. Bley, C. Laurent, A. Peigney, J. Eur. Ceram. Soc. **31**, (2011) 2247-2254
- [Scherrer 1918]** P. Scherrer, Nach. Gesell. Wissens. Gott. Math. Phys. **1-2**, (1918) 96-100
- [Siqueira 2014]** K.P.F. Siqueira, J.C. Soares, E. Granado, E.M. Bittar, A.M. de Paula, R.L. Moreira, A. Dias, J. Solid State Chem. **209**, (2014) 63-68
- [Subramanian 1983]** M.A. Subramanian, G. Aravamudan, Rao G.V. Subba, Solid State Ch. **15** (2), (1983) 55-143
- [Tarafder 2011]** A. Tarafder, B. Karmakar, Engineering "Electrical and Electronic Engineering" Ferroelectrics - Material Aspects", book edited by Mickaël Lallart, Nanostructured LiTaO₃ and KNbO₃ Ferroelectric Transparent Glass-Ceramics for Applications in Optoelectronics, August 24, (2011) 389-412
- [Tilloca 1970]** G. Tilloca, M. Perez y Jorda, F. Queyroux, C.R. Acad. Sc. Paris Serie C: Sciences chimiques **271** (2), (1970) 134-135
- [Tilloca 1972]** G. Tilloca, M. Perez y Jorda, C.R. Acad. Sc. Paris, Serie C: Sciences Chimiques **274**, (1972) 93-95

- [Trunov 1981]** V.K.;Trunov, V.A Efremov, Yu. A Velikopodnyi, I.M. Averin, Kristallografiya **26** (1), (1981) 67-71
- [Vent 1994]** J.F. Vent, R.B. Helmholtz, D.J.W. IJdo, J. Solid State Chem. **108** (1), (1994) 18-23
- [Wakeshima 2010]** M. Wakeshima, Y. Hinatsu, J. Solid State Chem. **183** (11), (2010) 2681-2688
- [Walasek 2007-1]** A. Walasek, E. Zych, J. Zhang, S. Wang, J. Lumin. **127** (2), (2007) 523-530
- [Walasek 2007-2]** A. Walasek, J. Zhang, S. Wang, E. Zych, Opt. Mater. **30** (1), (2007) 188-191
- [Withers 1991]** R.L. Withers, J.G. Thompson, P.J. Barlow, J. Solid State Chem. **94**, (1991) 89-105
- [Withers 1992]** R. L. Withers, J.G. Thompson, P.J. Barlow, J.C. Barry, Aust. J. Chem. **45**, (1992) 1375-1395
- [Yamamura 1999]** H. Yamamura, K. Matsui, K. Kakinuma, T. Mori, Solid State Ionics **123**, (1999) 279–285
- [Zhao 2015]** J. Zhao, Q. He, B. Yao, Q. Zhang, T. Zhang, Q. Wang, X. Han, Ceram. Int. **41** (6), (2015) 7669-7676
- [Zhou 2003]** Y. Zhou, K. Hirao, Y. Yamauchi, S. Kanzaki, Scr. Mater. **46**, (2003) 1631-1636

Chapter 3

Conclusion

We successfully optimize a Pechini type synthesis route which makes possible the stabilization of pure Eu^{3+} doped Y_3NbO_7 compounds. In addition, the obtained powder present an adequate nano-size and morphology to favor a high densification through SPS process.

SPS pellets were all analyzed by X-ray diffraction, SEM and their densities were measured. But in order to understand the behavior of the Y_3NbO_7 during the sintering process, this matrix was doped with trivalent europium ions. Thanks to its energetic diagram, this ion is traditionally used as a local probe to study the environment of rare earth element.

Because the spectral distribution and shape of the 4f-4f emission lines of the potential impurities differ totally from those of the niobate solid solution, their fingerprint can easily be distinguished in the global emission curves.

A first control of the raw powder reveals that Y_2O_3 and/or YNbO_4 are stabilized after a half hour treatment at 1100°C . In addition, the spectral distribution reflects a distorted and amorphous-type coordination polyhedron around the doping element. This emission is shifted to the higher energy when the temperature of the treatment increases.

The optical properties of the pellets highlight the SPS current effect on the niobate host. This electron mobility linked with the heating rate value, accelerates the ionic mobility leading to the stabilization of two fluorite-type compositions within the pellet. The optical answer is by consequence, constituted by two distinct europium emissions. Refinements of cell parameters are consistent with a 24% and a 28-29% of Niobium ratio ($\text{Nb}/\text{Nb}+\text{Y}$) with a higher proportion of the lowest niobium content which is also the more defective fluorite host.

The intrinsic disorder due to the occurrence of oxygen vacancies may be the origin of amorphous-type responses of the luminescent cations and it varies as a function of niobium content. These observations are also supported by electron diffraction patterns (TEM).

These results point out the fact that after a SPS treatment at 1600°C, the Y_3NbO_7 compound may not be the more stable state of the niobate phase and a miscibility gap might exist in the phase diagram, under such sintering conditions.

Taking into account the residual porosity, the purity of the final pellet and the density, the optimized and reference conditions resulting from the 102 experiments performed during these investigations are the following:

- Temperature: 1600°C
- Heating rate: 5°C.min⁻¹
- Dwell time: 20 min.
- Pressure: 100 MPa (which correspond to an applied strength of 7.9 kN).

Finally, the spark plasma sintering of the Eu^{3+} doped Y_3NbO_7 niobate makes possible a better understanding of this material. The structural characterizations coupled with the luminescence spectroscopy clearly demonstrate that this cubic matrix tolerates a large versatility of the niobium/yttrium content. A shift of composition can be driven by thermal heat-treatment. An unexpected consequence is a large spectral distribution of rare earth emissions. The high current used by the SPS technique activates ionic mobility leading to a decomposition splitting. As a consequence, transparency has not been reached since full densification cannot be performed. By consequence, the SPS technique might not be the best sintering process to obtain transparent Y_3NbO_7 ceramic.

The next step will be to investigate other sintering processes in order to keep a homogeneous composition of the solid solution. And the sintering parameters will have to be optimized to reach a full densified and transparent pellet.

Titre : Etude d'une céramique de niobate dopée terre rare, Y_3NbO_7 , pour applications optiques

Résumé :

Les matériaux émetteurs et les lasers solides sont largement employés dans le domaine de l'optique et des sciences des matériaux en tant que sources d'excitation, pour des mesures expérimentales, des applications médicales, de la mise en forme ou de la découpe de métaux...Récemment des valeurs d'efficacité laser prometteuses ont été obtenues à partir de céramiques transparentes qui résultent de procédés de mises en forme plus rapides et moins coûteux de matériaux à l'état cristallisé.

Les travaux de recherche proposés sont centrés sur une matrice cubique dopée par des ions Eu^{3+} de formule Y_3NbO_7 . Les voies de synthèse sont optimisées pour obtenir une phase pure présentant des grains homogènes en taille et de morphologie sphérique. Les paramètres SPS tels que la montée en température, la température et la durée de frittage ainsi que la pression sont ajustés pour favoriser la densification des pastilles.

La spectroscopie de luminescence des ions europium trivalents est employée pour optimiser les paramètres étudiés. Les émissions enregistrées couplées à la diffraction des rayons X et à la microscopie électronique en transmission soulignent l'existence de plusieurs environnements distordus autour des ions dopants dans le réseau de type fluorine lacunaire. La cristallisation rapide obtenue par SPS, couplée à la nature du niobate de terre rare, conducteur ionique, conduit à une démixtion de la solution solide de Y_3NbO_7 en deux fluorines distinctes. La composition finale de la pastille est conditionnée par le ratio cationique Nb/Y.

Mots clés : Y_3NbO_7 , SPS, europium, luminescence

Title : Investigation of a rare earth doped niobate ceramic for optical applications

Abstract :

Emitting materials and all solid state lasers are widely used in the field of optical applications and materials science as a source of excitement, instrumental measurements, medical applications, metal shaping...Recently promising laser efficiencies were recorded on transparent ceramics which results from a cheaper and faster ways to obtain crystallized materials.

This investigation is focused on the cubic Eu^{3+} doped Y_3NbO_7 matrix. The synthesis route is optimized in order to obtain a pure phase which presents a homogeneous morphology of spherical grains. Several SPS parameters as heating rate, temperature, duration time and pressure are adjusted in order to increase the densification of the pellets. Luminescence spectroscopy of trivalent europium ions is used to optimize these parameters. The emission data coupled with X-Ray diffraction analysis and electronic diffraction microscopy highlight the existence of several distorted environments of the doping element in the defective fluorite type Y_3NbO_7 host lattice. Indeed, the fast and high crystallization rate obtained after SPS coupled with the ionic conductivity of the matrix make possible a phase composition splitting into two fluorites. The final composition of the pellet is driven by the ratio between niobium and yttrium elements.

Keywords : Y_3NbO_7 , SPS, europium, luminescence

Unité de recherche

ICMCB-UPR 9048 – 87 av. Dr. A. Schweitzer, 33608 PESSAC cedex